DISTRIBUTED COOPERATIVE CONTROL OF AC MICROGRIDS

by

ALI BIDRAM

Presented to the Faculty of the Graduate School of

The University of Texas at Arlington in Partial Fulfillment

of the Requirements

for the Degree of

DOCTOR OF PHILOSOPHY

THE UNIVERSITY OF TEXAS AT ARLINGTON

August 2014

Acknowledgements

First, I thank God for endowing me the boundless mercy and power of thinking.

I wish to express my sincere appreciation to my supervisors Dr. Ali Davoudi and Dr. Frank L. Lewis. With their kind and unconditional supports, I was able to continue my PhD studies. Not only they provided me with technical guidelines, but also they taught me how to manage challenging situations.

I am thankful to my dissertation defense committee members, Dr. William Dillon, Dr. Wei-Jen Lee, Dr. Rasool Kenarangui, and Dr. Dan Popa for their instructive guidelines and constructive and improving comments on my dissertation. My special thanks to Dr. Jonathan Bredow and Dr. Kambiz Alavi for providing the Electrical Engineering department students with a great atmosphere to pursue their studies. I need to thank Electrical Engineering department staffs, specially, Ms Gail Paniuski, for their kind help in my PhD studies. I wish to appreciate Mr. Vahidreza Nasirian, Mr. Hamidreza Modares, Dr. Hamid Behjati, Mr. Lei Niu, Mr. Ali Moayedi, and Mr. Fatih Cingoz for being supportive in all of the stages of my PhD.

This dissertation is supported in part by National Science Foundation under the grant numbers ECCS-1137354, ECCS-1128050, and NSFCS-61374087, N. M Stelmakh outstanding student research award, China NNSF grant 61120106011, and China Education Ministry Project 111 (No.B08015).

I wish to specially thank my parents for their ever-lasting love and support.

I wish to express my utmost appreciation to my lovely wife, Maryam, to whom this dissertation is dedicated. Without her unconditional support and kind encouragement my PhD studies would be longer and more difficult. Not only she never ceased her unconditional support and love, she is also my program manager and great consultant.

July 9, 2014

To my love, Maryam

Abstract

DISTRIBUTED COOPERATIVE CONTROL OF MICROGRIDS

Ali Bidram, PhD

The University of Texas at Arlington, 2014

Supervising Professors: Ali Davoudi and Frank L. Lewis

In this dissertation, the comprehensive secondary control of electric power microgrids is of concern. Microgrid technical challenges are mainly realized through the hierarchical control structure, including primary, secondary, and tertiary control levels. Primary control level is locally implemented at each distributed generator (DG), while the secondary and tertiary control levels are conventionally implemented through a centralized control structure. The centralized structure requires a central controller which increases the reliability concerns by posing the single point of failure. In this dissertation, the distributed control structure using the distributed cooperative control of multi-agent systems is exploited to increase the secondary control reliability. The secondary control objectives are microgrid voltage and frequency, and distributed generators (DGs) active and reactive powers. Fully distributed control protocols are implemented through distributed communication networks. In the distributed control structure, each DG only requires its own information and the information of its neighbors on the communication network. The distributed structure obviates the requirements for a central controller and complex communication network which, in turn, improves the system reliability. Since the DG dynamics are nonlinear and non-identical, input-output feedback linearization is used to transform the nonlinear dynamics of DGs to linear dynamics. Proposed control frameworks cover the control of microgrids containing inverter-based DGs. Typical microgrid test systems are used to verify the effectiveness of the proposed control protocols.

Table of Contents

Acknowledgement ..... ……..iii

Abstract v

List of Illustrations ix

List of Tables xiii

Chapter 1 Introduction……..…….…..... 1

Hierarchical Control Structure of Microgrids 1

Primary Control 3

Secondary Control 26

Tertiary Control 29

Problem Definition 31

Dissertation Outline 35

Chapter 2 Distributed Secondary Voltage Control of Microgrids 37

Introduction 37

Large Signal Dynamical Model of an Inverter-Based Distributed Generator 37

Secondary Voltage Control Based on Distributed Cooperative Control 42

Preliminary of Graph Theory 43

Cooperative Secondary Voltage Control Based on Feedback Linearization and Tracking Synchronization Problem 43

The Required Sparse Communication Topology for Secondary Control 49

Simulation Results for the Distributed Secondary Voltage Control 50

Simulation Results for Different Reference Voltage Values 51

The Effect of Algebraic Riccati Equation (ARE) Parameters on the Transient Response 54

The Effect of Time-varying Communication Networks on the Performance of the Distributed Secondary Voltage Control 56

Conclusion 57

Chapter 3 Distributed Secondary Frequency Control of Microgrids 58
Introduction 58
Secondary Frequency Control Objectives 58
Secondary Frequency Control Based on Distributed Cooperative Control 60
Simulation Results for the Distributed Secondary Frequency Control 65
Conclusion 68
Chapter 4 Two-Layer Multi-Objective Control
Framework for Microgrids 70
Introduction 70
Two-Layer Multi-Objective Control Framework for Microgrids 72
Dynamical Model of CCVSIs 76
Controller Design for Each Layer of the Proposed Control Framework 79
Control Layer 1: Frequency and Voltage Control of VCVSIs 79
Control layer 2: Active and Reactive Power Control of CCVSIs 82
Simulation Results for the Two-Layer Multi-Objective Control Framework 87
Simulation Results for the Microgrid Test System in Figure 4-8 87
Simulation Results for the IEEE 34 Bus Test Feeder 99
Conclusion 104
Chapter 5 Adaptive and Distributed Secondary Voltage Control of Microgrids 105
Introduction 105
Adaptive and Distributed Secondary Voltage Control 106
Sliding Mode Error 107
The Adaptive and Distributed Controller Design 109
Simulation Results for the Adaptive and Distributed Secondary Voltage Control 116
Case 1 117
Case 2 119

Case 3 120
Case 4 121
Conclusion 123
Chapter 6 Conclusions and Future Works 124
Contributions and Conclusions 124
Future Works 126
Appendix A The Effects of the Algebraic Riccati Equation Parameters on the Synchronization Speed of the Secondary Voltage Control 128
Appendix B The Specifications of Microgrid Test System in Figure 2-6 130
Appendix C The Effect of the Controller Gain on the Convergence Speed in a Tracking Synchnization Problem 132
Appendix D The Specifications of the Microgrid Test System in Figure 4-8 138
Appendix E The Specifications of the IEEE 34 Bus Test Feeder 141
References 144
Biographical Information 155

List of Illustrations

Figure 1-1 Hierarchical Control Levels of a Microgrid 2
Figure 1-2 PQ Control Mode With Active and Reactive Power References 4
Figure 1-3 Reference Voltage Determination for Voltage Control Mode 5
Figure 1-4 Voltage and Current Control Loops in Voltage Control Mode 5
Figure 1-5 Zero-Level Control Loops for a Set of Energy Sources Connected to an AC Bus 5
Figure 1-6 Conventional Droop Method 7
Figure 1-7 Simplified Diagram of a Converter Connected to the Microgrid 7
Figure 1-8 Small Signal Model of the Conventional Active Power Control 8
Figure 1-9 The Small Signal Model of the Adjustable Active Power Control 11
Figure 1-10 The Small Signal Model of the Adjustable Reactive Power Control 11
Figure 1-11 Droop/Boost Characteristics for Low-Voltage Microgrids: (a) Voltage-Active Power Droop Characteristic and (b) Frequency-Reactive Power Boost Characteristic 12
Figure 1-12 Droop Method with Virtual Power Frame Transformation 14
Figure 1-13 Block Diagram of the Virtual Output Impedance Method 16
Figure 1-14 Virtual Output Impedance with Voltage Unbalance Compensator 16
Figure 1-15 A Typical Two-DG System 18
Figure 1-16 Block Diagram of the Signal Injection Method for Reactive Power Sharing 20
Figure 1-17 Block Diagram of the Updated Signal Injection Method 20
Figure 1-18 Control Block Diagram for the Harmonic Cancellation Technique 23
Figure 1-19 h^{th} Harmonic Equivalent Circuit of a DG 23
Figure 1-20 Block Diagram of the Secondary and Tertiary Controls 28
Figure 1-21 The Potential Function-Based Technique Block Diagram 29
Figure 1-22 Voltage Unbalance Compensation in the Secondary Control 29
Figure 1-23 Marginal Cost Function Matching Between Two DGs 30
Figure 1-24 The Secondary Control Structures: (a) Centralized and (b) Distributed 32

Figure 1-25 Multi-Agent Environment for a Microgrid System with DGs as Agents 33

Figure 2-1 The Block Diagram of an Inverter-Based DG 40

Figure 2-2 The Block Diagram of the Power Controller 40

Figure 2-3 The Block Diagram of the Voltage Controller 41

Figure 2-4 The Block Diagram of the Current Controller 41

Figure 2-5 The Block Diagram of the Proposed Secondary Voltage Control 48

Figure 2-6 Single Line Diagram of the Microgrid Test System 51

Figure 2-7 Topology of the Communication Digraph 51

Figure 2-8 DG Output Voltage Magnitudes:(a) When v_{ref}=1 pu, (b) When v_{ref}=0.95 pu, and (c) when v_{ref}=1.05 pu 53

Figure 2-9 Critical Bus Voltage Magnitude 54

Figure 2-10 DG Output Voltage Magnitudes with the Following Control Parameters: (a) $Q=\begin{bmatrix}1000 & 0\\ 0 & 1\end{bmatrix}$ and R=0.01 and (b) $Q=\begin{bmatrix}50000 & 0\\ 0 & 1\end{bmatrix}$ and R=5 55

Figure 2-11 Topologies of the Time-Varying Communication Network 56

Figure 2-12 DG Output Voltage Magnitudes with Time-Varying Communication Network 57

Figure 3-1 The Block Diagram of the Distributed Secondary Frequency Control 64

Figure 3-2 The Secondary Frequency Control with c_f= 400 and f_{ref}= 50 Hz: (a) DG Angular Frequencies and (b) DG Active Power Ratios 66

Figure 3-3 The Secondary Frequency Control with c_f= 40 and f_{ref}= 50 Hz: (a) DG Angular Frequencies and (b) DG Active Power Ratios 67

Figure 3-4 The Secondary Frequency Control with Time-Varying Communication Network: (a) DG Frequencies and (b) DG Active Power Ratios 69

Figure 4-1 The Comprehensive Distributed Control of Microgrids with Two Control Layers 74

Figure 4-2 The Block Diagram of a CCVSI 77

Figure 4-3 The Bock Diagram of α_i Calculator 77

Figure 4-4 The Block Diagram of the Current Controller for a CCVSI 78

Figure 4-5 The Block Diagram of the Voltage Control in the Control Layer 1 81
Figure 4-6 The Block Diagram of the Active Power Control in the Control Layer 2 84
Figure 4-7 The Block Diagram of the Reactive Power Control in the Control Layer 2 86
Figure 4-8 Single Line Diagram of the Microgrid Test System 87
Figure 4-9 Topology of the Communication Digraph for (a) Control Layer 1 and (b) Control layer 2 88
Figure 4-10 Frequency Control of Control Layer 1 in *Case 1*: (a) VCVSI Frequencies and (b) VCVSI Active Power Ratios $D_{Pi}P_i$ 90
Figure 4-11 Voltage Control of Control Layer 1 in *Case 1*: (a) VCVSI Output Voltage Magnitudes and (b) VCVSI Reactive Power Ratios $D_{Qi}Q_i$ 91
Figure 4-12 Active and Reactive Power Control of Control Layer 2 in *Case 1*: (a) CCVSI Active Power ratios P_i/P_{maxi} and (b) CCVSI reactive power ratios Q_i/Q_{maxi} 92
Figure 4-13 Frequency Control of Control Layer 1 in *Case 2*: (a) VCVSI Frequencies and (b) VCVSI Active Power Ratios $D_{Pi}P_i$ 93
Figure 4-14 Voltage Control of Control Layer 1 in *Case 2*: (a) Critical Bus Voltage Magnitude and (b) VCVSI Reactive Power Ratios $D_{Qi}Q_i$ 94
Figure 4-15 Active and Reactive Power Control of Control Layer 2 in *Case 2*:(a) CCVSI Active Power Ratios P_i/P_{maxi} and (b) CCVSI Reactive Power Ratios Q_i/Q_{maxi} 95
Figure 4-16 Communication Digraphs for the Time-Varying Communication Network in *Case 3* 96
Figure 4-17 Frequency Control Using Control Layer 1 in *Case 3*: (a) VCVSI Frequencies and (b) VCVSI Active Power Ratios $D_{Pi}P_i$ 97
Figure 4-18 Voltage Control Using Control Layer 1 in *Case 3*: (a) Critical Bus Voltage Magnitude and (b) VCVSI Reactive Power Ratios $D_{Qi}Q_i$ 98
Figure 4-19 Active and Reactive Power Control Using Control Layer 2 in *Case 3*: (a) CCVSI Active Power Ratios P_i/P_{maxi} and (b) and CCVSI Reactive Power Ratios Q_i/Q_{maxi} 99

Figure 4-20 Single Line Diagram of Modified IEEE 34 Bus Test Feeder 101

Figure 4-21 Communication Digraphs for IEEE 34 Bus Test Feeder: (a) VCVSIs and (b) CCVSIs 101

Figure 4-22 Frequency Control for IEEE 34 Bus Test Feeder: (a) VCVSI Frequencies and (b) VCVSI Active Power Ratios $D_{Pi}P_i$ 102

Figure 4-23 Voltage Control for IEEE 34 Bus Test Feeder: (a) VCVSI Output Voltage Magnitudes and (b) VCVSI Reactive Power Ratios $D_{Qi}Q_i$ 103

Figure 4-24 Active and Reactive Power Control for IEEE 34 Bus Test Feeder: (a) CCVSI Active Power Ratios P_i/P_{maxi} and (b) CCVSI Reactive Power Ratios Q_i/Q_{maxi} 104

Figure 5-1 NN Structure for Estimating (a) $\overline{f}_i$ and (b) $\overline{g}_i$ 111

Figure 5-2 The Block Diagram of the Adaptive and Distributed Secondary Control 115

Figure 5-3 The Communication Digraph for *Case 1*, *Case 2, and Case 3* 118

Figure 5-4 DG Output Voltage Magnitudes for *Case 1* when v_{ref}=1 pu 118

Figure 5-5 The Voltage Magnitude of Critical Bus for *Case 1* 119

Figure 5-6 DG Output Voltage Magnitudes for *Case 1* when v_{ref}=1 pu,c_i=40, $\lambda_1 = 100$, and $\lambda_2 = 1$ 119

Figure 5-7 DG Output Voltage Magnitudes for *Case 2* 120

Figure 5-8 DG Output Voltage Magnitudes for *Case 3* 121

Figure 5-9 The Digraphs for Modeling the Time-Varying Communication Network of *Case 4* 122

Figure 5-10 DG Output Voltage Magnitudes for *Case 4* 122

List of Tables

Table 1-1 The Potential Advantage and Disadvantages of the Discussed Droop Methods 25

Table B-1 Specifications of the Microgrid Test System in Figure 2-6 131

Table D-1 Specifications of DGs for Microgrid Test Systems in Figure 4-8 139

Table D-2 Specifications of Lines for Microgrid Test Systems in Figure 4-8 140

Table D-3 Specifications of Loads for Microgrid Test Systems in Figure 4-8 140

Table E-1 Specifications of DGs for IEEE 34 Bus Test Feeder 142

Table E-2 Specifications of Loads for IEEE 34 Bus Test Feeder 143

Chapter 1

Introduction

Hierarchical Control Structure of Microgrids

Conventional electric power systems are facing continuous and rapid changes to alleviate environmental concerns, address governmental incentives, and respond to the consumer demands. The notion of the smart grid has recently emerged to introduce an intelligent electric network. Improved reliability and sustainability are among desired characteristics of smart grid affecting the distribution level. These attributes are mainly realized through microgrids which facilitate the effective integration of distributed generators (DG) [1]-[6]. Microgrids can operate in both grid-connected and islanded operating modes. Proper control of microgrid is a prerequisite for stable and economically efficient operation [6]-[13]. The principal roles of the microgrid control structure are [12]-[22]

- Voltage and frequency regulation for both operating modes,
- Proper load sharing and DG coordination,
- Microgrid resynchronization with the main grid,
- Power flow control between the microgrid and the main grid,
- Optimizing the microgrid operating cost.

These requirements are of different significances and time scales, thus requiring a hierarchical control structure [12] to address each requirement at a different control hierarchy. Hierarchical control strategy consists of three levels, namely the primary, secondary, and tertiary controls, as shown in Figure 1-1. The primary control maintains voltage and frequency stability of the microgrid subsequent to the islanding process. It is essential to provide independent active and reactive power sharing controls for the DGs in the presence of both linear and nonlinear loads. Moreover, the power sharing control avoids undesired circulating currents. The primary control level includes fundamental control hardware, commonly referred to as zero-level, which comprises internal voltage and current control loops of the DGs. The

secondary control compensates for the voltage and frequency deviations caused by the operation of the primary controls. Ultimately, the tertiary control manages the power flow between the microgrid and the main grid and facilitates an economically optimal operation [12]-[13].

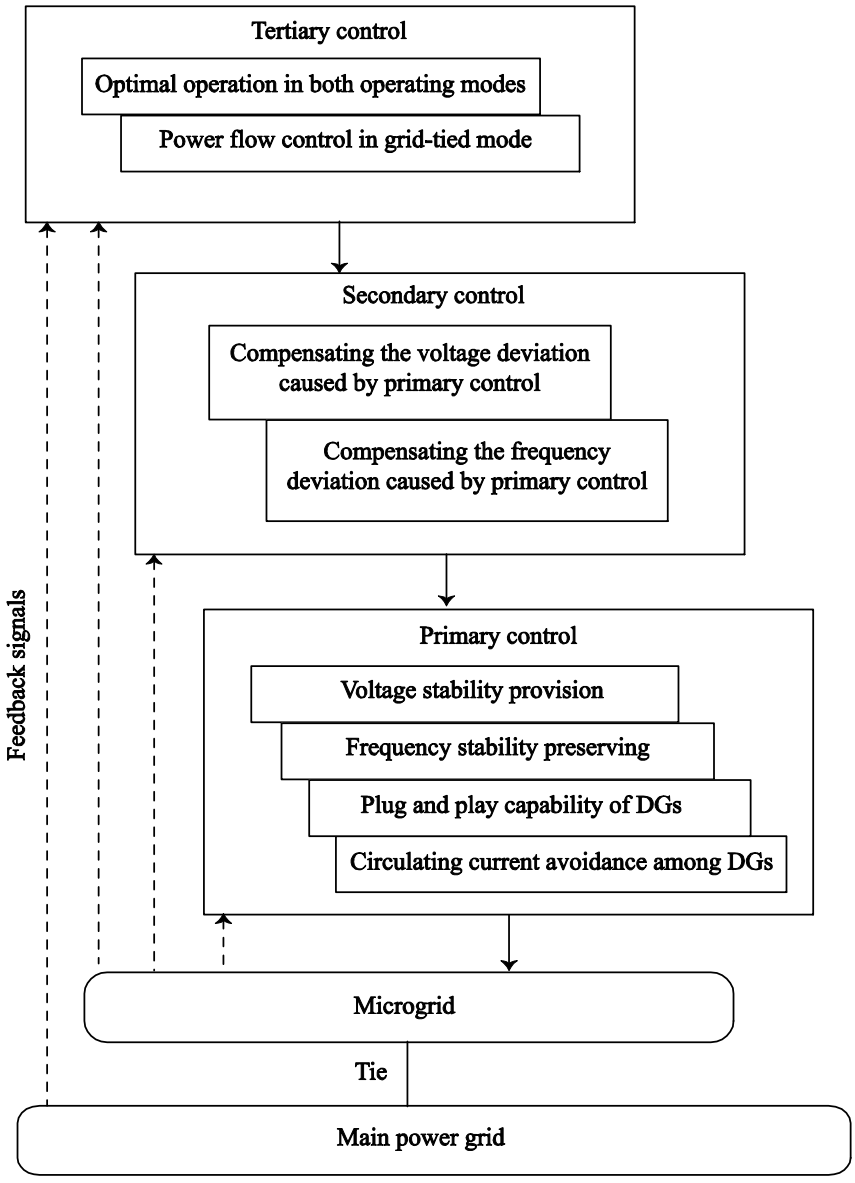

Figure 1-1 Hierarchical Control Levels of a Microgrid

Primary Control

The primary control is designed to satisfy the following requirements [12]-[13], [15], [21], [23]:

- To stabilize the voltage and frequency: Subsequent to an islanding event, the microgrid may lose its voltage and frequency stability due to the mismatch between the power generated and consumed.
- To offer plug and play capability for DGs and properly share the active and reactive power among them, preferably, without any communication links.
- To mitigate circulating currents that can cause over-current phenomenon in the power electronic devices and damage the DC-link capacitor.

The primary control provides the reference points for the voltage and current control loops of DGs. These inner control loops are commonly referred to as zero-level control. The zero-level control is generally implemented in either active/reactive power (PQ) or voltage control modes [17].

In the PQ control mode, the DG active and reactive power delivery is regulated on the pre-determined reference points, as shown in Figure 1-2. The control strategy is implemented with a current-controlled voltage source inverter (CCVSI). In Figure 1-2, H_1 controller regulates the DC-link voltage and the active power through adjusting the magnitude of the output active current of the converter, i_p. H_2 controller regulates the output reactive power by adjusting the magnitude of the output reactive current, i.e., i_q [17], [24].

In the voltage control mode, the DG operates as a voltage controlled voltage source inverter (VCVSI) where the reference voltage, v_o^*, is determined by the primary control, conventionally via droop characteristics [17], as shown in Figure 1-3. The nested voltage and current control loops in the voltage control mode are shown in Figure 1-4. This controller feeds the current signal as a feedforward term via a transfer function (e.g., virtual impedance). To fine-

tune the transient response, proportional-integral-derivative (PID) [25], adaptive [26], and proportional resonant controllers [27] are proposed for the voltage controller.

Power quality of small-scale islanded systems is of particular importance due to the presence of nonlinear and single-phase loads and the low inertia of the microgrid [28]-[30]. To improve the power quality for a set of energy sources connected to a common bus, the control structure shown in Figure 1-5 is used. In this figure, $H_{LPF}(s)$ denotes the transfer function of a low-pass filter. Each converter has an independent current control loop, and a central voltage control loop that is adopted to distribute the fundamental component of the active and reactive powers among different sources. The reference point for the voltage control loop is determined by the primary control. The individual current controllers ensure power quality by controlling the harmonic contents of the supplied currents to the common AC bus [28]. The DG's control modes are usually implemented using the droop characteristic techniques [31].

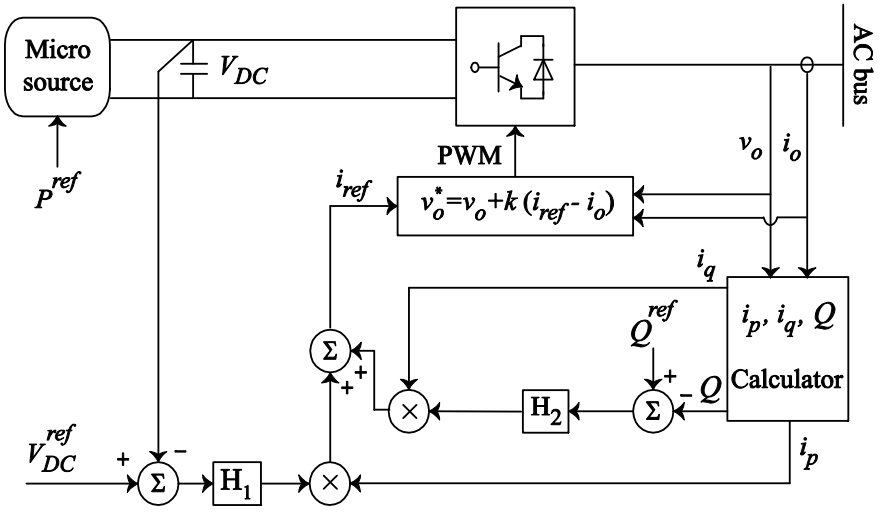

Figure 1-2 PQ Control Mode With Active and Reactive Power References [17]

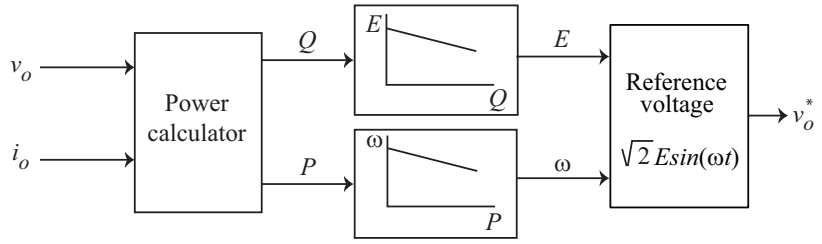

Figure 1-3 Reference Voltage Determination for Voltage Control Mode [17]

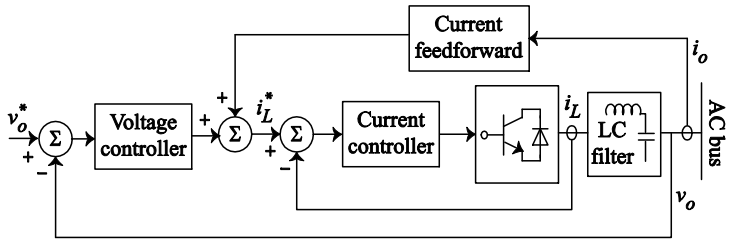

Figure 1-4 Voltage and Current Control Loops in Voltage Control Mode [28]

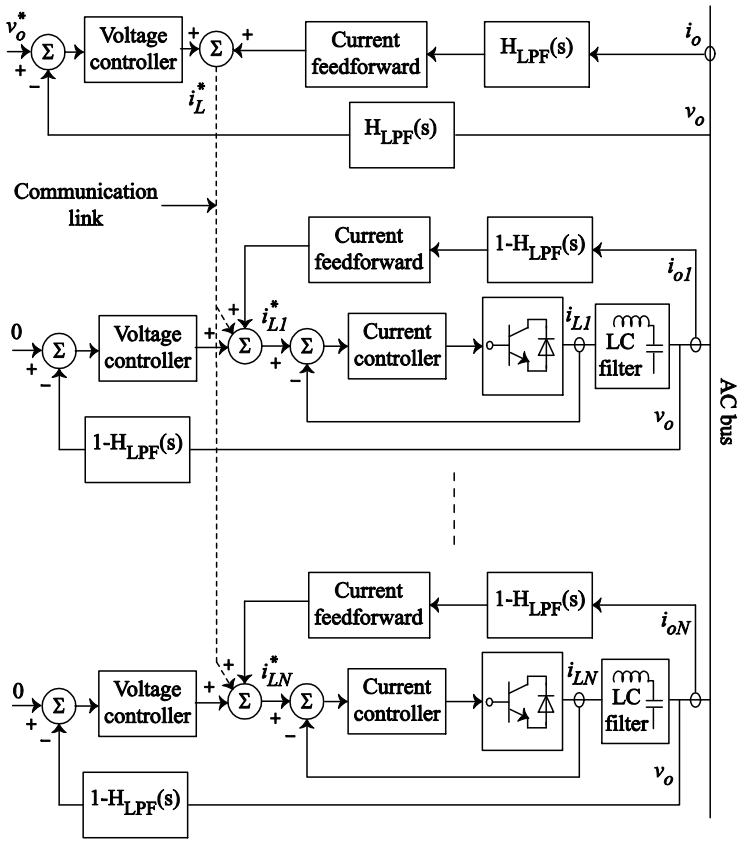

Figure 1-5 Zero-Level Control Loops for a Set of Energy Sources Connected to an AC Bus [28]

The droop control method has been referred to as the independent, autonomous, and wireless control due to elimination of intercommunication links between the converters. The conventional active power control (frequency droop characteristic) and reactive power control (voltage droop characteristic), those illustrated in Figure 1-6, are used for voltage mode control. Principles of the conventional droop methods can be explained by considering an equivalent circuit of a VCVSI connected to an AC bus, as shown in Figure 1-7. If switching ripples and high frequency harmonics are neglected, the VCVSI can be modeled as an AC source, with the voltage of $E\angle\delta$. In addition, assume that the common AC bus voltage is $V_{com}\angle 0$ and the converter output impedance and the line impedance are lumped as a single effective line impedance of $Z\angle\theta$. The complex power delivered to the common AC bus is calculated as

$$S = V_{com} I^* = \frac{V_{com} E\angle\theta - \delta}{Z} - \frac{V_{com}^2\angle\theta}{Z}, \tag{1,1}$$

from which, the real and reactive powers are achieved as

$$\begin{cases} P = \dfrac{V_{com} E}{Z}\cos(\theta - \delta) - \dfrac{V_{com}^2}{Z}\cos(\theta), \\ Q = \dfrac{V_{com} E}{Z}\sin(\theta - \delta) - \dfrac{V_{com}^2}{Z}\sin(\theta). \end{cases} \tag{1,2}$$

If the effective line impedance, $Z\angle\theta$, is assumed to be purely inductive, $\theta = 90^\circ$, then (1,2) can be reduced to

$$\begin{cases} P = \dfrac{V_{com} E}{Z}\sin\delta, \\ Q = \dfrac{V_{com} E\cos\delta - V_{com}^2}{Z}. \end{cases} \tag{1,3}$$

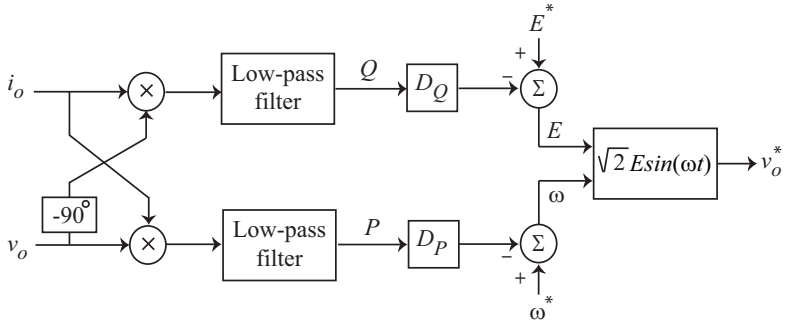

Figure 1-6 Conventional Droop Method

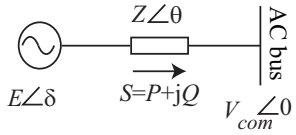

Figure 1-7 Simplified Diagram of a Converter Connected to the Microgrid

If the phase difference between the converter output voltage and the common AC bus, δ, is small enough, then, $\sin\delta \approx \delta$ and $\cos\delta \approx 1$. Thus, one can apply the frequency and voltage droop characteristics to fine-tune the voltage reference of the VCVSI [31], [38]-[43], as shown in Figure 1-6 based on

$$\begin{cases} \omega = \omega^* - D_P P, \\ E = E^* - D_Q Q, \end{cases} \tag{1,4}$$

where the primary control references E^* and ω^* are the DG output voltage RMS value and angular frequency at the no-load, respectively. The droop coefficients, D_P and D_Q, can be adjusted either heuristically or by tuning algorithms (e.g., particle swarm optimization [44]). In the former approach, D_P and D_Q are determined based on the converter power rating and the maximum allowable voltage and frequency deviations. For instance, in a microgrid with N DGs, corresponding D_P and D_Q should satisfy following constraints [45], [46]

$$\begin{cases} D_{P1}P_{n1} = D_{P2}P_{n2} = \ldots = D_{PN}P_{nN} = \Delta\omega_{\max}, \\ D_{Q1}Q_{n1} = D_{Q2}Q_{n2} = \ldots = D_{QN}Q_{nN} = \Delta E_{\max}, \end{cases} \tag{1,5}$$

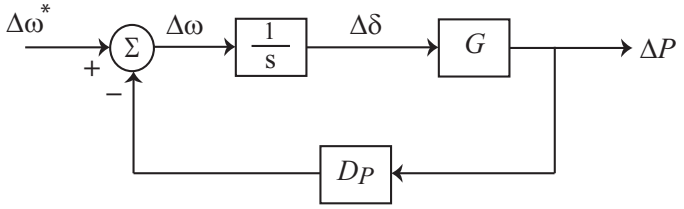

Figure 1-8 Small Signal Model of the Conventional Active Power Control

where $\Delta\omega_{\max}$ and $\Delta E_{\max}$ are the maximum allowable angular frequency and voltage deviations, respectively. P_{ni} and Q_{ni} are the nominal active and reactive power of the i^{th} DG.

During the grid-tied operation of microgrid, the DG voltage and angular frequency, E and ω, are enforced by the gird. The DG output active and reactive power references, P^{ref} and Q^{ref}, can hence be adjusted through E^* and ω^* [17] as

$$\begin{cases} P^{ref} = \dfrac{\omega^* - \omega}{D_P}, \\ Q^{ref} = \dfrac{E^* - E}{D_Q}. \end{cases} \tag{1,6}$$

Dynamics response of the conventional primary control, on the simplified system of Figure 1-7, can be studied by linearizing (1,3) and (1,4). For instance, the linearized active power equation in (1,3) and frequency droop characteristic in (1,4) are

$$\begin{cases} \Delta P = G\Delta\delta, \\ \Delta\omega = \Delta\omega^* - D_P\Delta P. \end{cases} \tag{1,7}$$

where at the operating point of V_{com0}, E_0, and δ_0

$$G = \frac{V_{com0}E_0}{Z}\cos\delta_0, \tag{1,8}$$

and

$$\Delta\delta = \int \Delta\omega dt. \tag{1,9}$$

Therefore, the small signal model for the active power control in (1,4) is

$$\Delta P(s) = \frac{G}{s + D_P G} \Delta \omega^*(s). \tag{1,10}$$

A similar procedure can be adopted to extract the small signal model of the reactive power control.

The block diagram of the small signal model for the active power control of (1,4) is demonstrated in Figure 1-8. As seen in (1,10), time constant of the closed loop control can only be adjusted by tuning D_P. On the other hand, as seen in (1,4), D_P also affects the DG frequency. Thus, a basic tradeoff exists between the time constant of the control system and the frequency regulation.

As opposed to the active load sharing technique, the conventional droop method can be implemented with no communication links, and therefore, is more reliable. However, it has some drawbacks as listed below:

- Since there is only one control variable for each droop characteristic, e.g., D_P for frequency droop characteristic, it is impossible to satisfy more than one control objective. As an example, a design tradeoff needs to be considered between the time constant of the control system and the voltage and frequency regulation [47]-[48].
- The conventional droop method is developed assuming highly inductive effective impedance between the VCVSI and the AC bus. However, this assumption is challenged in microgrid applications since low-voltage transmission lines are mainly resistive. Thus, (1,3) is not valid for microgrid applications [12], [45].
- As opposed to the frequency, the voltage is not a global quantity in the microgrid. Thus, the reactive power control in (1,4) may adversely affect the voltage regulation for critical loads [45].
- In case of nonlinear loads, the conventional droop method is unable to distinguish the load current harmonics from the circulating current. Moreover, the current harmonics

distorts the DG output voltage. The conventional droop method can be modified to reduce the total harmonic distortion (THD) of the output voltages [49]-[52].

These potential drawbacks have been widely discussed in the literature. Proposed solutions are discussed here.

Adjustable Load Sharing Method

In this technique, the time constant of the proposed active and reactive power controllers can be adjusted without causing any impact on the DG voltage and frequency [47]. The proposed active power controller uses the conventional controller in (1,4); however, the phase angle of the VCVSI, δ , in Figure 1-7 is determined by

$$\delta = K_p \int \omega dt, \tag{1,11}$$

where K_p is an integral gain. Given (1,11), the small signal model of the proposed controller can be derived as

$$\Delta P(s) = \frac{K_p G}{s + K_p D_P G} \Delta \omega^*(s), \tag{1,12}$$

where G is defined in (1,8). Block diagram of this model is illustrated in Figure 1-9. The eigenvalue of the linearized control system of (1,12) is

$$\lambda = -K_p D_P G\,. \tag{1,13}$$

Equation (1,13) shows this eigenvalue depends on the integral gain, K_p, and the droop coefficient, D_p. Therefore, the closed loop time constant can be directly adjusted by tuning K_p. Since D_p is remained intact, the resulting frequency of the active power control in (1,4) will no longer be affected by the controller time constant adjustment.

Similarly, at the operating point of V_{com0}, E_0, and δ_0 the small signal control for the reactive power control in (1,4) can be found by perturbing (1,3) and (1,4)

$$\Delta Q(s) = \frac{H}{1 + D_Q H} \Delta E^*(s), \tag{1,14}$$

where

$$H = \frac{V_{com0}\cos\delta_0}{Z}. \tag{1,15}$$

As seen in (1,14), ΔQ is a linear function of a reference signal, ΔE^*. Since H is a function of δ_0, line impedance, and the operating point, performance of the conventional reactive power control in (1,4) tightly depends on the microgrid operational parameters. In the adjustable reactive power sharing method, an integral controller is used that regulates the common bus voltage in Figure 1-7, V_{com}, to match a reference voltage, V_{ref}[47]

$$E = K_q \int (V_{ref} - V_{com})dt\ , \tag{1,16}$$

where K_q is the integral gain and

$$V_{ref} = E^* - D_Q Q\ . \tag{1,17}$$

In steady state, V_{com} and V_{ref} are equal. Moreover, the steady state reactive power can be calculated as

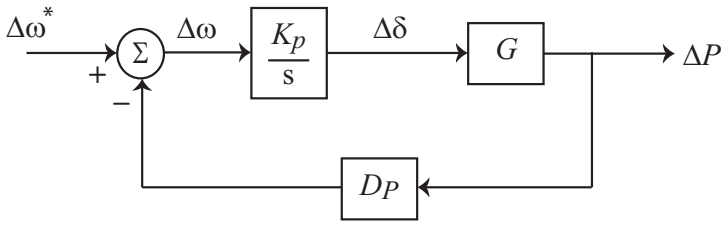

Figure 1-9 The Small Signal Model of the Adjustable Active Power Control [47]

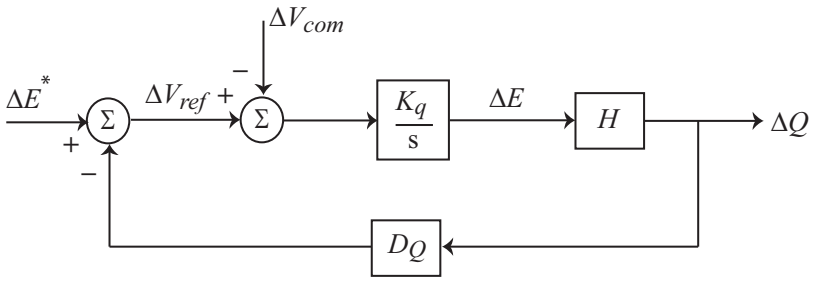

Figure 1-10 The Small Signal Model of the Adjustable Reactive Power Control [47]

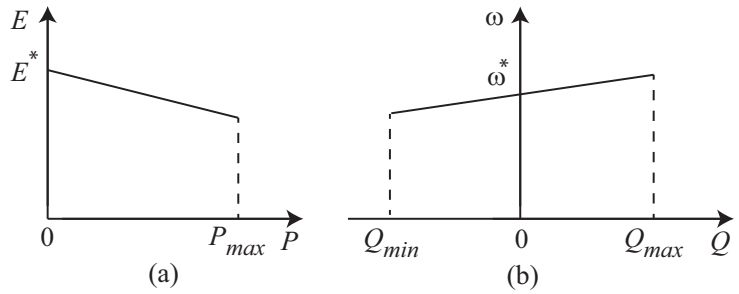

Figure 1-11 Droop/boost characteristics for low-voltage microgrids: (a) voltage-active power droop characteristic, (b) frequency-reactive power boost characteristic.

$$Q = \frac{E^* - V_{com}}{D_Q}. \tag{1,18}$$

Thus, as opposed to (1,14) and (1,15), microgrid operational parameters will no longer affect the reactive power control. Additionally, voltage regulation of the common bus is guaranteed. The small signal model for the proposed reactive power control is shown in Figure 1-10 and is expressed by

$$\Delta Q(s) = \frac{k_q H}{s + k_q D_Q H}\Delta E^*(s) - \frac{k_q H}{s + k_q D_Q H}\Delta V_{com}(s). \tag{1,19}$$

The closed loop transfer function of (1,19) is a function of both k_q and D_Q. Therefore, the dynamic response of the proposed reactive power control can be directly adjusted by k_q. Since D_Q is remained intact, the resulting voltage of the reactive power control in (1,4) will no longer be affected by the controller time constant adjustment.

VPD/FQB Droop Method

Low voltage transmission lines are basically resistive. Thus, one can consider a resistive effective line impedance, i.e., $\theta = 0^\circ$, and also can assume the δ to be small enough that $\sin\delta \approx \delta$. Considering these assumptions, (1,2) can be simplified as

$$\begin{cases} P \approx \dfrac{V_{com}E - V_{com}^2}{Z}, \\ Q \approx -\dfrac{V_{com}E}{Z}\delta. \end{cases} \tag{1,20}$$

Thus, the voltage-active power droop and frequency-reactive power boost (VPD/FQB) characteristics are alternatively considered [40]

$$\begin{cases} E = E^* - D_P P, \\ \omega = \omega^* + D_Q Q, \end{cases} \tag{1,21}$$

where E^* and ω^* are the output voltage amplitude and angular frequency of the DG at no-load condition, respectively. D_P and D_Q are the droop and boost coefficients, respectively.

Droop and boost characteristics of VPD/FQB method are shown in Figure 1-11. This approach offers an improved performance for controlling low-voltage microgrids with highly resistive transmission lines. However, it strongly depends on system parameters and this dependency confines its application. Additionally, the VPD/FQB technique may face a malfunction in the presence of nonlinear loads and cannot guarantee the voltage regulation. Similar to the adjustable load sharing method, the VPD/FQB technique can be modified to adjust the controller time constant without causing voltage and frequency deviation [47]-[48]. In the VPD control mode, the common bus voltage, V_{com}, is controlled to follow a reference voltage, V_{ref}.

$$E = (K_{P1} + \frac{K_{I1}}{s})(V_{ref} - V_{com}), \tag{1,22}$$

where

$$V_{ref} = E^* - D_P P, \tag{1,23}$$

and K_{P1} and K_{I1} are the proportional and integral gains of the active power controller, respectively. In steady state,

$$V_{com} = V_{ref} = E^* - D_P P\,. \tag{1,24}$$

In the FQB control mode, δ is determined by another proportional-integral (PI) controller as

$$\delta = (K_{P2} + \frac{K_{I2}}{s})\,\omega, \tag{1,25}$$

where K_{P2} and K_{I2} are the proportional and integral gains of the reactive power controller, respectively. In the modified VPD/FQB method, the time constants of the closed loop controllers are directly adjusted by the proportional and integral gains, K_{P1}, K_{I1}, K_{P2}, and K_{I2}.

Virtual Frame Transformation Method

An orthogonal linear transformation matrix, $\mathbf{T}_{PQ}$, is used to transfer the active/reactive powers to a new reference frame where the powers are independent of the effective line impedance [53]-[55]. For the system shown in Figure 1-7, $\mathbf{T}_{PQ}$ is defined as

$$\begin{bmatrix} P' \\ Q' \end{bmatrix} = \mathbf{T}_{PQ} \begin{bmatrix} P \\ Q \end{bmatrix} = \begin{bmatrix} \sin\theta & -\cos\theta \\ \cos\theta & \sin\theta \end{bmatrix} \begin{bmatrix} P \\ Q \end{bmatrix}. \tag{1,26}$$

The transformed active and reactive powers, P' and Q', are then used in droop characteristics in (1,4). The block diagram of this technique is shown in Figure 1-12.

Similarly, a virtual frequency/voltage frame transformation is defined as

$$\begin{bmatrix} \omega' \\ E' \end{bmatrix} = \mathbf{T}_{\omega E} \begin{bmatrix} \omega \\ E \end{bmatrix} = \begin{bmatrix} \sin\theta & \cos\theta \\ -\cos\theta & \sin\theta \end{bmatrix} \begin{bmatrix} \omega \\ E \end{bmatrix}, \tag{1,27}$$

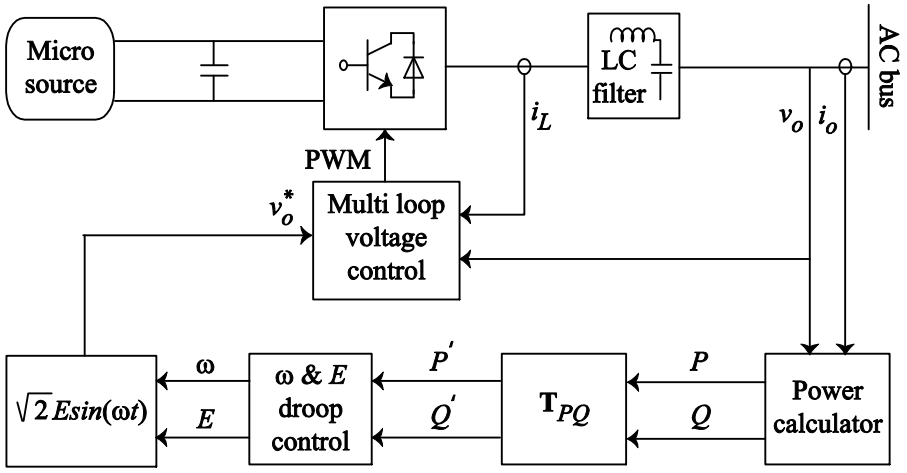

Figure 1-12 Droop Method with Virtual Power Frame Transformation

where E and ω are calculated through the conventional droop equations in (1,4). The transformed voltage and frequency, E' and ω', are then used as reference values for the VCVSI voltage control loop [56]-[58]. The virtual frame transformation method decouples the active and reactive power controls. However, the applied transformation requires a prior knowledge of the effective line impedance. Moreover, the control method does not consider possible negative impacts of nonlinear loads, does not ensure a regulated voltage, and comprises a basic tradeoff between the control loop time constant adjustment and voltage/frequency regulation.

Virtual Output Impedance

An intermediate control loop can be adopted to adjust the output impedance of the VCVSIs [12], [41], and [59]. In this control loop, as depicted in Figure 1-13, the VCVSI output voltage reference, v_{ref}, is proportionally drooped with respect to the output current, i_o, i.e.,

$$v_{ref} = v_o^* - Z_V(s) i_o, \tag{1,28}$$

where $Z_V(s)$ is the virtual output impedance, and v_o^* is the output voltage reference that is obtained by the conventional droop techniques in (1,4). If $Z_V(s)=sL_V$ is considered, a virtual output inductance is emulated for the VCVSI. In this case, the output voltage reference of the VCVSI is drooped proportional to the Derivative of its output current. In the presence of nonlinear loads, the harmonic currents can be properly shared by modifying (1,28) as

$$v_{ref} = v_o^* - s\sum L_{Vh} I_h, \tag{1,29}$$

where I_h is the h^{th} current harmonic, and L_{Vh} is the inductance associated with I_h. L_{Vh} values need to be precisely set to effectively share the current harmonics[38].

Since the output impedance of the VCVSI is frequency dependent, in the presence of nonlinear loads, THD of the output voltage would be relatively high. This can be mitigated by using a high-pass filter instead of sL_V in (1,28)

$$v_{ref} = v_o^* - L_V \frac{s}{s+\omega_c} i_o \tag{1,30}$$

where ω_c is the cutoff frequency of the high-pass filter [41].

If the virtual impedance, Z_V, is properly adjusted, it can prevent occurrence of current spikes when the DG is initially connected to the microgrid. This soft starting can be facilitated by considering a time-variant virtual output impedance as

$$Z_V(t) = Z_f - (Z_f - Z_i)e^{-t/T}, \tag{1,31}$$

where Z_i and Z_f are the initial and final values of the virtual output impedance, respectively. T is the time constant of the start up process [31].

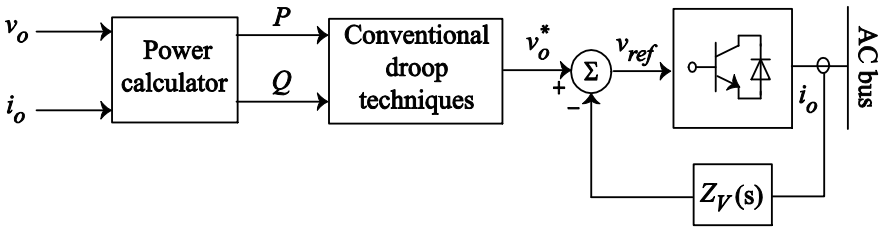

Figure 1-13 Block Diagram of the Virtual Output Impedance Method [41]

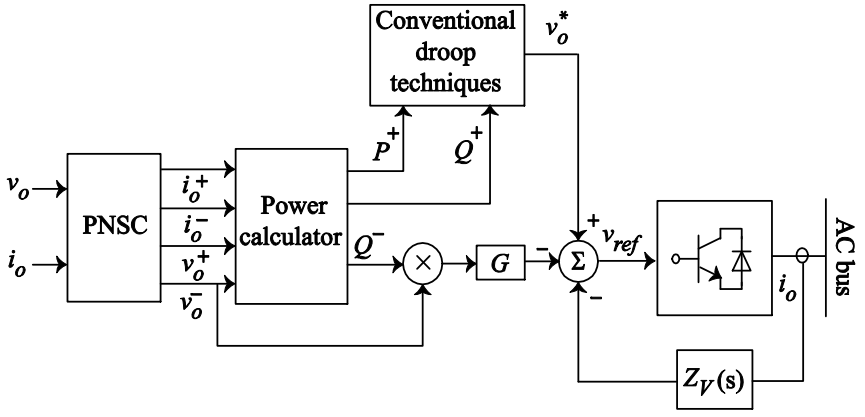

Figure 1-14 Virtual Output Impedance with Voltage Unbalance Compensator

Most recently, the virtual output impedance method has been modified for voltage unbalance compensation, caused by the presence of unbalanced loads in the microgrid [60]. The block diagram of the modified virtual output impedance method is shown in Figure 1-14. As can be seen, the measured DG output voltage and current are fed into the positive and negative sequence calculator (PNSC). Outputs of the PNSC, i_o^+, i_o^-, v_o^+, and v_o^-, are used to find the positive and negative sequence of the DG active and reactive power. The negative sequence of the reactive power, Q^-, is multiplied by the v_o^- and then a constant gain, G. The result is then used to find the voltage reference. The constant gain G needs to be fine-tuned to minimize the voltage unbalance without compromising the closed-loop stability.

The virtual output impedance method alleviates the dependency of the droop techniques on system parameters. Additionally, this control method properly operates in the presence of nonlinear loads. However, this method does not guarantee the voltage regulation, and, adjusting the closed loop time constant may result in an undesired deviation in the DG voltage and frequency.

Adaptive Voltage Droop Control

In this method, two terms are added to the conventional reactive power control in (1,4). Additional terms are considered to compensate for the voltage drop across the transmission lines that deliver power from the DG to critical loads. For a typical 2-DG system shown in Figure 1-15, the voltages at first and second buses are

$$V_i\angle\alpha_i = E_i\angle\delta_i - (r_i + jx_i)(I_i\angle-\theta_i), \quad i = 1,2, \tag{1,32}$$

where $I_i\angle-\theta_i$ is the output current of the i^{th} DG. Using (1,4) one can write

$$V_i = E_i^* - D_{Qi}Q_i - r_iI_i\cos\gamma_i - x_iI_i\sin\gamma_i, \tag{1,33}$$

where $\gamma_i = \alpha_i + \theta_i$. The bus voltage of the i^{th} DG can also be formulated in terms of its active and reactive powers, P_i and Q_i, as

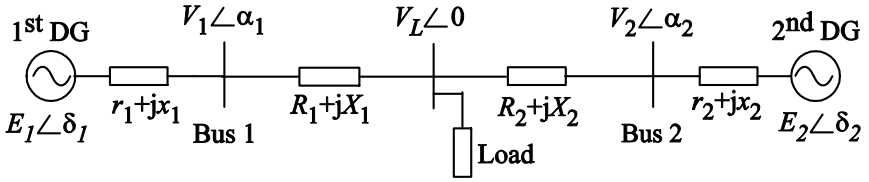

Figure 1-15 A Typical Two-DG System

$$V_i = E_i^* - D_{Qi}Q_i - \frac{r_i P_i}{E_i^*} - \frac{x_i Q_i}{E_i^*}. \tag{1,34}$$

The terms $r_i P_i / E_i^*$ and $x_i Q_i / E_i^*$ represent the voltage drop on the internal impedance r_i+jx_i. These terms can be incorporated in the conventional reactive power control of (1,4) to compensate for the voltage drops on the transmission lines as

$$E_i = E_i^* + (\frac{r_i P_i}{E_i^*} + \frac{x_i Q_i}{E_i^*}) - D_{Qi}Q_i. \tag{1,35}$$

Although, the reactive power control in (1,35) improves the voltage regulation of the farther buses, it is still dependent on the active power control in (1,4). This problem is resolved by adopting the voltage droop coefficient as a nonlinear function of active and reactive powers [45]

$$\begin{cases} E_i = E_i^* + (\frac{r_i P_i}{E_i^*} + \frac{x_i Q_i}{E_i^*}) - D_i(P_i, Q_i)Q_i, \\ D_i(P_i, Q_i) = D_{Qi} + m_{Qi}Q_i^2 + m_{Pi}P_i^2, \end{cases} \tag{1,36}$$

where D_{Qi}, m_{Qi}, and m_{Pi} are droop coefficients. The terms $m_{Qi}Q_i^2$ and $m_{Pi}P_i^2$ mitigate the negative impacts of the active power control and the microgrid parameters on the reactive power control.

The adaptive droop method is particularly desirable when the voltage regulation of some buses is not feasible. The higher-order terms in (1,36) significantly improve the reactive power sharing under heavy loading conditions. The potential disadvantage, however, is the required prior knowledge of the transmission line parameters [45]. This control method is not fully functional in the presence of nonlinear loads. Moreover, given the basics discussed for the

adjustable load sharing method, adjusting the time constant may result in undesired deviations in DG voltage and frequency.

Signal Injection Method

In this approach, each DG injects a small AC voltage signal to the microgrid. Frequency of this control signal, ω_q, is determined by the output reactive power, Q, of the corresponding DG as

$$\omega_q = \omega_{q0} + D_Q Q, \tag{1,37}$$

where ω_{q0} is the nominal angular frequency of injected voltage signals and D_Q is the boost coefficient. The small real power transmitted through the signal injection is then calculated and the RMS value of the output voltage of the DG, E, is accordingly adjusted as

$$E = E^* - D_P p_q, \tag{1,38}$$

where E^* is the RMS value of the no-load voltage of the DG, and D_P is the droop coefficient. This procedure is repeated until all VCVSIs produce the same frequency for the control signal.

Here, this technique is elaborated for a system of two DGs shown in Figure 1-15. It is assumed that D_Q is the same for both DGs. Initially, first and second DGs inject low voltage signals to the system with the following frequencies

$$\begin{cases} \omega_{q1} = \omega_{q0} + D_Q Q_1, \\ \omega_{q2} = \omega_{q0} + D_Q Q_2. \end{cases} \tag{1,39}$$

Assuming $Q_1 > Q_2$

$$\Delta\omega = \omega_{q1} - \omega_{q2} = D_Q(Q_1 - Q_2) = D_Q \Delta Q. \tag{1,40}$$

The phase difference between the two voltage signals can be obtained as

$$\delta = \int \Delta\omega dt = D_Q \Delta Q t\,. \tag{1,41}$$

Due to the phase difference between the DGs, a small amount of active power flows from one to the other. Assuming inductive output impedances for DGs, the transmitted active power from DG1 to DG2, p_{q1}, is

$$p_{q1} = \frac{V_{q1}V_{q2}}{x_1 + x_2 + X_1 + X_2}\sin\delta, \tag{1,42}$$

where V_{q1} and V_{q2} are the RMS values of the injected voltage signals. Moreover, the transmitted active power in reverse direction, from DG2 to DG1, p_{q2}, is

$$p_{q2} = -p_{q1}. \tag{1,43}$$

The DG voltages are adjusted as

$$\begin{cases} E_1 = E^* - D_P p_{q1}, \\ E_2 = E^* - D_P p_{q2}. \end{cases} \tag{1,44}$$

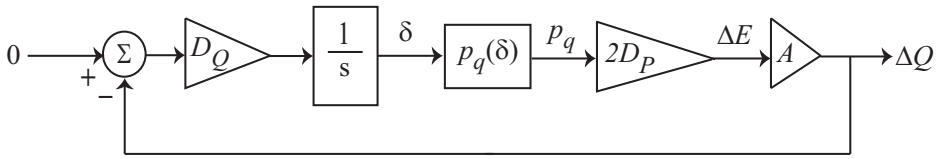

Figure 1-16 Block Diagram of the Signal Injection Method for Reactive Power Sharing [61]

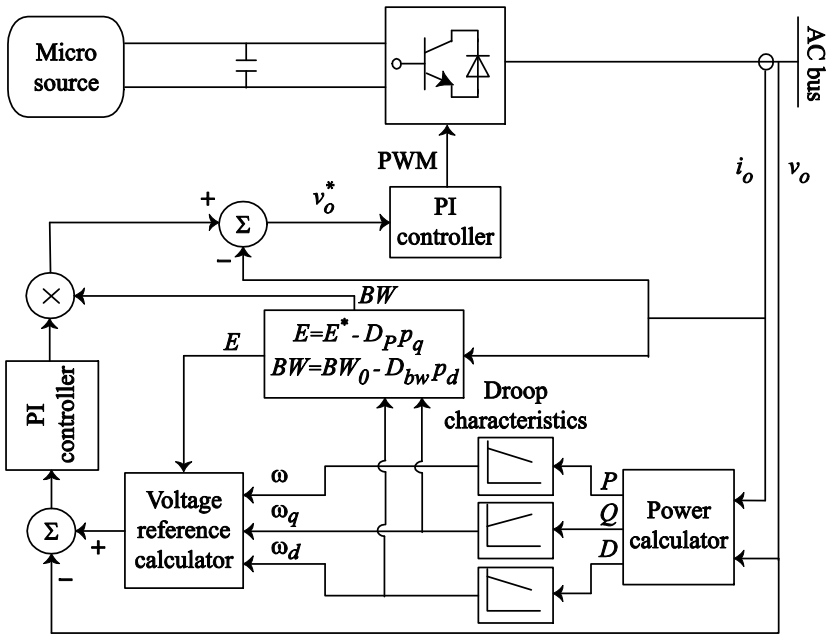

Figure 1-17 Block Diagram of the Updated Signal Injection Method [61]

Herein, it is assumed that D_P is the same for both DGs. The difference between the DGs output voltages is

$$\Delta E = E_1 - E_2 = -2D_P p_{q1}. \tag{1,45}$$

Thus, one can write

$$\begin{cases} \Delta Q = A\Delta E, \\ A = 2V_L \dfrac{\sin\varphi}{|Z|} - V_L \dfrac{\sin(\varphi+\delta)}{|Z|}, \\ r_1 + R_1 + j(x_1 + X_1) = r_2 + R_2 + j(x_2 + X_2) = |Z| \angle \varphi, \end{cases} \tag{1,46}$$

where V_L is the load voltage. The block diagram of the proposed controller is shown in Figure 1-16.

In the presence of nonlinear loads, parallel DGs can be controlled to participate in supplying current harmonics by properly adjusting the voltage loop bandwidth [61]. For that, first, frequency of the injected voltage is drooped based on the total distortion power, D

$$\begin{cases} \omega_d = \omega_{d0} - mD, \\ D = \sqrt{S^2 - P^2 - Q^2}, \end{cases} \tag{1,47}$$

where ω_{d0} is the nominal angular frequency of the injected voltage signals, m is the droop coefficient, and S is DG nominal power. A procedure similar to (1,39) to (1,42) is adopted to calculate the power transmitted by the injected signal, p_d. The bandwidth of VCVSI voltage loop is adjusted as

$$BW = BW_0 - D_{bw} p_d, \tag{1,48}$$

where BW_0 is the nominal bandwidth of the voltage loop and D_{bw} is the droop coefficient. The block diagram of the signal injection method is shown in Figure 1-17.

Signal injection method properly controls the reactive power sharing, and is not sensitive to variations in the line impedances [61]-[62]. It also works for linear and nonlinear

loads, and over various operating conditions. However, it does not guarantee the voltage regulation.

Nonlinear Load Sharing

Some have challenged the functionality of droop techniques in the presence of nonlinear loads [50]-[52]. Two approaches for resolving this issue are discussed here. In the first approach [50], the DGs equally share the linear and nonlinear loads. For this purpose, each harmonic of the load current, I_h, is sensed to calculate the corresponding voltage droop harmonic, V_h, at the output terminal of the DG. The voltage harmonics are compensated by adding 90° leading signals, corresponding to each current harmonic, to the DG voltage reference. Therefore, the real and imaginary parts of the voltage droop associated with each current harmonic are

$$\begin{cases} \mathrm{Re}(V_h) = -k_h \,\mathrm{Im}(I_h), \\ \mathrm{Im}(V_h) = k_h \,\mathrm{Re}(I_h), \end{cases} \tag{1,49}$$

where k_h is the droop coefficient for the h^{th} harmonic. As a result, the output voltage THD is significantly improved.

In the second approach, the conventional droop method is modified to compensate for the harmonics of the DG output voltage. These voltage harmonics are caused by the distorted voltage drop across the VCVSI output impedance and are due to the distorted nature of the load current [52]. As shown in Figure 1-18, first, the DG output voltage and current are used to calculate the fundamental term and harmonics of the DG output active and reactive power, (P_1,Q_1) and (P_h,Q_h) respectively. It is noteworthy that distorted voltage and current usually do not carry even harmonics, and thus, h is usually an odd number. P_1 and Q_1, are fed to the conventional droop characteristics in (1,4) to calculate the fundamental term, v_o^*, of the VCVSI voltage reference, v_{ref}. As shown in Figure 1-18, to cancel out the output voltage harmonics, a set of droop characteristics are considered for each individual harmonic. Each set of droop characteristics determines an additional term to be included in the VCVSI output voltage

reference, v_{ref}, to cancel the corresponding voltage harmonic. Each current harmonic, I_h, is considered as a constant current source, as shown in Figure 1-19. In this figure, $E_h \angle \delta_h$ denotes a phasor for the corresponding Voltage signal that is included in the voltage reference, v_{ref}. $Z_h \angle \theta_h$ represents the VCVSI output impedance associated with the h^{th} current harmonic. The active and reactive powers delivered to the harmonic current source, P_h and Q_h, are

$$\begin{cases} P_h = E_h I_h \cos\delta_h - Z_h I_h^2 \cos\theta_h, \\ Q_h = E_h I_h \sin\delta_h - Z_h I_h^2 \sin\theta_h. \end{cases} \quad (1,50)$$

When δ_h is small enough (i.e. $\sin(\delta_h) = \delta_h$), P_h and Q_h are roughly proportional to E_h and θ_h, respectively. Therefore, the following droop characteristics can be used to eliminate the h^{th} DG output voltage harmonic

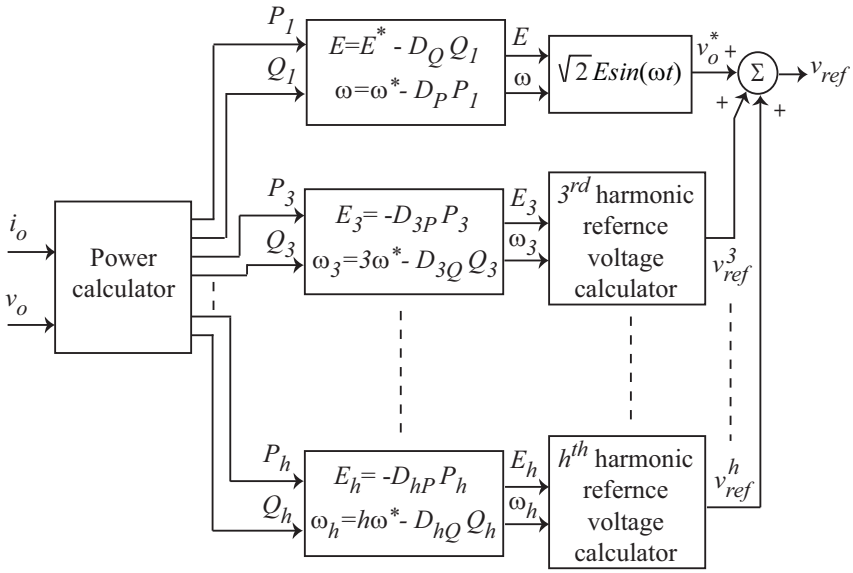

Figure 1-18 Control Block Diagram for the Harmonic Cancellation Technique

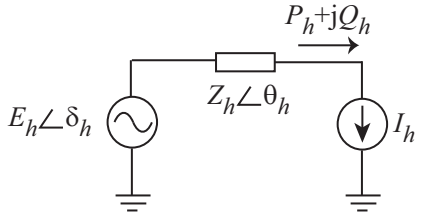

Figure 1-19 h^{th} Harmonic Equivalent Circuit of a DG

$$\begin{cases} \omega_h = h\omega^* - D_{hQ}Q_h, \\ E_h = -D_{hP}P_h, \end{cases} \quad h \neq 1, \tag{1,51}$$

where ω^* is the rated fundamental frequency of the microgrid. D_{hP} and D_{hQ} are the droop coefficients. As can be seen in Figure 1-18, the harmonic reference voltage, v_{ref}^h, for eliminating the h^{th} output voltage harmonic, can be formed with E_h and the phase angle generated from the integration of ω_h.

Primary control techniques are application specific and bring specific features. The active load sharing method provides tight current sharing and high power quality; however, it requires communication links and high bandwidth control loops. On the other hand, the droop methods provide local controls without any communication infrastructures. The potential advantages and disadvantages of the conventional droop method and its modifications are outlined in Table 1.1, based on which, following statements can be concluded:

- System identification is required to find the line parameters for some techniques, e.g., adaptive voltage droop or virtual frame transformation methods.
- Modified droop techniques, excluding the ones for low voltage microgrids, decouple the active and reactive power controls.
- Adjustable load sharing and adaptive voltage droop methods are the only techniques that offer voltage regulation.
- Nonlinear loads need to be accommodated with the complicated control techniques such as the virtual impedance, the signal injection, or the nonlinear load sharing methods to achieve a mitigated level of harmonics in the microgrid.

The adjustable load sharing is the only technique where the system time constant can be independently adjusted without affecting the DG voltage and frequency.

Table 1-1 The Potential Advantage and Disadvantages of the Discussed Droop Methods

Droop method	Potential advantages	Potential disadvantages
Conventional droop method [22], [43]	• Simple implementation.	• Affected by the system parameters. • Only functional for highly inductive transmission lines. • Cannot handle nonlinear loads. • Voltage regulation is not guaranteed. • Adjusting the controller speed for the active and reactive power controllers can affect the voltage and frequency controls.
Adjustable load sharing method [47]	• Adjusting the controller speed for the active and reactive power controllers without compromising the voltage and frequency controls. • Robust to the system parameter variations. • Improved voltage regulation.	• Cannot handle nonlinear loads.
VPD/FQB droop method [48]	• Simple implementation. • Adjusting the controller speed for the active and reactive power controllers without compromising the voltage and frequency controls.	• Affected by the system parameters. • Only functional for highly resistive transmission lines. • Cannot handle nonlinear loads.
Virtual frame transformation method [53]-[58]	• Simple implementation. • Decoupled active and reactive power controls.	• Cannot handle nonlinear loads. • The line impedances should be known a priori. • Adjusting the controller speed for the active and reactive power controllers can affect the voltage and frequency controls. • Voltage regulation is not guaranteed.
Virtual output impedance [12], [31], [41], [59]-[60]	• Simple implementation. • Not affected by the system parameters. • Functional for both linear and nonlinear loads. • Mitigates the harmonic distortion of the output voltage. • Can compensate for the unbalance of the DG output voltages.	• Adjusting the controller speed for the active and reactive power controllers can affect the voltage and frequency controls. • Voltage regulation is not guaranteed.
Adaptive voltage droop method [45]	• Improved voltage regulation. • Not affected by the system parameters.	• Cannot handle nonlinear loads. • Adjusting the controller speed for the active and reactive power controllers can affect the voltage and frequency controls. • System parameters should be known a priori.
Signal injection method [61]-[62]	• Functional for both linear and nonlinear loads. • Not affected by the system parameters.	• Complicated implementation. • Adjusting the controller speed for the active and reactive power controllers can affect the voltage and frequency controls. • Voltage regulation is not guaranteed.
Nonlinear load sharing techniques [50], [52]	• Properly shares the current harmonics between the DGs, and consequently, cancels out the voltage harmonics.	• Affected by the system parameters. • Poor voltage regulation for the case of precise reactive power sharing. • Adjusting the controller speed for the active and reactive power controllers can affect the voltage and frequency controls.

Secondary Control

Primary control, as discussed, may cause frequency and voltage deviation even in steady state. Although the storage devices can compensate for this deviation, they are unable to provide the power for load-frequency control in long terms due to their short energy capacity. The secondary control, as a centralized controller, restores the microgrid voltage and frequency and compensate for the deviations caused by the primary control. This control hierarchy is designed to have slower dynamics response than that of the primary, which, justifies the decoupled dynamics of the primary and the secondary control loops and facilitates their individual designs [63].

Figure 1-20 represents the block diagram of the conventional secondary control with a centralized control structure. As seen in this figure, frequency of the microgrid and the terminal voltage of a given DG are compared with the corresponding reference values, ω_{ref} and v_{ref}, respectively. Then, the error signals are processed by individual controllers as in (1,52); the resulting signals ($\delta\omega$ and δE) are sent to the primary controller of the DG to compensate for the frequency and voltage deviations [12]

$$\begin{cases} \delta\omega = K_{P\omega}(\omega_{ref} - \omega) + K_{I\omega}\int(\omega_{ref} - \omega)dt + \Delta\omega_s, \\ \delta E = K_{PE}(v_{ref} - E) + K_{IE}\int(v_{ref} - E)dt, \end{cases} \quad (1,52)$$

where $K_{P\omega}$, $K_{I\omega}$, K_{PE}, and K_{IE} are the controllers parameters. An additional term, $\Delta\omega_s$, is considered in frequency controller in (1,52) to facilitate synchronization of the microgrid to the main gird. In the islanded operating mode, this additional term is zero. However, during the synchronization, a PLL module is required to measure $\Delta\omega_s$ [64]-[68]. During the grid-tied operation, voltage and frequency of the main grid are considered as the references in (1,52).

Most recently, potential function-based optimization technique has been suggested for the secondary control [13]. In this method, a potential function is considered for each DG. This

function is a scalar cost function that carries all the information on the DG measurements, constraints, and control objectives as

$$\varphi_j(x_j) = w^u \sum_{i=1}^{n_u} p_i^u(x_j) + w^c \sum_{i=1}^{n_c} p_i^c(x_j) + w^g p_j^g(x_j), \quad (1,53)$$

where ϕ_j is the potential function related to each DG, and x_j comprises the measurements from the DG unit (e.g., voltage, current, real and reactive power). p_i^u denotes the partial potential functions that reflect the measurement information of the DG. p_i^c denotes the operation constraints that ensure the stable operation of microgrid. p_j^g is used to mitigate the DG measurements from the pre-defined set points. w^u, w^c, and w^g are the weighted factors for the partial potential functions.

The block diagram of the potential function-based technique is shown in Figure 1-21. In this technique, when the potential functions approach their minimum values, the microgrid is about to operate at the desired states. Therefore, inside the optimizer in Figure 1-21, set points of the DG are determined such that to minimize the potential functions, and thus, to meet the microgrid control objectives.

The potential function-based technique requires bidirectional communication infrastructure to facilitate data exchange from the DG to the optimizer (measurements) and vice versa (calculated set points). The data transfer links add propagation delays to the control signals. This propagation delay is tolerable, since the secondary controllers are slower than the primary ones.

The secondary control can also be designed to satisfy the power quality requirements, e.g., voltage balancing at critical buses [69]. Block diagram of the voltage unbalance compensator is shown in Figure 1-22. First, the critical bus voltage is transformed to the dq reference frame. Once the positive and negative sequence voltages for both d and q axis are calculated, one can find the voltage unbalance factor (VUF) as

$$VUF = 100\frac{\sqrt{(v_d^-)^2 + (v_q^-)^2}}{\sqrt{(v_d^+)^2 + (v_q^+)^2}}, \qquad (1,54)$$

where v_d^+ and v_d^- are the positive and negative sequence voltages of the direct component, and v_q^+ and v_q^- are the positive and negative sequence voltages of the quadrature component, respectively. As depicted in Figure 1-22, the calculated VUF is compared with the reference value, VUF*, and the difference is fed to a PI controller. The controller output is multiplied by the negative sequence of the direct and quadrature voltage components, v_d^- and v_q^-, and the results are added to the references of DG voltage controllers to compensate for the voltage unbalance.

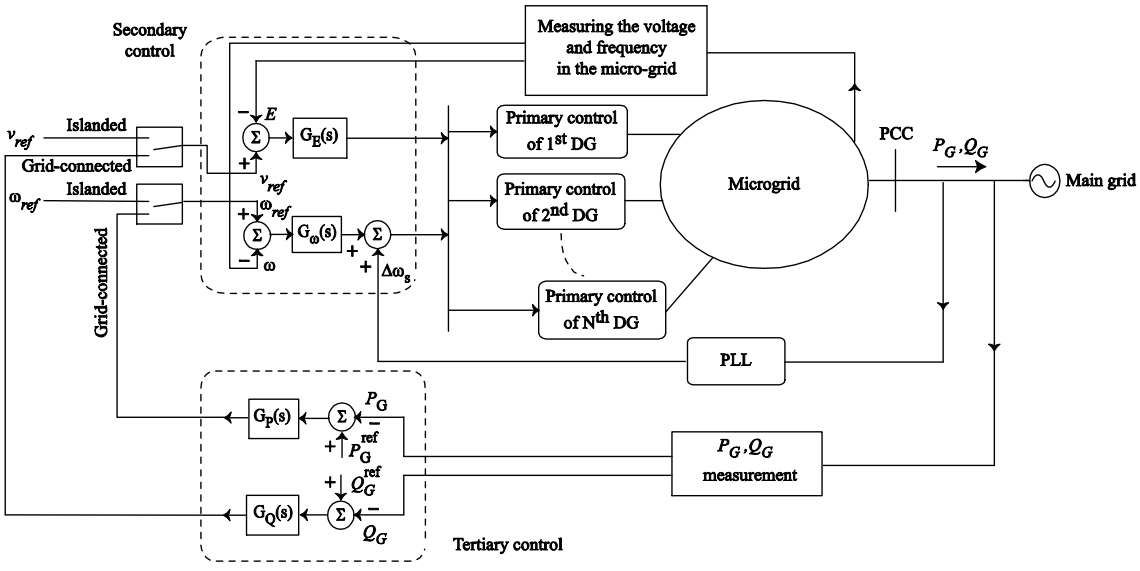

Figure 1-20 Block diagram of the secondary and tertiary controls [12].

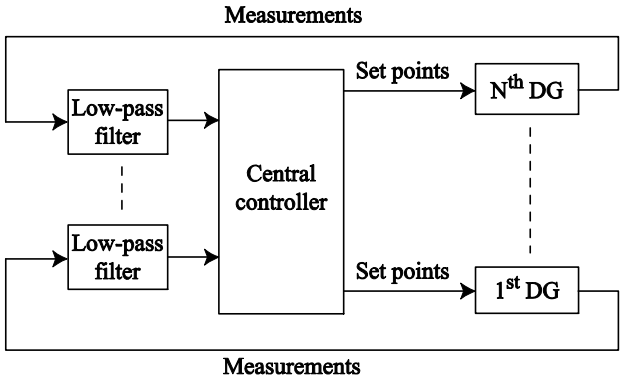

Figure 1-21 The Potential Function-Based Technique Block Diagram [13]

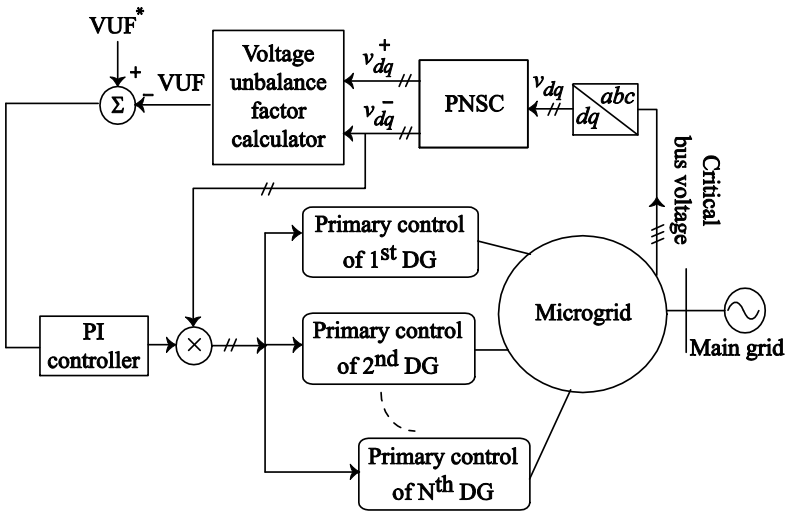

Figure 1-22 Voltage Unbalance Compensation in the Secondary Control

Tertiary Control

Tertiary control is the last (and the slowest) control level that considers the economical concerns in the optimal operation of the microgrid, and manages the power flow between microgrid and main grid [12]. In the grid-tied mode, the power flow between microgrid and main grid can be managed by adjusting the amplitude and frequency of DGs voltages. The block diagram of this process is shown in Figure 1-20. First, active and reactive output powers of the microgrid, P_G and Q_G, are measured. These quantities are then compared with the

corresponding reference values, P_G^{ref} and Q_G^{ref} , to obtain the frequency and voltage references, ω_{ref} and v_{ref} based on

$$\begin{cases} \omega_{ref} = K_{PP}(P_G^{ref} - P_G) + K_{IP}\int (P_G^{ref} - P_G)dt, \\ v_{ref} = K_{PQ}(Q_G^{ref} - Q_G) + K_{IQ}\int (Q_G^{ref} - Q_G)dt, \end{cases} \quad (1,55)$$

where K_{PP}, K_{IP}, K_{PQ}, and K_{IQ} are the controllers parameters [12]. ω_{ref} and v_{ref} are further used as the reference values to the secondary control, as in (1,52).

The tertiary control also provides an economically optimal operation, e.g., by using a gossiping algorithm. Generally, the economically optimal operation is satisfied if all the DGs operate at equal marginal costs (variation of the total cost with respect to the variation of the generated power), C_{opt}, [15], [70]-[75]. In the gossiping algorithm, initially, random output power set points, P_i^0 and P_j^0 , are considered for the i^{th} DG and its random gossiping partner, j^{th} DG, respectively. Then, considering the prior knowledge about the marginal cost curves of the DGs, the optimal output power of the two DGs, P_i^{opt} and P_j^{opt} , are determined. At this time, each of the two DGs changes its output power to generate at the optimal point. The aforementioned procedure is illustrated in Figure 1-23. The same procedure is repeated for other pairs of DGs until the whole DGs in the microgrid operate optimally. Additionally, evolutionary game theory-based techniques are proposed to facilitate the power management by local information, and thus, to simplify the required communication infrastructures [71].

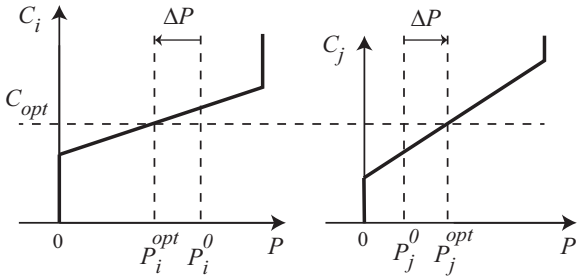

Figure 1-23 Marginal Cost Function Matching Between Two DGs [70]

Problem Definition

The traditional secondary control exploits a centralized control structure which is shown in Figure 1-20 and Figure 1-24(a). Central controllers command globally on the gathered system-wide information, and require a complex [12], [76] and in some cases two-way communication network [13] that adversely affects system flexibility and configurability and increases the reliability concerns by posing single point of failure. The single point of failure means that by the failure of the central controller, the whole control system fails down. In this dissertation, the distributed control structure, shown in Figure 1-24(b), is used to implement the secondary control of microgrids. A microgrid can be considered as a multi-agent system where its DGs are the energy nodes (agents). Figure 1-25 shows the multi-agent environment for a microgrid system with DGs as agents. The distributed structure of the communication network improves the system reliability. In this control structure, the control protocols are distributed on all DGs. Therefore, the requirement for a central controller is obviated and the control system does not fail down subsequent to outage of a single unit.

Over the last two decades, networked multi-agent systems have earned much attention due to their flexibility and computational efficiency. These systems are inspired by the natural phenomena such as swarming in insects, flocking in birds, thermodynamic laws, and synchronization and phase transitions in physical and chemical systems. In these phenomena, the coordination and synchronization process necessitates that each agent exchange information with other agents according to some restricted communication protocols [77]-[81].

The distributed cooperative control of multi-agent systems can be used to implement the secondary control of microgrids. The term “distributed” means that the controller requires a communication network by which each agent only receives the information of its neighboring agents. The term “cooperative” means that, in contrast to the competitive control, all agents act as one group towards a common synchronization goal and follow cooperative decisions [78]-[82]. Distributed cooperative control of multi-agent systems is mainly categorized into the

regulator synchronization problem and the tracking synchronization problem. In regulator synchronization problem, also called leaderless consensus, all agents synchronize to a common value that is not prescribed or controllable. In tracking synchronization problem, all agents synchronize to a leader node that acts as a command generator [83]-[85]. Neighboring agents can communicate with each other. The leader is only connected to a small portion of the agents [83].

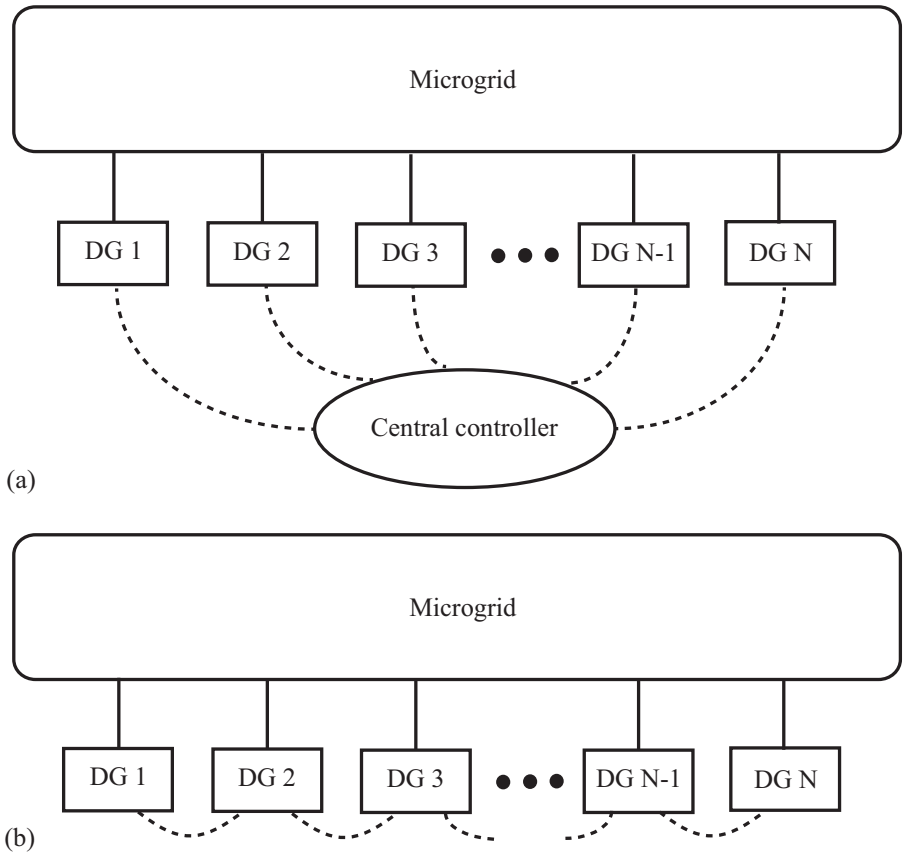

Figure 1-24 The Secondary Control Structures: (a) Centralized and (b) Distributed.

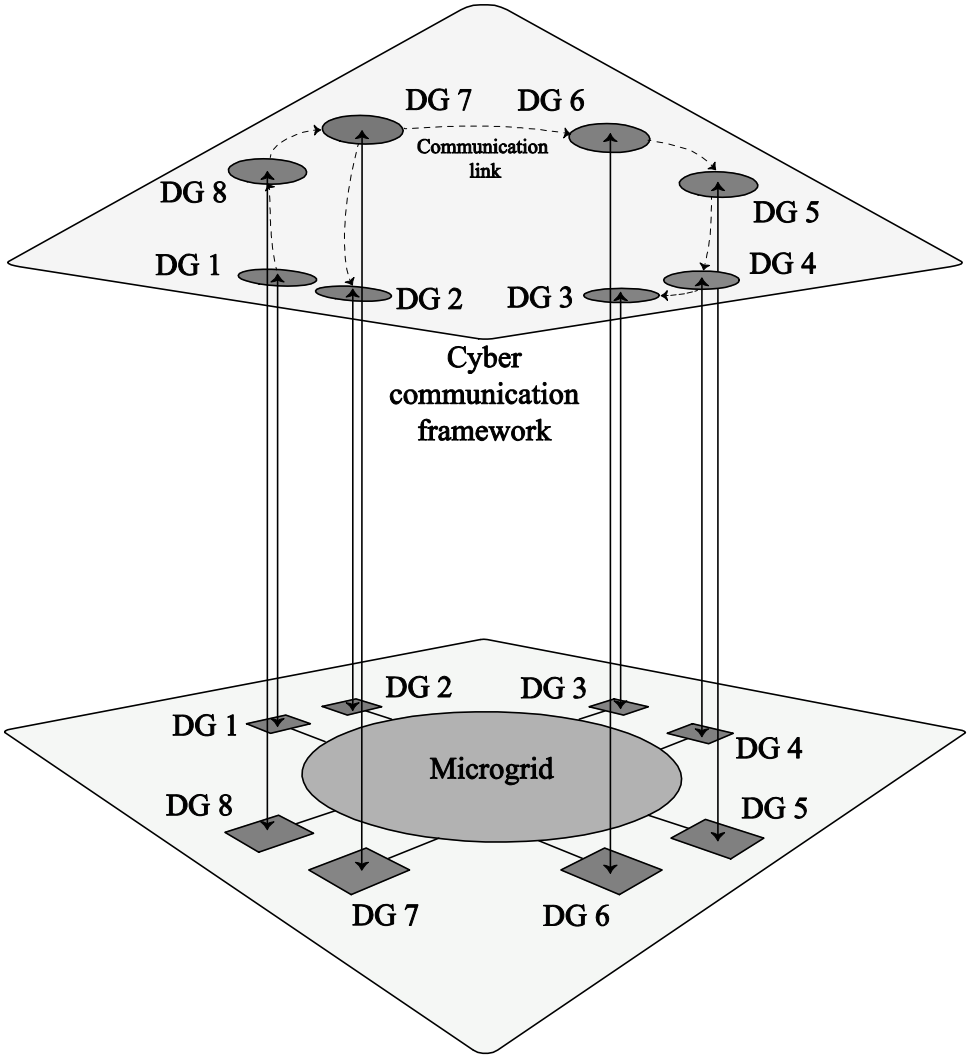

Figure 1-25 Multi-Agent Environment for a Microgrid System with DGs as Agents

The secondary control of microgrids is similar to the tracking synchronization problem of a multi-agent system where the DG voltages and frequencies are required to track their nominal values. The dynamics of DGs in microgrids are nonlinear and non-identical. Therefore, input-output feedback linearization is used to transform the nonlinear heterogeneous dynamics of DGs to linear dynamics. Input-output feedback linearization transforms the secondary voltage control to a second order tracking synchronization problem. The secondary frequency control is transformed to a first order synchronization problem using input-output feedback linearization.

Based on the transformed dynamics, fully distributed voltage and frequency control protocols are derived for each DG. The proposed distributed controls are implemented through a sparse communication network, with only one-way communication links, where each DG requires its own information and the information of its neighbors.

The DGs can be of rotating machinery or voltage source inverter (VSI) based types. The control structure of a VSI may vary based on the control objectives such as voltage and frequency, or active and reactive power. VCVSIs have internal voltage and current controller loops that facilitate the voltage and frequency control of DG. However, in some DGs, the sole active and reactive power control may be of interest. This requirement can be satisfied through the current controlled voltage source inverters (CCVSI). Up to this point, most of the presented secondary control schemes have only covered the voltage and frequency control of VCVSIs. In this dissertation, a two-layer control framework is proposed to implement the secondary control for an islanded microgrid containing both VCVSIs and CCVSIs. The first control layer deals with the voltage and frequency control of VCVSIs. Additionally, the active and reactive power of VCVSIs are allocated based on their active and reactive power ratings. The second control layer objectives are to control the active and reactive power of CCVSIs. Each control layer is implemented through the distributed control of multi-agent systems.

The distributed secondary voltage control of microgrids can be made adaptive with respect to the changes in the DG parameters and microgrid operating conditions. The term adaptive refers to the following salient features of the proposed controller. The proposed controller compensates for the nonlinear and uncertain dynamics of DGs and, hence, obviates the control design challenges caused by the nonlinear dynamics of DGs. The controller is fully independent of the DG parameters and the specification of the connector by which each DG is connected to the microgrid. Therefore, the controller can be deployed on any DG regardless of the DG parameters and the connector specifications and its performance does not deteriorate by the change in DG parameters (e.g., due to aging and thermal effects). The proposed

controller appropriately responds to the changes in the system operating condition, without any manual intervention, and adjusts the control parameters in real time. Linear-in-parameter neural networks (NN) can be used to design an adaptive and distributed secondary voltage control. Neural networks are used to compensate for the uncertainties caused by the unknown dynamics of DGs. The NN weights are the control parameters, and are calculated in realtime. DGs are considered as agents that can communicate with each other through a communication network.

Based on the above elaborated problems, the research objectives of this dissertation are summarized as follows.

- To propose a distributed secondary voltage control based on the cooperative control of multi-agent systems.
- To propose a distributed secondary frequency control based on the cooperative control of multi-agent systems.
- To develop a two-layer multi-objective control frame work for microgrids containing both VCVSIs and CCVSIs.
- To present an adaptive and distributed secondary voltage control that is adaptive with respect to the changes in the DG parameters.

Dissertation Outline

The rest of the dissertation is organized as follows.

In Chapter 2, the distributed secondary voltage control of microgrids is discussed. The Lyapunov technique is used to design a fully distributed voltage control. A microgrid test system is used to verify the effectiveness of the proposed voltage control.

In Chapter 3, the distributed secondary frequency control of microgrids is proposed. The distributed frequency control synchronizes the frequency of the microgrid to the nominal frequency and shares the active power of DGs according to their active power ratings. The effectiveness of the proposed frequency control is verified by simulating a microgrid test system.

In chapter 4, a two-layer control framework is proposed to implement the secondary control for an islanded microgrid containing both VCVSIs and CCVSIs. The first control layer deals with the voltage and frequency control of VCVSIs. Additionally, the active and reactive power of VCVSIs should be allocated based on their active and reactive power ratings. The second control layer objectives are to control the active and reactive power of CCVSIs. Based on the dynamical models of VCVSIs and CCVSIs, distributed control protocols for VCVSIs and CCVSIs are designed. Finally, the proposed control framework is verified using a microgrid test system and IEEE 34 bus test feeder.

Chapter 5 exploits neural networks to design an adaptive secondary voltage control based on the distributed cooperative control. The proposed control is adaptive with respect to the changes in the microgrid parameters and operating conditions. The proposed control is verified using a microgrid test system.

Chapter 6 summarizes and concludes the paper and recommends the future research works that extend the proposed materials in this dissertation.

Chapter 2

Distributed Secondary Voltage Control of Microgrids

Introduction

The secondary voltage control restores the microgrid operating voltage to the nominal voltage subsequent to disturbances such as islanding process. The dynamics of DGs in a microgrid are nonlinear and may be non-identical. The secondary voltage control resembles the tracking synchronization problem of a multi-agent system with nonlinear and non-identical dynamics. Therefore, to design a distributed secondary voltage control, the tracking synchronization problem for a nonlinear and non-identical multi-agent system must be solved [86]. Distributed cooperative control for multi-agent systems with nonlinear or non-identical dynamics has been recently introduced in the literature [87]-[89]. In this chapter, input-output feedback linearization is used to solve this problem. Input-output feedback linearization transforms the nonlinear and heterogeneous dynamics of DGs to linear dynamics. Thus, the secondary voltage control is transformed to a second-order tracking synchronization problem [90]. The Lyapunov technique is then adopted to derive fully distributed control protocols for each DG.

This chapter is organized as follows. First, the dynamical model of inverter-based DGs is presented. Then, input-output feedback linearization is adopted to design a secondary voltage control based on distributed cooperative control. Finally, the proposed secondary control is verified using a microgrid test system.

Large Signal Dynamical Model of an Inverter-based Distributed Generator

The proposed secondary voltage control is designed based on the large-signal nonlinear dynamical model of the DG. The block diagram of an inverter-based DG is shown in Figure 2-1. It contains an inverter bridge, connected to a primary dc power source (e.g., photovoltaic panels or fuel cells). The control loops, including the power, voltage, and current controllers, adjust the output voltage and frequency of the inverter bridge [91]-[93]. Given the

relatively high switching frequency of the inverter bridge, the switching artifacts can be safely neglected via average-value modeling. As stated in [91], dc-bus dynamics can be safely neglected, assuming an ideal source from the DG side.

It should be noted that the nonlinear dynamics of each DG are formulated in its own d-q (direct-quadrature) reference frame. It is assumed that the reference frame of the i^{th} DG is rotating at the frequency of ω_i. The reference frame of one DG is considered as the common reference frame with the rotating frequency of ω_{com}. The angle of the i^{th} DG reference frame, with respect to the common reference frame, is denoted as δ_i and satisfies the following differential equation

$$\dot{\delta}_i = \omega_i - \omega_{com}. \tag{2,1}$$

The power controller block, shown in Figure 2-2, contains the droop technique in (1,4), and provides the voltage references v^*_{odi} and v^*_{oqi} for the voltage controller, as well as the operating frequency ω_i for the inverter bridge. Two low-pass filters with the cut-off frequency of ω_{ci} are used to extract the fundamental component of the output active and reactive powers, denoted as P_i and Q_i, respectively. The differential equations of the power controller can be written as

$$\dot{P}_i = -\omega_{ci}P_i + \omega_{ci}(v_{odi}i_{odi} + v_{oqi}i_{oqi}), \tag{2,2}$$

$$\dot{Q}_i = -\omega_{ci}Q_i + \omega_{ci}(v_{oqi}i_{odi} - v_{odi}i_{oqi}), \tag{2,3}$$

where v_{odi}, v_{oqi}, i_{odi}, and i_{oqi} are the direct and quadrature components of v_{oi} and i_{oi} in Figure 2-1. As seen in Figure 2-2, the primary voltage control strategy for each DG aligns the output voltage magnitude on the d-axis of the corresponding reference frame. Therefore

$$\begin{cases} v^*_{odi} = E^*_i - D_{Qi}Q_i, \\ v^*_{oqi} = 0. \end{cases} \tag{2,4}$$

The block diagram of the voltage controller is shown in Figure 2-3 [92]-[93]. The differential algebraic equations of the voltage controller are written as

$$\dot{\phi}_{di} = v^*_{odi} - v_{odi}, \tag{2,5}$$

$$\dot{\phi}_{qi} = v^*_{oqi} - v_{oqi}, \tag{2,6}$$

$$i^*_{ldi} = F_i i_{odi} - \omega_b C_{fi} v_{oqi} + K_{PVi}(v^*_{odi} - v_{odi}) + K_{IVi}\phi_{di}, \tag{2,7}$$

$$i^*_{lqi} = F_i i_{oqi} + \omega_b C_{fi} v_{odi} + K_{PVi}(v^*_{oqi} - v_{oqi}) + K_{IVi}\phi_{qi}, \tag{2,8}$$

where ϕ_{di} and ϕ_{qi} are the auxiliary state variables defined for PI controllers in Figure 2-3, ω_b is the nominal angular frequency. Other parameters are shown in Figures 2-1 and 2-3.

The block diagram of the current controller is shown in Figure 2-4 [92]-[93]. The differential algebraic equations of the current controller are written as

$$\dot{\gamma}_{di} = i^*_{ldi} - i_{ldi}, \tag{2,9}$$

$$\dot{\gamma}_{qi} = i^*_{lqi} - i_{lqi}, \tag{2,10}$$

$$v^*_{idi} = -\omega_b L_{fi} i_{lqi} + K_{PCi}(i^*_{ldi} - i_{ldi}) + K_{ICi}\gamma_{di}, \tag{2,11}$$

$$v^*_{iqi} = \omega_b L_{fi} i_{ldi} + K_{PCi}(i^*_{lqi} - i_{lqi}) + K_{ICi}\gamma_{qi}, \tag{2,12}$$

where γ_{di} and γ_{qi} are the auxiliary state variables defined for the PI controllers in Figure 2-4. i_{ldi} and i_{lqi} are the direct and quadrature components of i_{li} in Figure 2-1. Other parameters are shown in Figures 2-1 and 2-4.

The differential equations for the output LC filter and output connector are as follows.

$$\dot{i}_{ldi} = -\frac{R_{fi}}{L_{fi}} i_{ldi} + \omega_i i_{lqi} + \frac{1}{L_{fi}} v_{idi} - \frac{1}{L_{fi}} v_{odi}, \tag{2,13}$$

$$\dot{i}_{lqi} = -\frac{R_{fi}}{L_{fi}} i_{lqi} - \omega_i i_{ldi} + \frac{1}{L_{fi}} v_{iqi} - \frac{1}{L_{fi}} v_{oqi}, \tag{2,14}$$

$$\dot{v}_{odi} = \omega_i v_{oqi} + \frac{1}{C_{fi}} i_{ldi} - \frac{1}{C_{fi}} i_{odi}, \tag{2,15}$$

$$\dot{v}_{oqi} = -\omega_i v_{odi} + \frac{1}{C_{fi}} i_{lqi} - \frac{1}{C_{fi}} i_{oqi}, \tag{2,16}$$

$$\dot{i}_{odi} = -\frac{R_{ci}}{L_{ci}} i_{odi} + \omega_i i_{oqi} + \frac{1}{L_{ci}} v_{odi} - \frac{1}{L_{ci}} v_{bdi}, \tag{2,17}$$

$$\dot{i}_{oqi} = -\frac{R_{ci}}{L_{ci}} i_{oqi} - \omega_i i_{odi} + \frac{1}{L_{ci}} v_{oqi} - \frac{1}{L_{ci}} v_{bqi}. \tag{2,18}$$

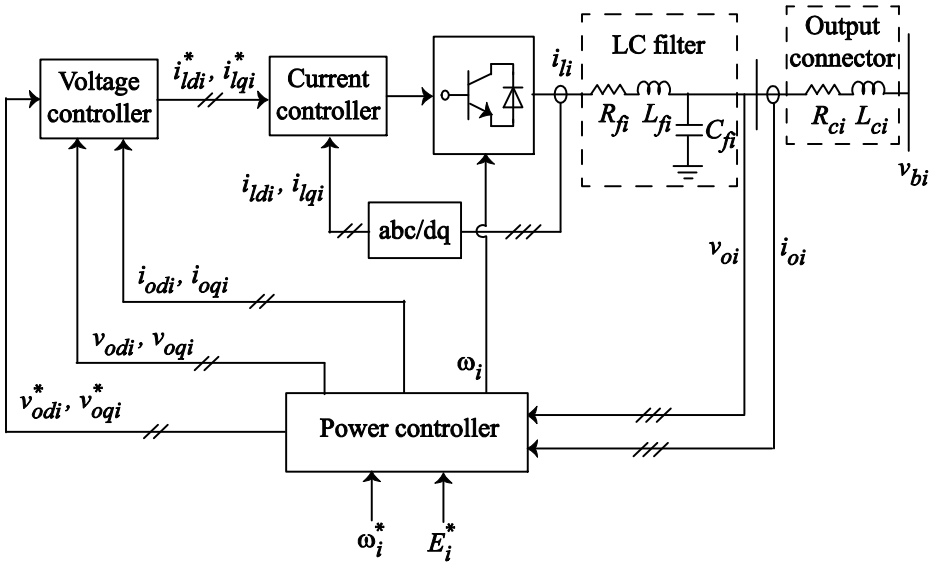

Figure 2-1 The Block Diagram of an Inverter-Based DG

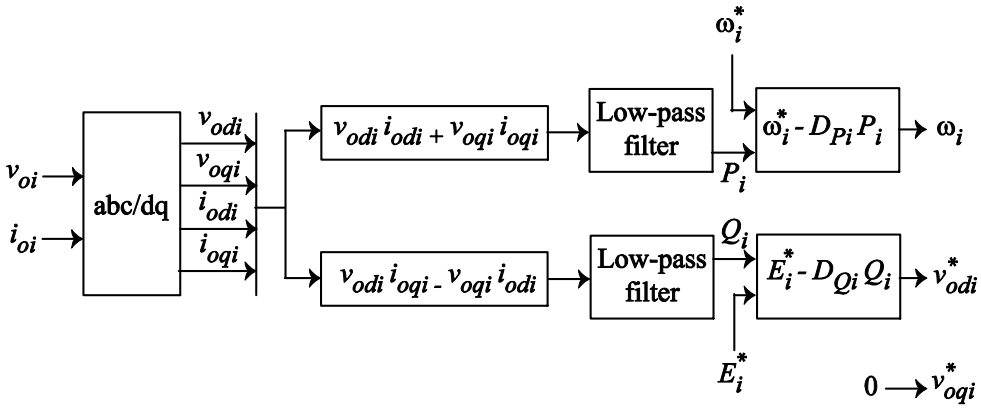

Figure 2-2 The Block Diagram of the Power Controller

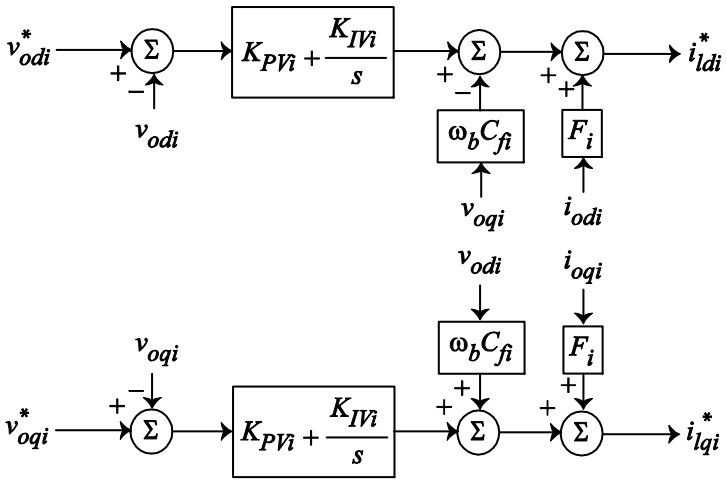

Figure 2-3 The Block Diagram of the Voltage Controller

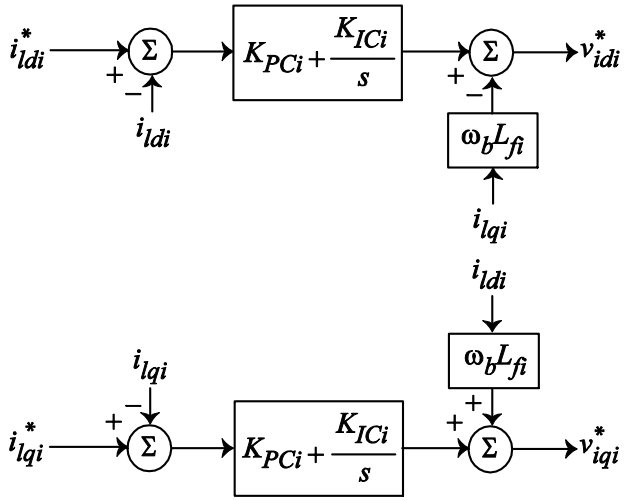

Figure 2-4 The Block Diagram of the Current Controller

Equations (2,1)-(2,18) form the large-signal dynamical model of the i^{th} DG. The large-signal dynamical model can be written in a compact form as

$$\begin{cases} \dot{x}_i = \mathbf{f}_i(x_i) + \mathbf{k}_i(x_i)\mathbf{D}_i + \mathbf{g}_i(x_i)u_i, \\ y_i = h_i(x_i), \end{cases} \tag{2,19}$$

where the state vector is

$$x_i = [\delta_i \quad P_i \quad Q_i \quad \phi_{di} \quad \phi_{qi} \quad \gamma_{di} \quad \gamma_{qi} \quad i_{ldi} \quad i_{lqi} \quad v_{odi} \quad v_{oqi} \quad i_{odi} \quad i_{oqi}]^T. \qquad (2,20)$$

The term $\mathbf{D}_i=[\omega_{com}\ v_{bdi}\ v_{bqi}]^T$ is considered as a known disturbance. The detailed expressions for $\mathbf{f}_i(x_i)$, $\mathbf{g}_i(x_i)$, and $\mathbf{k}_i(x_i)$ can be extracted from (2,1) to (2,18).

The secondary voltage control selects E_i^* in (1,4) such that the terminal voltage amplitude of each DG approaches its reference value, i.e. $v_{o,magi} \rightarrow v_{ref}$. If v_{ref} is set to the nominal voltage of microgrid $v_{nominal}$, the output voltage magnitude of VCVSIs synchronize to the nominal voltage of microgrid. However, v_{ref} can be chosen such that the voltage magnitude of a critical bus of microgrid synchronizes to $v_{nominal}$. In this case, v_{ref} is defined by

$$v_{ref} = k_{pc}(v_{nominal} - v_{c,mag}) + k_{ic}\int (v_{nominal} - v_{c,mag})dt, \qquad (2,21)$$

where $v_{c,mag}$ is the critical bus voltage magnitude and k_{pc} and k_{ic} are the control gains.

Since the amplitude of the DG output voltage is

$$v_{o,magi} = \sqrt{{v_{odi}}^2 + {v_{oqi}}^2}\ , \qquad (2,22)$$

and v_{oqi} is set to zero by the primary control as stated in (2,4), the synchronization of the voltage amplitude can be achieved by choosing the control input E_i^* such that $v_{odi} \rightarrow v_{ref}$. Therefore, for the secondary voltage control, the output and control input are set to $y_i=v_{odi}$ and $u_i = E_i^*$, respectively.

Secondary Voltage Control Based on Distributed Cooperative Control

A microgrid resembles a nonlinear and heterogeneous multi-agent system, where each DG is an agent. The secondary control of microgrids is a tracking synchronization problem, where all DGs try to synchronize their terminal voltage amplitude to pre-specified reference values. For this purpose, each DG only needs to communicate with its neighbors on the communication network. The required communication network can be modeled by a communication graph.

In this section, first, a preliminary on the graph theory is presented. Then, the secondary voltage control is implemented through input-output feedback linearization and distributed cooperative control of multi-agent systems. Finally, the communication network requirements for the proposed secondary voltage control are discussed.

Preliminary of Graph Theory

The communication network of a multi-agent cooperative system can be modeled by a directed graph (digraph). A digraph is usually expressed as $Gr=(V_G,E_G,A_G)$ with a nonempty finite set of N nodes $V_G=\{v_1,v_2,\ldots,v_N\}$, a set of edges or arcs $E_G \subset V_G \times V_G$, and the associated adjacency matrix $A_G=[a_{ij}] \in R^{N\times N}$. In a microgrid, DGs are considered as the nodes of the communication digraph. The edges of the corresponding digraph of the communication network denote the communication links.

An edge from node j to node i is denoted by (v_j,v_i), which means that node i receives the information from node j. a_{ij} is the weight of edge (v_j,v_i), and $a_{ij}>0$ if $(v_j,v_i) \in E_G$, otherwise $a_{ij}=0$. Node i is called a neighbor of node j if $(v_i,v_j) \in E_G$. The set of neighbors of node j is denoted as $N_j=\{i \mid (v_i,v_j) \in E_G\}$. For a digraph, if node i is a neighbor of node j, then node j can get information from node i, but not necessarily vice versa. The in-degree matrix is defined as $D=diag\{d_i\} \in R^{N\times N}$ with $d_i = \sum_{j\in N_i} a_{ij}$. The Laplacian matrix is defined as $L=D-A_G$. A direct path from node i to node j is a sequence of edges, expressed as $\{(v_i,v_k),(v_k,v_l),\ldots,(v_m,v_j)\}$. A digraph is said to have a spanning tree, if there is a root node with a direct path from that node to every other node in the graph [82].

Cooperative Secondary Voltage Control Based on Feedback Linearization and Tracking Synchronization Problem

As previously discussed, the secondary voltage control chooses appropriate control inputs E_i^* in (1,4) to synchronize the voltage magnitudes of DGs $v_{o,magi}$ to the reference voltage v_{ref}. The synchronization of the voltage magnitudes of DGs $v_{o,magi}$ is equivalent to synchronizing the direct term of output voltages v_{odi}. Therefore, the secondary voltage control should choose u_i

in (2,19) such that $y_i \rightarrow y_0, \forall i$, where $y_0 \equiv v_{ref}$.

Since the dynamics of DGs in a microgrid are nonlinear and might not be all identical, input-output feedback linearization can be used to facilitate the secondary voltage control design. In input-output feedback linearization, a direct relationship between the dynamics of the output y_i (or equivalently v_{odi}) and the control input u_i (or equivalently E_i^*) is generated by repetitively differentiating y_i with respect to time.

For the dynamics of the i^{th} DG in (2,19), the direct relationship between the y_i and u_i is generated after the 2nd derivative of the output y_i

$$\ddot{y}_i = L_{\mathbf{F}_i}{}^2 h_i + L_{\mathbf{g}_i} L_{\mathbf{F}_i} h_i u_i, \tag{2,23}$$

where

$$\mathbf{F}_i(x_i) = \mathbf{f}_i(x_i) + \mathbf{k}_i(x_i)\mathbf{D}_i. \tag{2,24}$$

$L_{\mathbf{F}_i} h_i$ is the Lie Derivative [94] of h_i with respect to $\mathbf{F}_i$, and is defined by $L_{\mathbf{F}_i} h_i = \nabla h_i \mathbf{F}_i = \frac{\partial(h_i)}{\partial \mathbf{x}_i} \mathbf{F}_i$.

$L_{\mathbf{F}_i}{}^2 h_i$ is defined by $L_{\mathbf{F}_i}{}^2 h_i = L_{\mathbf{F}_i}(L_{\mathbf{F}_i} h_i) = \frac{\partial(L_{\mathbf{F}_i} h_i)}{\partial \mathbf{x}_i} \mathbf{F}_i$.

An auxiliary control v_i is defined as

$$v_i = L_{\mathbf{F}_i}{}^2 h_i + L_{\mathbf{g}_i} L_{\mathbf{F}_i} h_i u_i. \tag{2,25}$$

Equations (2,23) and (2,25) result in the 2nd-order linear system

$$\ddot{y}_i = v_i, \forall i. \tag{2,26}$$

By choosing appropriate v_i, the synchronization for y_i is provided. The control input u_i is implemented by v_i as

$$u_i = (L_{\mathbf{g}_i} L_{\mathbf{F}_i} h_i)^{-1}(-L_{\mathbf{F}_i}{}^2 h_i + v_i). \tag{2,27}$$

In the following, the procedure for designing appropriate v_i is elaborated. First, equation (2,26) and the first derivative of y_i are written as

$$\begin{cases} \dot{y}_i \equiv y_{i,1}, \\ \dot{y}_{i,1} = v_i, \end{cases} \forall i. \tag{2,28}$$

or equivalently

$$\dot{\mathbf{y}}_i = \mathbf{A}\mathbf{y}_i + \mathbf{B}v_i, \forall i. \tag{2,29}$$

where $\mathbf{y}_i = [y_i \quad y_{i,1}]^T$, $\mathbf{B} = [0 \quad 1]^T$, and $\mathbf{A} = \begin{bmatrix} 0 & 1 \\ 0 & 0 \end{bmatrix}$.

Using input-output feedback linearization, the nonlinear dynamics of each DG in (2,19) are transformed to (2,29) and a set of internal dynamics. The commensurate reformulated dynamics of the reference generator can be expressed as

$$\dot{\mathbf{y}}_0 = \mathbf{A}\mathbf{y}_0, \tag{2,30}$$

where $\mathbf{y}_0 = [y_0 \quad \dot{y}_0]^T$. It should be noted that since $y_0 = v_{ref}$ is constant, $\dot{y}_0 = 0$.

It is assumed that DGs can communicate with each other through a communication network described by the digraph Gr. Based on the digraph Gr, the i^{th} DG may need to transmit $\mathbf{y}_i$ in (2,29) through the communication network. It is assumed that only one DG has the access to the reference $\mathbf{y}_0$ in (2,30) by a weight factor known as the pinning gain b_i. The secondary voltage control problem is to find a distributed v_i in (2,27) such that $\mathbf{y}_i \to \mathbf{y}_0, \forall i$. To solve this problem, the cooperative team objectives are expressed in terms of the local neighborhood tracking error

$$\mathbf{e}_i = \sum_{j \in N_i} a_{ij}(\mathbf{y}_i - \mathbf{y}_j) + b_i(\mathbf{y}_i - \mathbf{y}_0), \tag{2,31}$$

where a_{ij} denotes the elements of the communication digraph adjacency matrix. The pinning gain b_i is nonzero for one DG.

For a microgrid including N DGs, the global error vector for graph Gr is written from (2,31) as [82]

$$\mathbf{e} = \big((L+B)\otimes I_2\big)(\mathbf{Y} - \mathbf{Y}_0) \equiv \big((L+B)\otimes I_2\big)\boldsymbol{\delta}, \tag{2,32}$$

where $\mathbf{Y}=[\boldsymbol{y}_1^T \boldsymbol{y}_2^T \ldots \boldsymbol{y}_N^T]^T$, $\mathbf{e}=[\mathbf{e}_1^T \mathbf{e}_2^T \ldots \mathbf{e}_N^T]^T$, $\mathbf{Y}_0=\mathbf{1}_N\mathbf{y}_0$ ($\mathbf{1}_N$ is the vector of ones with the length of N.),

$B=diag\{b_i\}$, I_2 is the identity matrix with two rows and two columns, and $\boldsymbol{\delta}$ is the global disagreement vector. The Kronecker product is shown as $\otimes$ [95].$\dot{\mathbf{Y}}$ can be written as

$$\dot{\mathbf{Y}} = (I_N \otimes \mathbf{A})\mathbf{Y} + (I_N \otimes \mathbf{B})\mathbf{v}, \tag{2,33}$$

where $\mathbf{v}=[v_1 v_2 \ldots v_N]^T$ is the global auxiliary control vector. $\dot{\mathbf{Y}}_0$ can be written as

$$\dot{\mathbf{Y}}_0 = (I_N \otimes \mathbf{A})\mathbf{Y}_0. \tag{2,34}$$

The following definitions and lemmas are required for designing the auxiliary controls v_i.

Definition 1.1 [96]. $(\mathbf{A},\mathbf{B})$ are stabilizable if there exists a matrix S such that all eigenvalues of $\mathbf{A}$-$\mathbf{B}S$ have a strictly negative real part.

Definition 1.2 [96]. A matrix is Hurwitz if all of its eigenvalues have a strictly-negative real part.

Definition 1.3 [96]. A symmetric matrix P is positive definite if x^TPx is positive for all non-zero column vector x, and x^TPx is zero only for $x=0$.

Lemma 1.1 [80], [97]. Let $(\mathbf{A},\mathbf{B})$ be stabilizable**.** Let the digraph Gr have a spanning tree and $b_i \neq 0$ for one DG placed on a root node of the digraph Gr. Let λ_i $(i \in \{1,2,\ldots,\mathrm{N}\})$ be the eigenvalues of $L+B$. The matrix

$$\mathbf{H} = I_N \otimes \mathbf{A} - c(L+B) \otimes \mathbf{B}K, \tag{2,35}$$

with $c \in R$ and $K \in R^{l \times 2}$, is Hurwitz if and only if all the matrices $\mathbf{A}$-$c\lambda_i\mathbf{B}K, \forall i \in \{1,2,\ldots,\mathrm{N}\}$ are Hurwitz.

Lemma 1.2 [97]. Let $(\mathbf{A},\mathbf{B})$ be stabilizable and matrices $Q=Q^T$ and $R=R^T$ be positive definite. Let feedback gain K be chosen as

$$K = R^{-1}\mathbf{B}^T P_1, \tag{2,36}$$

where P_1 is the unique positive definite solution of the control algebraic Riccati equation (ARE) [96]

$$\mathbf{A}^T P_1 + P_1\mathbf{A} + Q - P_1\mathbf{B}R^{-1}\mathbf{B}^T P_1 = 0. \tag{2,37}$$

Then, all the matrices $\mathbf{A}$-$c\lambda_i\mathbf{B}K$, $\forall i \in \{1,2,\ldots,\mathrm{N}\}$ are Hurwitz if $c \geq \frac{1}{2\lambda_{\min}}$, where

$\lambda_{\min} = \min_{i\in\mathcal{N}} Re(\lambda_i)$ ($Re(\lambda_i)$ denotes the real part of λ_i).

Theorem 2.1 Let the digraph Gr have a spanning tree and $b_i \neq 0$ for one DG placed on a root node of the digraph Gr. It is assumed that the internal dynamics of each DG are asymptotically stable. Let the auxiliary control v_i in (2,27) be

$$v_i = -cK\mathbf{e}_i, \tag{2,38}$$

where $c \in R$ is the coupling gain, and $K \in R^{1\times 2}$ is the feedback control vector. Then, all $\mathbf{y}_i$ in (2,29) synchronize to $\mathbf{y}_0$ in (2,30) and, hence, the direct term of DG output voltages v_{odi} synchronizes to v_{ref}, if K is chosen as in (2,36) and

$$c \geq \frac{1}{2\lambda_{\min}}, \tag{2,39}$$

where $\lambda_{\min} = \min_{i\in\mathcal{N}} Re(\lambda_i)$.

Proof: Consider the Lyapunov function candidate

$$V = \frac{1}{2}\boldsymbol{\delta}^T P_2 \boldsymbol{\delta}, \quad P_2 = P_2^T, P_2 > 0, \tag{2,40}$$

where $\boldsymbol{\delta}$ is the global disagreement vector in (2,32). Then

$$\dot{V} = \boldsymbol{\delta}^T P_2 \dot{\boldsymbol{\delta}} = \boldsymbol{\delta}^T P_2 \left(\dot{\mathbf{Y}} - \dot{\mathbf{Y}}_0\right) = \boldsymbol{\delta}^T P_2 \left((I_N \otimes \mathbf{A})\boldsymbol{\delta} + (I_N \otimes \mathbf{B})\mathbf{v}\right). \tag{2,41}$$

The global auxiliary control $\mathbf{v}$ can be written as

$$\mathbf{v} = -c(I_N \otimes K)\left((L+B)\otimes I_2\right)\boldsymbol{\delta}. \tag{2,42}$$

Placing (2,42) into (2,41) yields

$$\dot{V} = \boldsymbol{\delta}^T P_2 \left(I_N \otimes \mathbf{A} - c(L+B)\otimes \mathbf{B}K\right)\boldsymbol{\delta} \equiv \boldsymbol{\delta}^T P_2 \mathbf{H}\boldsymbol{\delta}. \tag{2,43}$$

From Lemma 1.1 and Lemma 1.2, $\mathbf{H}$ is Hurwitz. Therefore, given any positive real number β, the positive definite matrix P_2 can be chosen such that the following Lyapunov equation holds,

$$P_2\mathbf{H} + \mathbf{H}^T P_2 = -\beta I_{2N}, \tag{2,44}$$

Placing (2,44) in (2,43) yields

$$\dot{V} = \boldsymbol{\delta}^T P_2 \mathbf{H}\boldsymbol{\delta} = \frac{1}{2}\boldsymbol{\delta}^T (P_2\mathbf{H} + \mathbf{H}^T P_2)\boldsymbol{\delta} = -\frac{\beta}{2}\boldsymbol{\delta}^T I_{2N}\boldsymbol{\delta}. \tag{2,45}$$

Equation (2,45) shows that $\dot{V} \le 0$. Therefore, the global disagreement vector $\boldsymbol{\delta}$, (2,26), and (2,38) are asymptotically stable and all $\mathbf{y}_i$ in (2,29) synchronize to $\mathbf{y}_0$ in (2,30). Hence the direct term of DG output voltages v_{odi} synchronizes to v_{ref}. If the internal dynamics are asymptotically stable, then they are all bounded. This completes the proof. □

The block diagram of secondary voltage control based on distributed cooperative control is shown in Figure 2-5. As seen, the control input E_i^* is implemented using (2,27). Each DG has a $\dot{v}_{odi}$ calculator block based on (2,15).

Choosing the coupling gain c and the feedback control vector Kbased on (2,36) and (2,39) ensures the asymptotic stability of the controller. Moreover, these controller parameters can adjust the response speed of the secondary voltage control. Appendix A will discuss the effects of ARE parameters on the synchronization speed of the proposed voltage control.

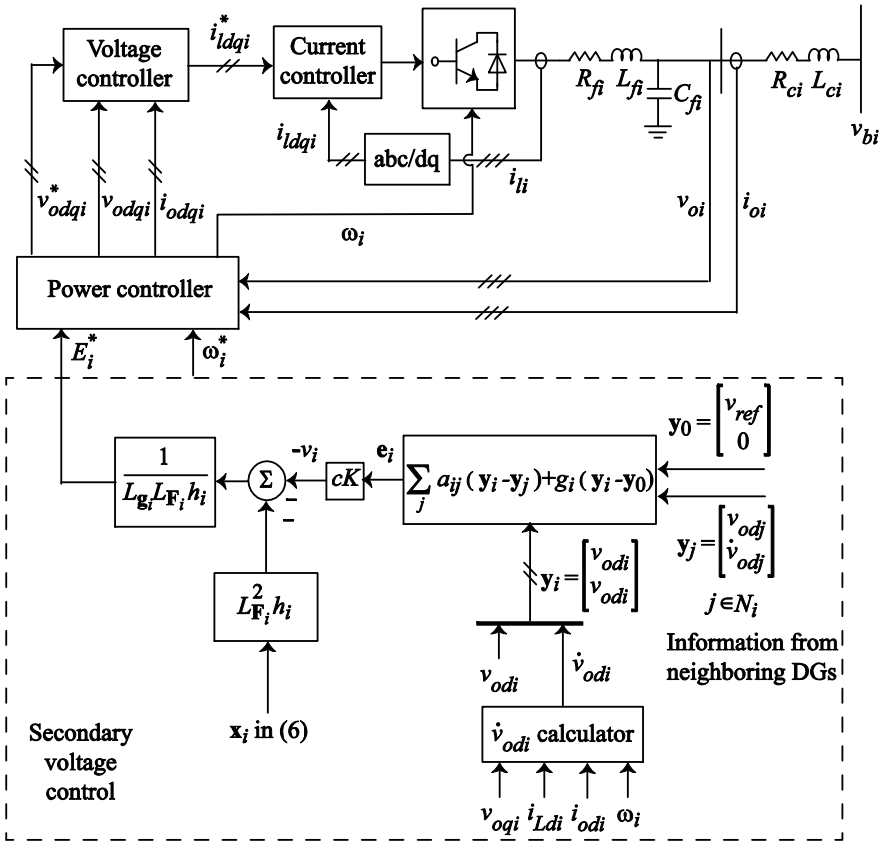

Figure 2-5 The Block Diagram of the Proposed Secondary Voltage Control

The Required Sparse Communication Topology for Secondary Control

The proposed secondary voltage control must be supported by a local communication network. The communication networks can be implemented by the TCP/IP communication protocol with optical fiber links [85]. For the microgrids with a small geographical span, the communication network can also be implemented by CAN Bus, PROFIBUS, and SERCOS communication protocols [13], [98]. The settling time of the secondary control can be up to one minute [13]. Therefore, the communication network operates much faster than the secondary control. The sampling time of the secondary control can be chosen much larger than the sampling time of the communication network. It should be noted that communication links contain an intrinsic delay. Since the time scale of the secondary control is large enough, the communication link delays can safely assumed zero [13]. The proposed secondary voltage control can admit both time invariant and time variant communication networks.

In the case of time invariant communication networks, the adjacency matrix A_G is fixed. According to the results of the Theorem 2.1, the communication topology should be a graph containing a spanning tree in which the secondary control of each DG only requires information about that DG and its immediate neighbors in the communication graph. Therefore, the communication requirements for implementing the proposed control with a time invariant communication network are rather mild. However, the implemented secondary control may not be robust against communication link failures or data loss. Given the physical structure of the microgrid, it is not difficult to select a graph with a spanning tree that connects all the DGs in an optimal fashion. Such optimal connecting graphs can be designed using operations research or assignment problem solutions [99]-[100]. The optimization criteria can include minimal lengths of the communication links, maximal use of existing communication links, minimal number of links, and etc.

Alternatively, time variant communication structure can be exploited to increase the

secondary control reliability. In this communication structure, each DG can send its own information to the neighboring DGs intermittently. The communication network is piecewise constant (i.e. the adjacency matrix A_G changes intermittently at pre-specified time instants.). Therefore, the secondary control is robust against data loss and communication link failures [77]. According to [77], a time variant communication network can provide the synchronization if the sequential completeness condition is satisfied. The sequential completeness condition means that, with the infinite sequence of finite intervals, the resulting graph over each finite interval must contain a spanning tree.

Simulation Results for the Distributed Secondary Voltage Control

The effectiveness of the proposed secondary voltage control is verified by simulating an islanded microgrid in Matlab. Figure 2-6 illustrates the single line diagram of the microgrid test system. This microgrid consists of four DGs. The lines between buses are modeled as series RL branches. The specifications of the DGs, lines, and loads are summarized in Appendix B.

It is assumed that DGs communicate with each other through the communication digraph depicted in Figure 2-7. This communication topology is chosen based on the geographical location of DGs. The associated adjacency matrix of the digraph in Figure 2-7 is

$$A_G = \begin{bmatrix} 0 & 0 & 0 & 0 \\ 1 & 0 & 0 & 0 \\ 0 & 1 & 0 & 0 \\ 1 & 0 & 0 & 0 \end{bmatrix}. \quad (2,46)$$

DG 1 is the only DG that is connected to the leader node with the pinning gain b_1=1. In the following, first, the effectiveness of the proposed secondary voltage control is shown for three different reference voltage values. Then, the effects of the algebraic Riccati equation parameters on the transient response of the controller are studied. Finally, the effectiveness of the proposed voltage control is verified when a time-varying communication network is used.

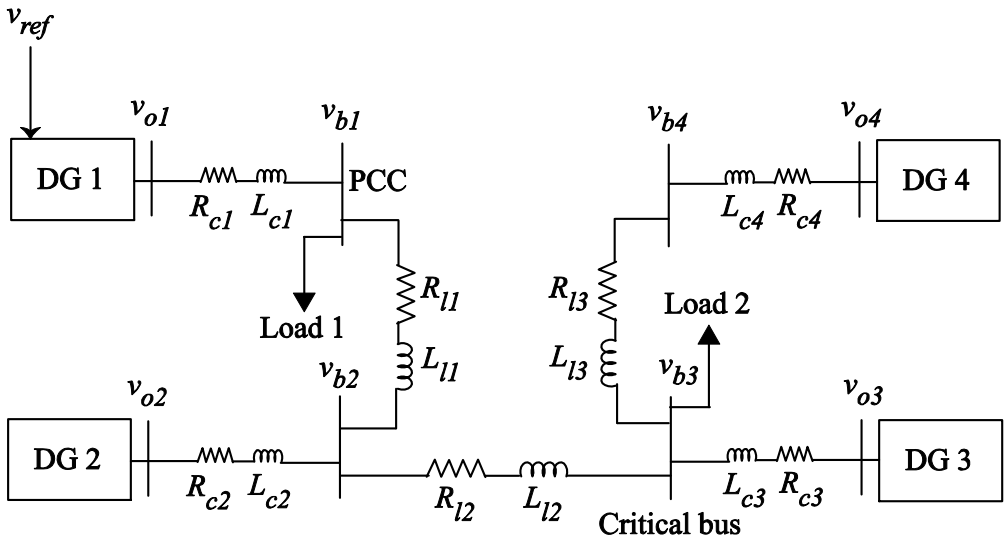

Figure 2-6 Single Line Diagram of the Microgrid Test System

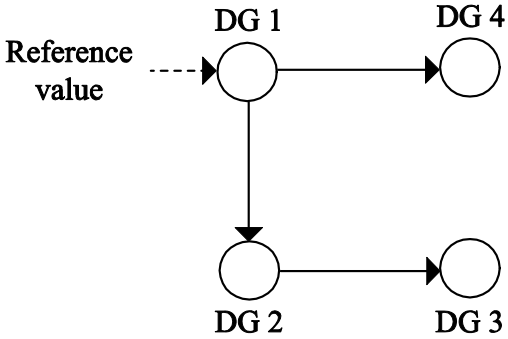

Figure 2-7 Topology of the Communication Digraph

Simulation Results for Different Reference Voltage Values

In this section, the coupling gain in (2,38) is c=4 which satisfies (2,39). The solution of the algebraic Riccati equation in (2,37) is used to calculate the feedback control vector K in (2,38). The algebraic Riccati equation parameters are chosen as $Q=\begin{bmatrix} 50000 & 0 \\ 0 & 1 \end{bmatrix}$ and R=0.01. The resulting feedback control vector is K=[2236 67.6]. It is assumed that the microgrid is islanded from the main grid at t=0, and the secondary control is applied at t=0.6 s. It should be

noted that the secondary control level always exists as a supervisory control level and take actions in the event of disturbances. However, to highlight the effectiveness of the proposed secondary control, it is assumed that the secondary control is applied with a delay. Figures 2-8(a), 2-8(b), and 2-8(c) show the simulation results when the reference voltage value is set to 1 pu, 0.95 pu, and 1.05 pu, respectively. As seen in Figure 2-8, while the primary control keeps the voltage amplitudes stable, the secondary control returns all terminal voltage amplitudes to the pre-specified reference values in 0.2 seconds.

The secondary voltage control can also be defined to control the voltage magnitude of the critical bus shown in Figure 2-6. In this case, v_{ref} is chosen according to (2,21), where $v_{c,mag}$ in (2,21) denotes the voltage magnitude of the critical bus. $v_{nominal}$ in (2,21) is set to 1 pu. k_{pc} and k_{ic} in (2,21) are set to 4 and 100, respectively. As seen in Figure 2-9, the secondary control is applied at t=0.6 s, and returns the voltage magnitude of critical bus to $v_{nominal}$ in less than 0.3 s.

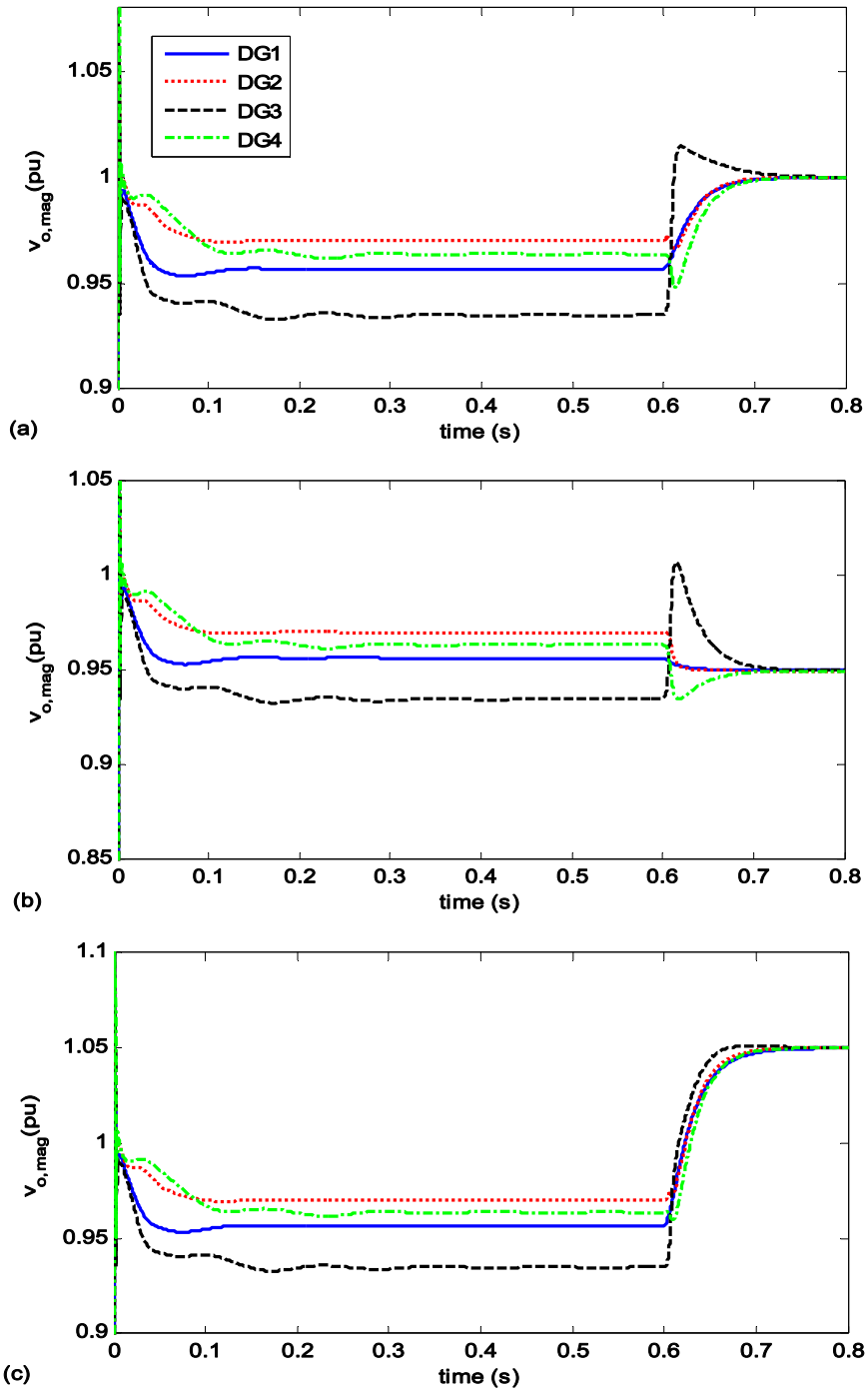

Figure 2-8 DG Output Voltage Magnitudes for (a) v_{ref}=1 pu, (b) v_{ref}=0.95 pu, and (c) v_{ref}=1.05 pu

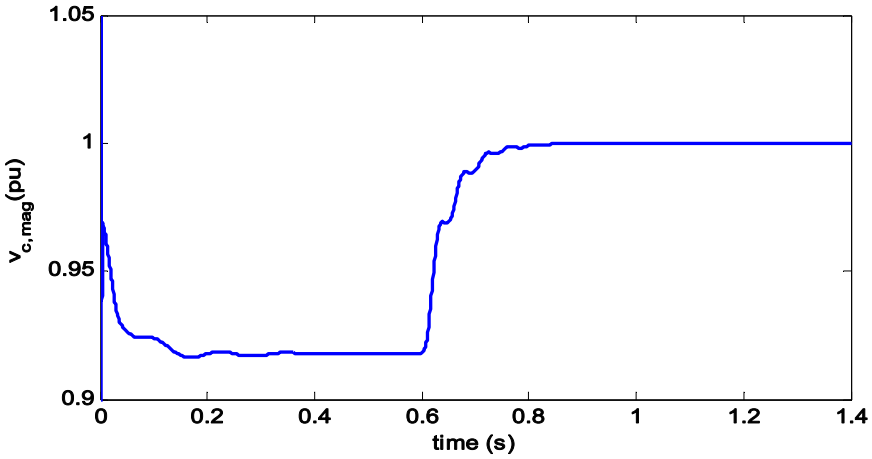

Figure 2-9 Critical Bus Voltage Magnitude

The Effect of Algebraic Riccati Equation (ARE) Parameters on the Transient Response

To show the effect of the ARE parameters on the response speed of the secondary voltage control (Appendix A), two different cases are considered. The reference value for the terminal voltage of DGs is set to 1 pu. In the first case, ARE parameters are set as $Q = \begin{bmatrix} 1000 & 0 \\ 0 & 1 \end{bmatrix}$ and $R = 0.01$. Compared with the case studied in Figure 2-8(a), the element in the first row and column of matrix Q, which directly affects the control of v_{odi}, is smaller. Figure 2-10(a) shows the DG output voltage magnitudes before and after applying the secondary control. As seen, the terminal voltage amplitudes synchronize to 1 pu after 0.3 s. Therefore, with a smaller Q, the secondary voltage control is slower than the case studied in Figure 2-8(a).

In the second case, the ARE parameters are set as $Q = \begin{bmatrix} 50000 & 0 \\ 0 & 1 \end{bmatrix}$ and $R = 5$. Compared with the case studied in Figure 2-8(a), R is larger. Figure 2-10(b) shows the DG output voltage magnitudes before and after applying the secondary control. As seen, the terminal voltage amplitudes converge to 1 pu after 0.5 s. Therefore, with a larger R, the secondary voltage control is slower than the case studied in Figure 2-8(a).

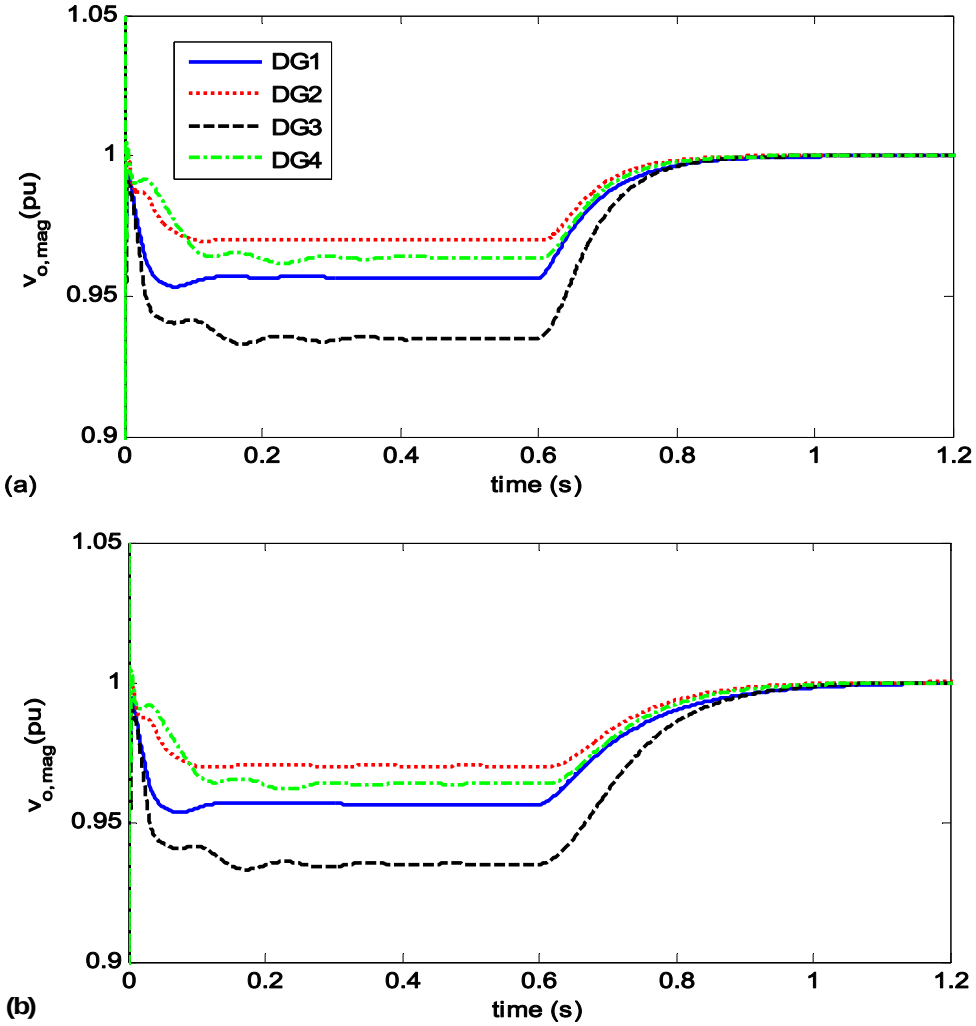

Figure 2-10 DG Output Voltage Magnitudes with the Following Control Parameters: (a) $Q = \begin{bmatrix} 1000 & 0 \\ 0 & 1 \end{bmatrix}$ and R=0.01, (b) $Q = \begin{bmatrix} 50000 & 0 \\ 0 & 1 \end{bmatrix}$ and R=5.

The Effect of Time-varying Communication Networks on the Performance of the Distributed Secondary Voltage Control

In this section, it is assumed that the microgrid is islanded from the main grid at t=0, and the voltage control is applied at t=0.6 s. However, the distributed voltage control is associated with time-varying communication networks. The reference voltage is set to v_{ref}=1 pu. Figure 2-11 shows the three communication network structures that are used in simulation. Each structure is adopted at a specific time interval. The communication digraph in Figure 2-11(a) models the communication network at the time interval [(0.6+0.15k) s, (0.6+0.15k)+0.05 s], for k=0,1,... The communication digraph in Figure 2-11(b) models the communication network at the time interval [(0.65+0.15k) s, (0.65+0.15k)+0.05 s], for k=0,1,... The communication digraph in Figure 2-11(c) models the communication network at the time interval [(0.7+0.15k) s, (0.7+0.15k)+0.05 s], for k=0,1,... It is seen that over the each 0.15 s period, the sequential completeness condition is satisfied. As seen in Figure 2-12, while the primary control keeps the voltage amplitudes stable, the secondary control returns all terminal voltage amplitudes to v_{ref}. This simulation result verifies the effectiveness of the proposed voltage control in the case of time-varying communication networks and communication link failures.

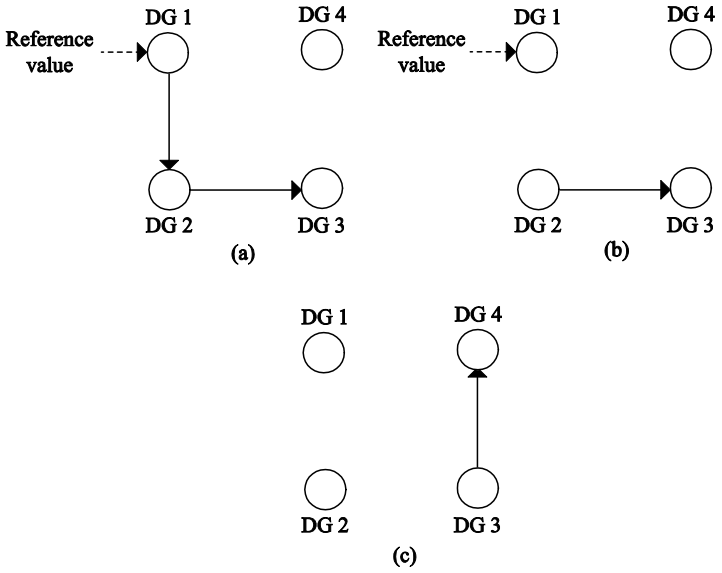

Figure 2-11 Topologies of the Time-Varying Communication Network

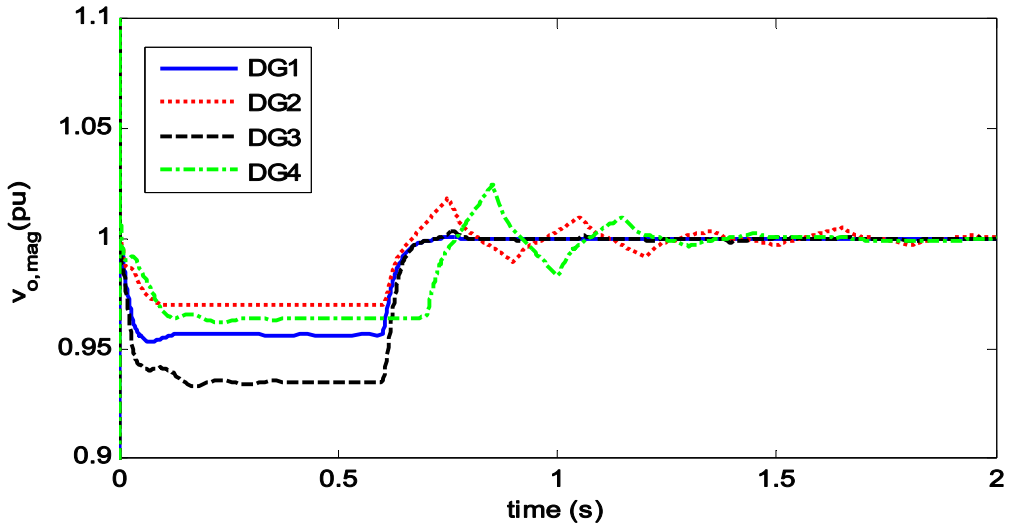

Figure 2-12 DG Output Voltage Magnitudes with Time-Varying Communication Network

Conclusion

In this chapter, the concept of distributed cooperative control of multi-agent systems is adopted to implement the secondary voltage control of microgrids. Input-output feedback linearization is used to transform the nonlinear dynamics of DGs to linear dynamics. Feedback linearization converts the secondary voltage control to a second-order tracking synchronization problem. The controller for each DG is fully distributed. Each DG only requires its own information and the information of some neighbors. The proposed microgrid secondary control requires a sparse communication network with one-way communication links and is more reliable than centralized secondary controls. It is shown that the proposed voltage control effectively works in the case of time-varying communication networks, and the controller parameters can effectively tune the controller synchronization speed.

Chapter 3

Distributed Secondary Frequency Control of Microgrids

Introduction

In this chapter, the distributed cooperative control of multi-agent systems is used to design the secondary frequency control of microgrids. Input-output feedback linearization can be used to transform the nonlinear heterogeneous dynamics of DGs to linear dynamics. Once input-output feedback linearization is applied, the secondary frequency control leads to a first-order synchronization problem. Fully distributed frequency control protocols are derived for each DG that synchronize the DG frequencies to the nominal value and allocate the active power of DGs based on their active power ratings [101]. The proposed secondary frequency control is implemented through a sparse communication network. The communication network is modeled by a digraph. Each DG requires its own information and the information of its neighbors on the digraph. The sparse communication structure requires one-way communication links and is more reliable than centralized secondary frequency controls.

The rest of this chapter is organized as follows. First, the secondary frequency control objectives are discussed. Then, the secondary frequency control is proposed. Finally, a microgrid test system is used to verify the effectiveness of the proposed secondary frequency control.

Secondary Frequency Control Objectives

The primary frequency control is considered,

$$\omega_i = \omega_i^* - D_{Pi} P_i. \tag{3,1}$$

where ω_i^* is the primary frequency control reference and D_{Pi} is the frequency-active power droop coefficient. The secondary frequency control chooses ω_i^* such that the angular frequency of each DG synchronizes to nominal angular frequency, i.e. $\omega_i \to \omega_{ref}$, where

$\omega_{ref} = 2\pi f_{ref}$. f_{ref} is the nominal frequency of the microgrid, and can be equal to 50 Hz or 60 Hz. It should be noted that once the secondary frequency control is applied, the DG output powers are allocated according to the same pattern used for primary control [102]. After applying the primary control, the DG output powers satisfy the following equality

$$D_{P1}P_1 = \cdots = D_{PN}P_N. \tag{3,2}$$

Since the active power droop coefficients D_{Pi} are chosen based on the active power rating of DGs, P_{maxi}, (3,2) is equivalent to

$$\frac{P_1}{P_{\max 1}} = \cdots = \frac{P_N}{P_{\max N}}. \tag{3,3}$$

Therefore, the secondary frequency control must also satisfy (3,2) or (3,3). For the secondary frequency control, the outputs and inputs of the dynamical model of DG in (2,19) are $y_i = \omega_i$ and $u_i = \omega_i^*$, respectively.

In the next section, the distributed cooperative control of multi-agent systems will be adopted to develop the secondary frequency control with a distributed structure. The proposed secondary frequency control exploits the following relationship between the output active power of each DG and its angular frequency. Assuming small R_{ci} in Figure 2-1, the output active power of each DG can be written as [103]

$$P_i = \frac{|v_{oi}||v_{bi}|}{X_{ci}}\sin(\delta_i) \equiv h_i \sin(\delta_i), \tag{3,4}$$

where δ_i is the angle of the DG reference frame with respect to the common reference frame. v_{oi} , v_{bi} , and $X_{ci} = \omega_i L_{ci}$ are shown in Figure 2-1. The term h_i can be assumed to be constant since the amplitude of v_{oi} and v_{bi} change slightly around the nominal voltage [103]. Since X_{ci} is typically small, δ_i is small, and hence, $\sin(\delta_i)$ is approximately equal to δ_i [103]. Considering these assumptions and differentiating (3,4) yields

$$\dot{P}_i = h_i(\omega_i - \omega_{com}), \tag{3,5}$$

Equation (3,5) provides a direct relationship between the differentiated output power of DGs and their angular frequency with respect to the angular frequency of microgrid. The global form of (3,5) can be written as

$$\dot{P} = h(\omega - \underline{\omega}_{com}), \tag{3,6}$$

where $h = diag\{h_i\}$ and $\underline{\omega}_{com} = \mathbf{1}_N \otimes \omega_{com}$.

Secondary Frequency Control Based on Distributed Cooperative Control

The distributed cooperative frequency control is designed to synchronize the frequency of DGs, ω_i in (3,1), to the reference frequency, ω_{ref}, while sharing the active power among DGs based on their power ratings as stated in (3,2).

Applying input-output feedback linearization by differentiating the frequency-droop characteristic in (3,1) yields

$$\dot{\omega}_i^* = \dot{\omega}_i + D_{Pi}\dot{P}_i = u_i, \tag{3,7}$$

where u_i is an auxiliary control to be designed. Equation (3,7) is a dynamic system for computing the control input ω_i^* from u_i (See Figure 3-1). The auxiliary control should be designed such that DG frequencies synchronize to the reference frequency ω_{ref}, and (3,2) is satisfied. According to (3,7), the secondary frequency control of a microgrid including N DGs is transformed to a synchronization problem for a first-order and linear multi-agent system

$$\begin{cases} \dot{\omega}_1 + D_{P1}\dot{P}_1 = u_1, \\ \dot{\omega}_2 + D_{P2}\dot{P}_2 = u_2, \\ \vdots \\ \dot{\omega}_N + D_{PN}\dot{P}_N = u_N. \end{cases} \tag{3,8}$$

To achieve synchronization, it is assumed that DGs can communicate with each other through the prescribed communication digraph Gr in Chapter 2. The auxiliary controls u_i are

chosen based on each DG's own information, and the information of its neighbors in the communication digraph as

$$u_i = -c_f(\sum_{j\in N_i} a_{ij}(\omega_i - \omega_j) + b_i(\omega_i - \omega_{ref}) + \sum_{j\in N_i} a_{ij}(D_{Pi}P_i - D_{Pj}P_j)), \quad (3,9)$$

where $c_f \in R$ is the coupling gain. It is assumed that the pinning gain $b_i \geq 0$ is nonzero for only one DG that has the reference frequency ω_{ref}.

The global control input u is written as

$$u = -c_f((L+B)(\omega - \underline{\omega}_{ref}) + LD_P P), \quad (3,10)$$

where $\omega = [\omega_1 \quad \omega_2 \quad \cdots \quad \omega_N]^T$, $\underline{\omega}_{ref} = \mathbf{1}_N \otimes \omega_{ref}$, with $\mathbf{1}_N$ the vector of ones with the length of N, $D_P = diag\{D_{Pi}\}$, and $P = [P_1 \quad P_2 \quad \cdots \quad P_N]^T$. The Kronecker product is $\otimes$. $B \in \mathbb{R}^{N\times N}$ is a diagonal matrix with diagonal entries equal to the pinning gains b_i. The global form of dynamics in (3,8) can be written as

$$\dot{\omega} + D_P\dot{P} = -c_f((L+B)(\omega - \underline{\omega}_{ref}) + LD_P P). \quad (3,11)$$

The term $(L+B)(\omega - \underline{\omega}_{ref})$ is defined as the global neighborhood tracking error e. The term $\omega - \underline{\omega}_{ref}$ is defined as the global disagreement vector, δ.

Lemma 2.1 [83]. Zero is a simple eigenvalue of L if and only if the directed graph has a spanning tree. Moreover, $L\mathbf{1}_N = 0$, with $\mathbf{1}_N$ being the vector of ones with the length of N.

Lemma 2.2 [104]. Let the digraph Gr have a spanning tree and $b_i \neq 0$ for at least one root node. Then, $L+B$ is a nonsingular M-matrix. Additionally

$$\|\delta\| \leq \|e\| / \sigma_{\min}(L+B), \quad (3,12)$$

where $\sigma_{\min}(L+B)$ is the minimum singular value of $L+B$, and $e = 0$ if and only if $\delta = 0$.

In the following, it is assumed that the DG for which $b_i \neq 0$ is labeled as DG 1. Theorem 3.1 is the main result.

Theorem 3.1 Let the digraph Gr have a spanning tree and $b_i \neq 0$ for only one DG placed as a root node of digraph Gr. Let the auxiliary control u_i be chosen as in (3,9). Then, the DG frequencies ω_i in (3,1) synchronize to ω_{ref}, and the active power among DGs is shared based on their power ratings satisfying (3,3).

Proof: In the steady state, the left sides of (3,11) and (3,6) are equal to zero. Setting the left side of (3,6) equal to zero yields

$$\omega = \underline{\omega}_{com}. \tag{3,13}$$

Equation (3,13) shows that all the DG frequencies synchronize to the microgrid frequency in steady state. Therefore, according to Lemma 2.1

$$L\omega = 0. \tag{3,14}$$

Setting the left side of (3,11) equal to zero, and considering (3,14) yields

$$LD_P P + B(\omega - \underline{\omega}_{ref}) = 0. \tag{3,15}$$

The commensurate form of (3,15) can be written as

$$\begin{bmatrix} \sum_{j=1:N} a_{1j} & -a_{12} & \cdots & -a_{1N} \\ -a_{21} & \sum_{j=1:N} a_{2j} & \cdots & -a_{2N} \\ \vdots & \vdots & \ddots & \vdots \\ -a_{N1} & -a_{N2} & \cdots & \sum_{j=1:N} a_{Nj} \end{bmatrix} \begin{bmatrix} D_{P1}P_1 \\ D_{P2}P_2 \\ \vdots \\ D_{PN}P_N \end{bmatrix} + \begin{bmatrix} b_1(\omega_1 - \omega_{ref}) \\ 0 \\ \vdots \\ 0 \end{bmatrix} = 0, \tag{3,16}$$

that equivalently yields (3,17) and (3,18).

$$a_{12}(D_{P1}P_1 - D_{P2}P_2) + \cdots + a_{1N}(D_{P1}P_1 - D_{PN}P_N) + b_1(\omega_1 - \omega_{ref}) = 0, \tag{3,17}$$

$$(\bar{L} + \bar{B})\left(\begin{bmatrix} D_{P2}P_2 \\ D_{P3}P_3 \\ \vdots \\ D_{PN}P_N \end{bmatrix} - \begin{bmatrix} D_{P1}P_1 \\ D_{P1}P_1 \\ \vdots \\ D_{P1}P_1 \end{bmatrix} \right) = 0, \tag{3,18}$$

where

$$\bar{L}=\begin{bmatrix} \sum_{j=1:N} a_{2j} & -a_{23} & \cdots & -a_{2N} \\ -a_{32} & \sum_{j=1:N} a_{3j} & \cdots & -a_{3N} \\ \vdots & \vdots & \ddots & \vdots \\ -a_{N2} & -a_{N3} & \cdots & \sum_{j=1:N} a_{Nj} \end{bmatrix}, \tag{3,19}$$

$$\bar{B}=\begin{bmatrix} -a_{21} & 0 & \cdots & 0 \\ 0 & -a_{31} & \cdots & 0 \\ \vdots & \vdots & \ddots & \vdots \\ 0 & 0 & \cdots & -a_{N1} \end{bmatrix}. \tag{3,20}$$

Equation (3,18) shows that the set $\{D_{P1}P_1, D_{P2}P_2, ..., D_{PN}P_N\}$ can be considered on a communication digraph with $D_{P1}P_1$ as the leader node. All nodes have access to the leader $D_{P1}P_1$ through the matrix $\bar{B}$ in (3,20). Since the original digraph Gr has a spanning tree with $D_{P1}P_1$ as the root node, at least one of the diagonal terms in $\bar{B}$ is non-zero. Therefore, exploiting Lemma 2.2 shows that all $D_{Pi}P_i$ synchronize to a common value in the steady state which satisfies (3,2) , or, equivalently, (3,3). Additionally, according to (3,17), having all $D_{Pi}P_i$ synchronized to a common value shows that ω_1 synchronizes to ω_{ref} and hence, according to (3,13), all DG frequencies synchronize to ω_{ref} . This completes the proof. □

The block diagram of the secondary frequency control based on the distributed cooperative control is shown in Figure 3-1. As seen in this figure, the control input ω_i^* is written as

$$\omega_i^* = \int u_i dt. \tag{3,21}$$

The coupling gain c_f has a direct impact on the convergence speed of the proposed frequency control. Appendix C discusses the impact of the controller gain on the synchronization speed a tracking synchronization problem the controller.

The proposed secondary frequency control can admit both time invariant and time

variant communication networks. In the case of time invariant communication networks, according to the results of the Theorem 3.1, the communication topology should be a graph containing a spanning tree in which the secondary control of each DG only requires information about that DG and its immediate neighbors in the communication graph. Therefore, the communication requirements for implementing the proposed control with a time invariant communication network are rather mild.

In the case of time variant communication structure, the communication network is piecewise constant (i.e. the adjacency matrix A_G changes intermittently at pre-specified time instants.). Therefore, the secondary frequency control is robust against data loss and communication link failures [77]. According to [77], a time variant communication network can provide the synchronization if the sequential completeness condition is satisfied. The sequential completeness condition means that, with the infinite sequence of finite intervals, the resulting graph over each finite interval must contain a spanning tree.

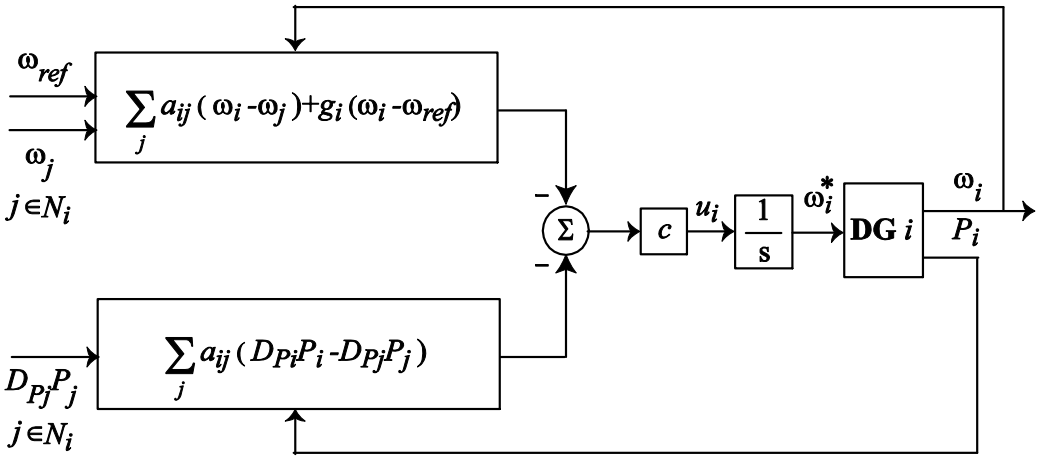

Figure 3-1 The Block Diagram of the Distributed Secondary Frequency Control

Simulation Results for the Distributed Secondary Frequency Control

The microgrid shown in Figure 2-6 is used to verify the effectiveness of the proposed secondary control. The specifications of the DGs, lines, and loads are summarized in Appendix B. The simulation results are extracted by modeling the dynamical equations of microgrid in Matlab.

It is assumed that DGs communicate with each other through the communication digraph depicted in Figure 2-7. This communication topology is chosen based on the geographical location of DGs. DG 1 is the only DG connected to the leader node with the pinning gain of $b_1 = 1$. The reference value for the microgrid frequency $f_{ref} = \omega_{ref} / 2\pi$ is set as 50 Hz. The coupling gain c_f is set to 400.

It is assumed that the microgrid is islanded form the main grid at t=0 and the secondary frequency control is applied at t=0.6 s. Figure 3-2 shows frequencies and output powers of DGs before and after applying the secondary frequency control. As seen in Figure 3-2(a), once the primary control is applied, DG operating frequencies all go to a common value that is the operating frequency of microgrid. However, the secondary frequency control returns the operating frequency of microgrid to its nominal value after 0.3 s. Figure 3-2(b) shows that the DG output powers all satisfy (3,2) and (3,3), and are set according to the power rating of DGs.

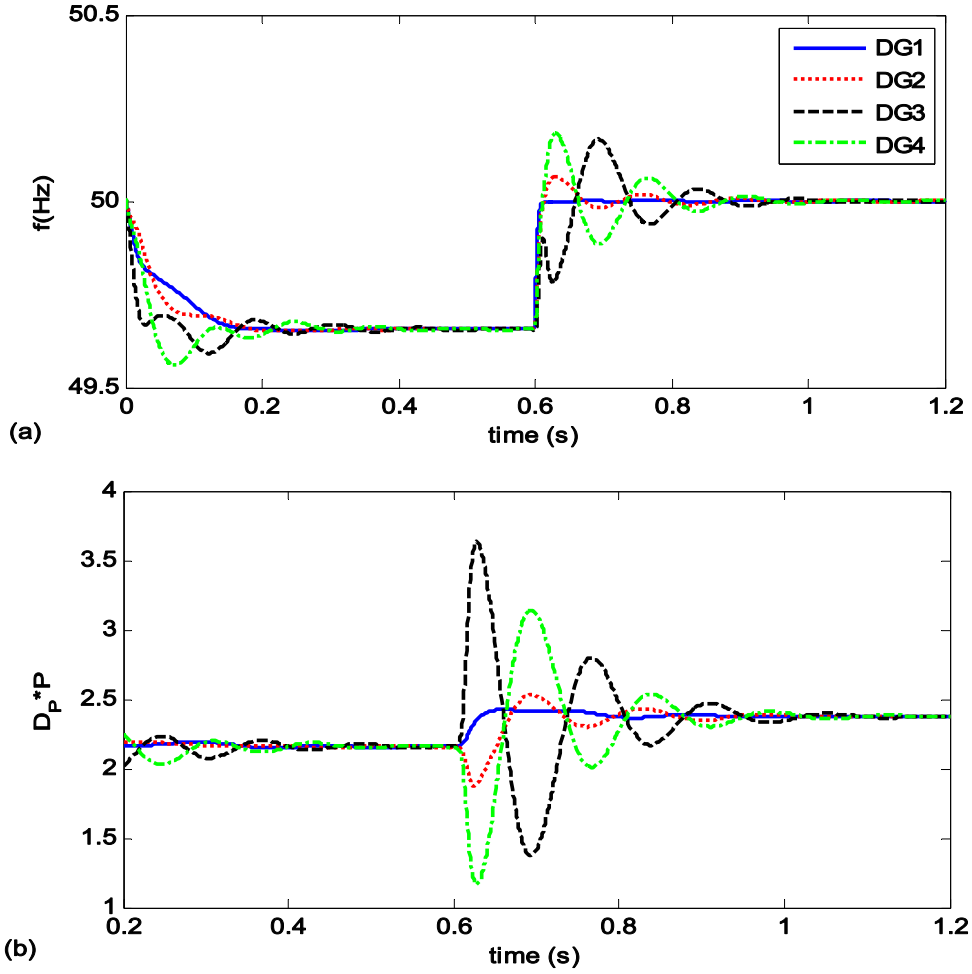

Figure 3-2 The Secondary Frequency Control with c_f= 400 and f_{ref}= 50 Hz: (a) DG Frequencies and (b) DG Active Power Ratios

The coupling gain c_f has a direct impact on the synchronization speed of the secondary frequency control. To show this impact, the coupling gain is decreased from 400 to 40 in the following case study. Figure 3-3 shows the simulation results when the coupling gain c_f is set to 40. It is assumed that the microgrid is islanded from the main gird at *t*=0, and the secondary frequency control is applied at *t*=0.6 s. Compared with the simulation results in Figure 3-2, smaller value of the coupling gain c_f decreases the frequency control synchronization speed.

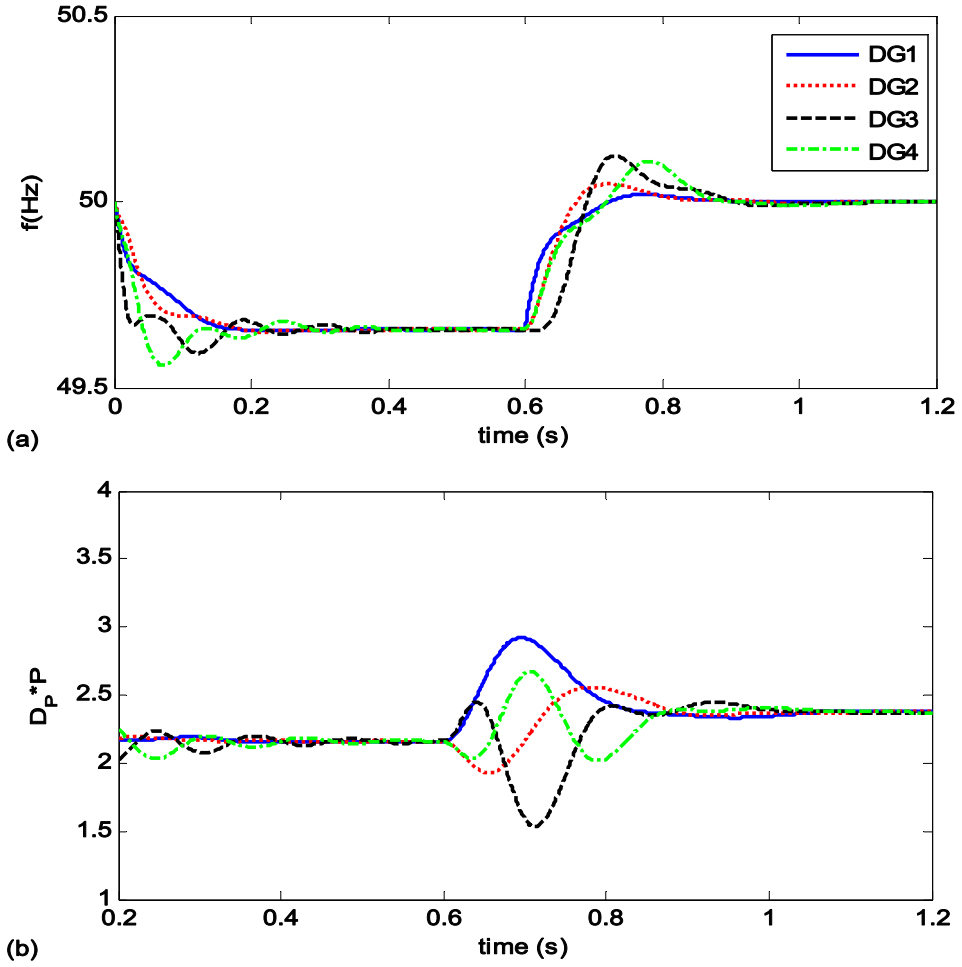

Figure 3-3 The Secondary Frequency Control with c_f= 40 and f_{ref}= 50 Hz: (a) DG Frequencies and (b) DG Active Power Ratios

To show the effectiveness of the proposed distributed frequency control, another round of simulations are performed using a time-varying communication network, shown in Figure 2-11. The communication digraph in Figure 2-11(a) models the communication network at the time interval [(0.6+0.15k) s, (0.6+0.15k)+0.05 s], for k=0,1,... The communication digraph in Figure 2-11(b) models the communication network at the time interval [(0.65+0.15k) s, (0.65+0.15k)+0.05 s], for k=0,1,... The communication digraph in Figure 2-11(c) models the communication network at the time interval [(0.7+0.15k) s, (0.7+0.15k)+0.05 s], for k=0,1,... It is seen that over the each 0.15 s period, the sequential completeness condition is satisfied. As seen in Figure 3-4(a), once the primary control is applied, DG operating frequencies all go to a common value that is the operating frequency of microgrid. However, the secondary frequency control returns the operating frequency of microgrid to its nominal value. Figure 3-4(b) shows that the DG output powers all satisfy (3,2) and (3,3), and are set according to the power rating of DGs. These results verify the effectiveness of the proposed secondary frequency control when a time-varying communication network is used.

Conclusion

The secondary frequency control of microgrids is designed based on the distributed cooperative control of multi-agent systems. Input-output feedback linearization is used to transform the nonlinear dynamics of DG to linear dynamics. Feedback linearization converts the secondary frequency control to the first-order tracking synchronization problem. The control inputs are designed to restore the frequency of microgrid and allocate the active power of DGs based on their active power ratings. The proposed secondary frequency control requires a sparse communication structure with one-way communication links and is more reliable than centralized secondary controls.

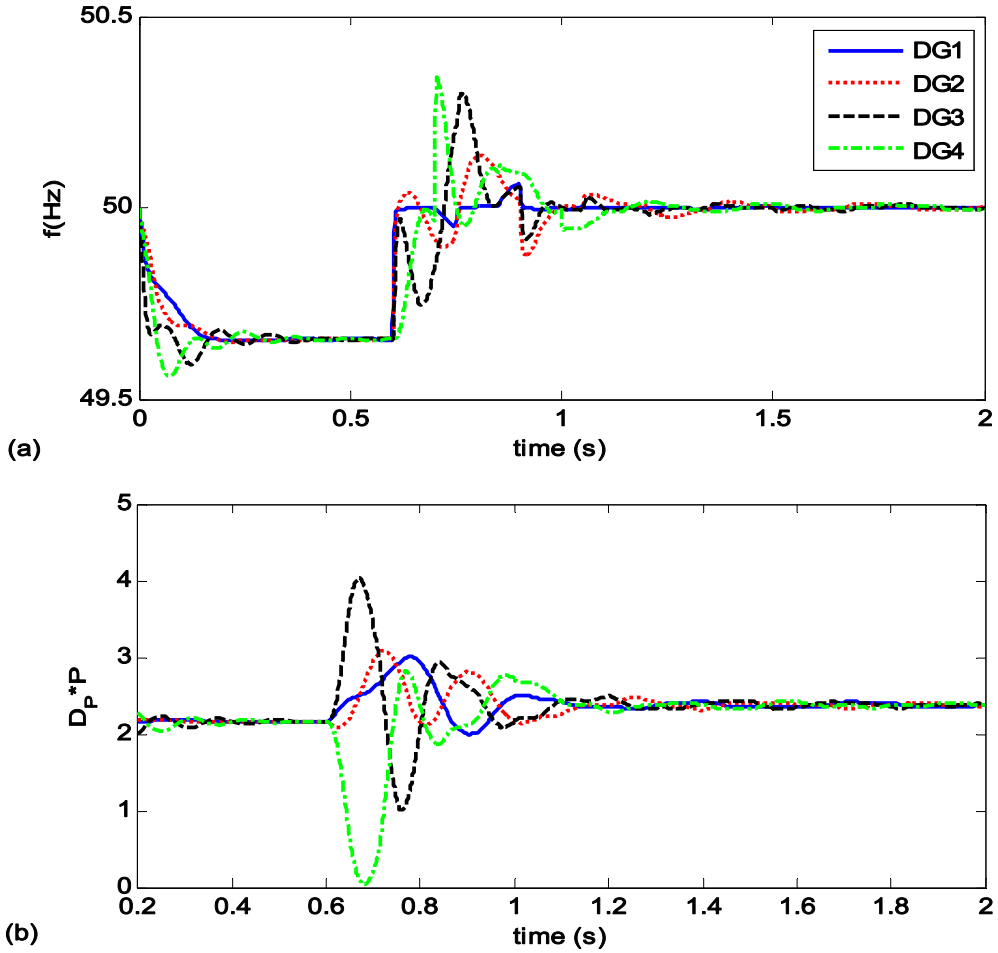

Figure 3-4 The Secondary Frequency Control with Time-Varying Communication Network: (a) DG Frequencies and (b) DG Active Power Ratios

Chapter 4

Two-Layer Multi-Objective Control Framework for Microgrids

Introduction

A microgrid as a small-scale power system facilitates the reliable and effective integration of DGs. Although DGs can be of rotating machinery type, more recently, electronically-interfaced DGs through voltage source inverters (VSI) became prevalent to integrate micro-turbines and renewable energy resources such as fuel-cells, solar energy, and wind energy. As discussed in Chapter 1, the control structure of a VSI may vary based on the control objectives such as voltage and frequency, or active and reactive power. In Chapters 2 and 3, distributed control structures for islanded microgrids with voltage controlled voltage source inverters (VCVSI) were proposed. VCVSIs have internal voltage and current controller loops that facilitate the voltage and frequency control of DG. However, in some DGs, the sole active and reactive power control may be of interest. This requirement can be satisfied through the current controlled voltage source inverters (CCVSI). CCVSIs possess an internal current controller that controls the direct and quadrature components of the VSI output current which in turn facilitates the active and reactive power control of DG [105]-[110]. Micro-turbines and fuel-cells are dispatchable power sources, and their associated voltage source inverter can operate as a CCVSI to adjust their generated power by the microgrid operator. Solar panels and wind turbine generators are intermittent power sources. The uncertainty and intermittency in the generated power is a big hassle to exploit wind and solar power sources as dispatchable DGs. Energy storage systems (e.g., batteries) can be exploited to compensate for the intermittency in the generated power of wind and solar power sources. Doing so, solar panels and wind turbine generators can also be exploited as dispatchable power sources [106].

A microgrid is able to operate in both grid-connected and islanded modes. In the grid-connected mode, the main grid dictates the microgrid voltage and frequency. In this mode, the DG control objectives are defined as active and reactive power, and hence they can be

exploited as CCVSIs. The microgrid can switch to the islanded mode due to the preplanned scheduling or unplanned disturbances. Subsequent to the islanding process, microgrid loses the voltage and frequency support by the main gird as well as the active and reactive power balance between the total power generation and consumption. Therefore, some DGs are required to switch to the VCVSI structure to provide a fast voltage and frequency support and compensate for the mismatch between the power generation and consumption. In this chapter, it is assumed that some DGs remain in the CCVSI mode subsequent to islanding process.

As discussed in Chapter 1, the VCVSI are equipped with the primary control to maintain the voltage and frequency stability of the microgrid. The primary control provides a fast voltage and frequency support, however, it might not return the microgrid to the normal operating conditions and an additional control level is required to restore the voltage and frequency. This functionality is provided by the secondary control, which compensates for the voltage and frequency deviations caused by the primary control [76]. In the previous chapters, the studied mcirogirds were assumed to be equipped with only VCVSIs. Therefore, the secondary control only dealt with the voltage and frequency control of VCVSIs. In this chapter, it is assumed that some DGs are exploited in the CCVSI mode. Therefore, the secondary control is designed to adjust the control inputs of VCVSIs and CCVSIs.

In this chapter, a two-layer control framework is proposed to implement the secondary control for an islanded microgrid containing both VCVSIs and CCVSIs. The first control layer deals with the voltage and frequency control of VCVSIs. Additionally, the active and reactive power of VCVSIs should be allocated based on their active and reactive power ratings. The second control layer objectives are to control the active and reactive power of CCVSIs. Each control layer is implemented through the distributed control of multi-agent systems. The control layers require a rather mild communication network with one-way communication links, and are fully distributed such that each DG only requires its own information and the information of its neighbors on the communication network graph. The distributed structure of the communication

network obviates the requirements for a central controller and improves the system reliability.

The salient features of the proposed methodology are:

- A two-layer and distributed control framework is proposed that simultaneously controls the VCVSI and CCVSI control objectives.
- The proposed control framework controls microgrids containing both VCVSIs and CCVSIs, synchronizes the voltage and frequency of the microgrid to the nominal values, and allocates the active and reactive power of VCVSIs and CCVSIs based on the inverter's power ratings.
- The availability of the active and reactive power capacity in VCVSIs is of particular importance to provide fast voltage/frequency support. The proposed control framework exploits a portion of CCVSIs' active and reactive power capacity for the voltage/frequency restoration and, hence, the availability of the VCVSIs' active and reactive power for future disturbances is increased.

This chapter is organized as follows. First, the two-layer and multi-objective control framework of microgrids is introduced. Then, a dynamical model for CCVSIs is proposed. Based on the dynamical models of VCVSIs and CCVSIs, distributed control protocols for VCVSIs and CCVSIs are designed. Finally, the proposed control framework is verified using a microgrid test system and IEEE 34 bus test feeder.

Two-Layer Multi-Objective Control Framework for Microgrids

Inverter based DGs can be of VCVSI or CCVSI type. In VCVSIs, internal voltage and current controller loops control the voltage and frequency of DG. CCVSIs possess an internal current controller that controls the direct and quadrature components of the VSI output current which in turn facilitates the active and reactive power control of DG. When a microgrid is connected to the main grid, its voltage and frequency are dictated by the main grid. In this mode, the DG control objectives are active and reactive power, and hence, all DGs can be exploited as CCVSIs. Subsequent to the islanding process, the microgrid loses its voltage and

frequency support by the main gird as well as the active and reactive balance between the total power generation and consumption. Therefore, some DGs are required to switch to the VCVSI structure to provide the voltage and frequency support and compensate for the mismatch between the power generation and consumption [76].

The VCVSIs are equipped with the primary control [76] to maintain the voltage and frequency stability of the microgrid. As discussed in Chapter 1, primary control avoids voltage and frequency instability by keeping these values in pre-specified ranges. Coordinated control of the primary local controllers can be achieved by the active and reactive-power droop techniques as

$$\begin{cases} \omega_i = \omega_i^* - D_{Pi} P_i, \\ v_{o,magi}^* = E_i^* - D_{Qi} Q_i. \end{cases} \tag{3,22}$$

$v^*_{o,magi}$ is the reference value for the output voltage magnitude that is provided for the internal voltage control loop of VCVSI. ω_i is the angular frequency of the VCVSI dictated by the primary control. P_i and Q_i are the measured active and reactive power at the DG's terminal. D_{Pi} and D_{Qi} are the droop coefficients. E_i^* and ω_i^* are the primary control references [76]. The droop coefficients are selected based on the active and reactive power ratings of each VCVSI.

The primary control provides a fast voltage and frequency support for the microgrid, however, it might not return the microgrid to the normal operating conditions and an additional control is required to restore the voltage and frequency. This functionality is provided by the secondary control, which compensates for the voltage and frequency deviations caused by the primary control. The secondary control operates with a longer time frame than primary control and adjusts the control inputs of VCVSIs and CCVSIs to restore the voltage and frequency of microgrid to their nominal values.

In this chapter, a two-layer control framework is presented to implement the secondary control for an islanded microgrid with both VCVSIs and CCVSIs. The first layer, namely, *control*

layer 1, controls the VCVSIs. The second layer, namely, *control layer 2*, controls CCVSIs. The distributed control of multi-agent systems is used to implement each control layer. Each control layer is associated with a limited and sparse communication network. Figure 4-1 illustrates the two-layer microgrid control framework along with the communication networks. The communication topology for each layer should be a graph containing a spanning tree in which the implemented controller at each DG only requires information about that DG and its direct neighbors in the communication graph. Given the physical structure of the microgrid, it is not difficult to select a graph with a spanning tree that connects all DGs in an optimal fashion. Such optimal connecting graphs can be designed using operations research or assignment problem solutions. The optimization criteria can include minimal lengths of the communication links, maximal use of existing communication links, minimal number of links, and so on.

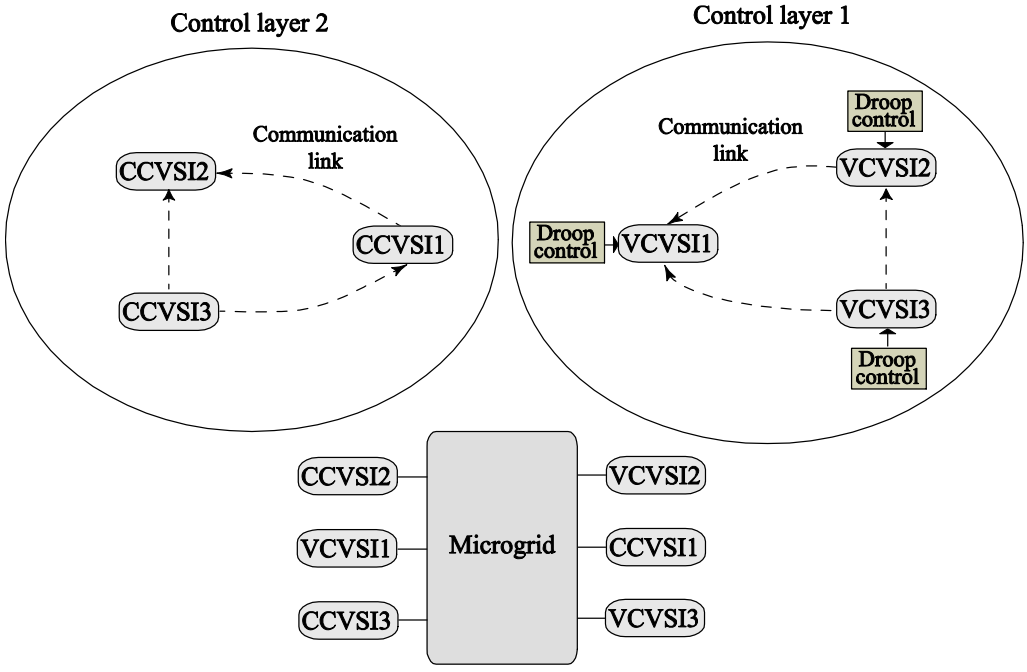

Figure 4-1 The Comprehensive Distributed Control of Microgrids with Two Control Layers

The *control layer 1* provides a framework to control VCVSIs in a distributed manner. This control layer has two main control parts, namely, frequency control and voltage control. Frequency control chooses ω_i^* such that the angular frequency of each VCVSI synchronizes to its nominal value, i.e. $\omega_i \to \omega_{ref}$. Additionally, it allocates the VCVSI output active powers according to

$$\frac{P_1}{P_{\max 1}} = \cdots = \frac{P_{N_V}}{P_{\max N_V}}, \tag{3,23}$$

where N_V is the number of VCVSIs in the islanded microgrid. $P_{\max i}$ denotes the active power rating of i^{th} VCVSI. Since the active droop coefficients D_{Pi} are chosen based on the active power ratings of VCVSIs,(3,23) is equivalent to

$$D_{P1}P_1 = \cdots = D_{PN_V}P_{N_V}. \tag{3,24}$$

The voltage control selects E_i^* in (3,22) such that the output voltage amplitudes of VCVSIs $v_{o,magi}$ return to the reference voltage, i.e. $v_{o,magi} \to v_{ref}$. If v_{ref} is set to the nominal voltage of microgrid $v_{nominal}$, the output voltage magnitude of VCVSIs synchronize to the nominal voltage of microgrid. However, v_{ref} can be chosen such that the voltage magnitude of a critical bus of microgrid synchronizes to $v_{nominal}$. In this case, v_{ref} is defined by (2,21).

The other objective of the voltage control can be defined as allocating the VCVSI output reactive powers according to

$$\frac{Q_1}{Q_{\max 1}} = \cdots = \frac{Q_{N_V}}{Q_{\max N_V}}, \tag{3,25}$$

where N_V is the number of VCVSIs in the islanded microgrid. $Q_{\max i}$ denotes the reactive power rating of i^{th} VCVSI. Since the reactive droop coefficients D_{Qi} are chosen based on the reactive power ratings of VCVSIs, (3,25) is equivalent to

$$D_{Q1}Q_1 = \cdots = D_{QN_V}Q_{N_V}. \tag{3,26}$$

The voltage droop characteristic in (3,22) is designed assuming a fully inductive microgrid. Therefore, (3,25) and (3,26) can be exactly satisfied in fully inductive microgrids, and hence small amount of mismatches among reactive power ratios can be observed in non inductive micrgrids.

While the *control layer 1* is active to control the voltage and frequency of microgrid by tuning VCVSIs, the *control layer 2* objectives for CCVSIs are to control the active and reactive powers of CCVSIs. The CCVSIs should provide active and reactive power supports for VCVSIs by compensating a portion of the consumed active and reactive power in the microgrid. Doing so, the VCVSIs can generate less active and reactive power, and save their active and reactive power capacities to provide a fast voltage and frequency control for future disturbances. The *control layer 2* sets the control inputs of CCVSIs such that their output active and reactive powers of satisfy

$$\frac{P_1}{P_{\max 1}} = \cdots = \frac{P_{Nc}}{P_{\max Nc}} = \alpha_P, \tag{3,27}$$

$$\frac{Q_1}{Q_{\max 1}} = \cdots = \frac{Q_{N_C}}{Q_{\max N_C}} = \alpha_Q, \tag{3,28}$$

where N_C is the number of CCVSIs in the islanded microgrid. $P_{\max i}$ and $Q_{\max i}$ denote the active and reactive power ratings of i^{th} CCVSIs. α_P and α_Q are pre-specified active and reactive power ratio references. Equations (3,27) and (3,28) show that the active and reactive power of CCVSIs must be allocated based on their active and reactive power ratings.

Dynamical Model of CCVSIs

The block diagram of a CCVSI based DG is shown in Figure 4-2. It contains an inverter bridge, connected to a primary dc power source. The current controller adjusts the direct and quadrature terms of output current i_{oi}. As seen in Figure 4-3, a control block is used to calculate the angle of the i^{th} CCVSI reference frame with respect to the common reference frame α_i such that the quadrature term of output voltage v_{oqi} becomes zero [111]. This control block is named

as α_i calculator.

The block diagram of the current controller is shown in Figure 4-4. The differential algebraic equations of the current controller are written as

$$\dot{\gamma}_{di} = i_{drefi} - i_{odi}, \tag{3,29}$$

$$\dot{\gamma}_{qi} = i_{qrefi} - i_{oqi}, \tag{3,30}$$

$$v_{idi}^{*} = v_{odi} - \omega_b L_{fi} i_{oqi} + K_{PCi}(i_{drefi} - i_{odi}) + K_{ICi}\gamma_{di}, \tag{3,31}$$

$$v_{iqi}^{*} = v_{oqi} + \omega_b L_{fi} i_{odi} + K_{PCi}(i_{qrefi} - i_{oqi}) + K_{ICi}\gamma_{qi}, \tag{3,32}$$

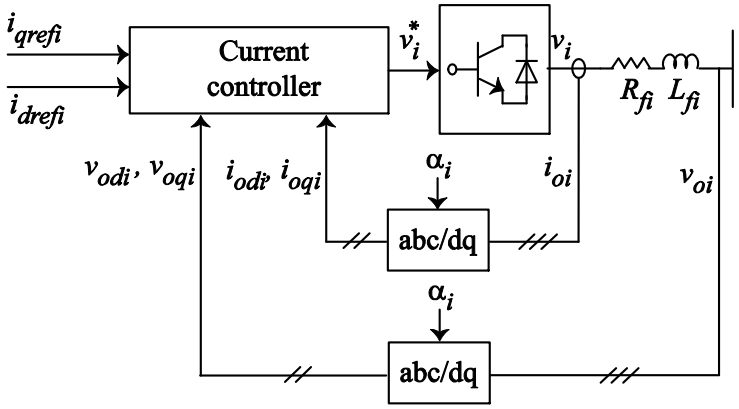

Figure 4-2 The Block Diagram of a CCVSI

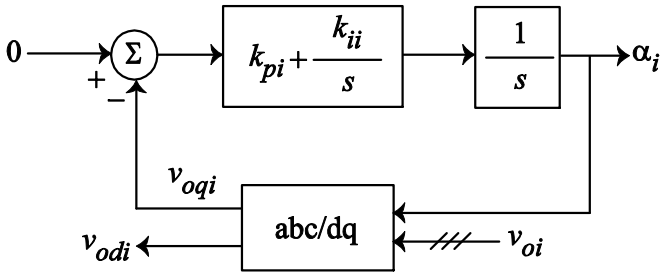

Figure 4-3 The Block Diagram of α_i Calculator

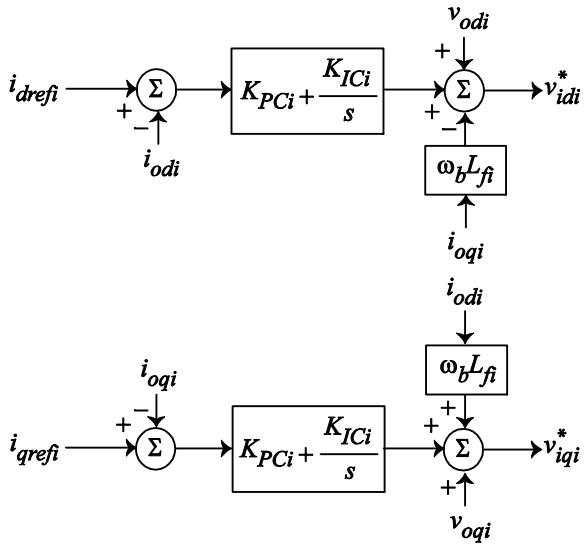

Figure. 4-4 The Block Diagram of the Current Controller for a CCVSI

where γ_{di} and γ_{qi} are the auxiliary state variables defined for the PI controllers in Figure 4-4. i_{odi} and i_{oqi} are the direct and quadrature components of output current i_{oi} in Figure 4-2. Other parameters are shown in Figure 4-2 and 4.4. Assuming that the inverter bridge produces the demanded voltage, i.e. $v^*_{idi} = v_{idi}$ and $v^*_{iqi} = v_{iqi}$, the dynamics of output RL filter can be written as

$$\dot{i}_{odi} = -\frac{R_{fi}}{L_{fi}} i_{odi} + \omega_{com} i_{oqi} + \frac{1}{L_{fi}} v_{idi} - \frac{1}{L_{fi}} v_{odi}, \tag{3,33}$$

$$\dot{i}_{oqi} = -\frac{R_{fi}}{L_{fi}} i_{oqi} - \omega_{com} i_{odi} + \frac{1}{L_{fi}} v_{iqi} - \frac{1}{L_{fi}} v_{oqi}. \tag{3,34}$$

Equations (3,29)-(3,34) form the large-signal dynamical model of the i^{th} CCVSI. The large-signal dynamical model can be written in a compact form as

$$\begin{cases} \dot{x}_{CCi} = \mathbf{f}_{CCi}(x_{CCi}) + \mathbf{k}_{CCi}(x_{CCi})\mathbf{D}_{CCi} + \mathbf{g}_{CCi}(x_{CCi})u_{CCi} \\ y_{CCi} = h_{CCi}(x_{CCi}) + d_{CCi}u_{CCi} \end{cases}, \tag{3,35}$$

where the state vector is

$$x_{CCi} = [\gamma_{di} \quad \gamma_{qi} \quad i_{odi} \quad i_{oqi}]^T. \tag{3,36}$$

The term $\mathbf{D}_{CCi}=[\omega_{com} v_{odi}]^T$ is considered as a known disturbance. The detailed expressions for $\mathbf{f}_{CCi}(x_{CCi})$, $\mathbf{g}_{CCi}(x_{CCi})$, and $\mathbf{k}_{CCi}(x_{CCi})$ can be extracted from (3,29) to (3,34).

The active and reactive power of CCVSI can be written as

$$P_i = v_{odi} i_{odi} + v_{oqi} i_{oqi} , \tag{3,37}$$

$$Q_i = v_{oqi} i_{odi} - v_{odi} i_{oqi} . \tag{3,38}$$

Since the α_i of each CCVSI is chosen such that v_{oqi} becomes zero, the output active and reactive powers P_i and Q_i in (3,37) and (3,38) can be written as

$$P_i = v_{odi} i_{odi} , \tag{3,39}$$

$$Q_i = -v_{odi} i_{oqi} . \tag{3,40}$$

Therefore, $P_i / P_{\max i}$ and $Q_i / Q_{\max i}$ can be tuned by controlling i_{odi} and i_{oqi}. Since i_{odi} is controlled by i_{drefi}, the output and control input in (3,35) are set to $y_{CCi} = \frac{P_i}{P_{\max i}}$ and $u_{CCi}=i_{drefi}$ for the active power control. Since i_{oqi} is controlled by i_{qrefi}, the output and control input in (3,35) are set to $y_{CCi} = \frac{Q_i}{Q_{\max i}}$ and $u_{CCi}=i_{qrefi}$ for the reactive power control.

Controller Design for Each Layer of the Proposed Control Framework

In this section, the control design procedure for VCVSIs and CCVSIs are elaborated.

Control Layer 1: Frequency and Voltage Control of VCVSIs

Frequency Control of VCVSIs

The distributed frequency control is to synchronize all of VCVSI frequencies to the nominal frequency. Additionally, it should allocate the output active power of VCVSIs based on their active power ratings, i.e. it should satisfy (3,23) and (3,24). In Chapter 3, the design procedure of the frequency control was elaborated. The distributed frequency control block diagram is shown in Figure 3-1.

Voltage Control of VCVSIs

In Chapter 2, the sole voltage control of VCVSI was discussed. In this chapter, the voltage and reactive power control of VCVSIs is considered. Therefore, the goal of voltage control is to choose appropriate control inputs E_i^* in (3,22) to synchronize the voltage magnitudes of VCVSIs $v_{o,magi}$ to the reference voltage v_{ref}, and allocate the output reactive power of VCVSIs based on their reactive power ratings, i.e. it satisfying (3,25) and (3,26). It should be noted that the voltage-droop characteristic in (3,22) is designed assuming a microgrid with inductive transmission lines. Therefore, small mismatches among reactive power ratios and voltage magnitudes can be observed in micrgrids where the transmission lines are not fully inductive.

According to (2,4), the synchronization of the voltage magnitudes of VCVSIs, $v_{o,magi}$, is equivalent to synchronizing the direct term of output voltages v_{odi}. To facilitate the simaltnous control of VCVSIs' voltage and reactive power, the fast dynamics of internal voltage and current controller in Figure 2-1 are neglected. Doing so, one can write $v^*_{o,magi}=v_{odi}$. Considering this fact, the differentiated voltage-droop characteristic in (3,22) is

$$\dot{E}_i^* = \dot{v}_{odi} + D_{Qi}\dot{Q}_i = v_{vi}, \tag{3,41}$$

where v_{vi} is an auxiliary control to be designed. Equation (3,41) is a dynamic system for computing the control input E_i^* from v_{vi}. The auxiliary control should be designed such that VCVSI voltage magnitudes synchronize to the reference voltage v_{ref}, and (3,25) is satisfied. According to (3,41), the voltage control of a microgrid including N_V VCVSIs is transformed to a synchronization problem for a first-order and linear multi-agent system

$$\begin{cases} \dot{v}_{od1} + D_{Q1}\dot{Q}_1 = v_{v1}, \\ \dot{v}_{od2} + D_{Q2}\dot{Q}_2 = v_{v2}, \\ \vdots \\ \dot{v}_{odN_V} + D_{QN_V}\dot{Q}_{N_V} = v_{vN_V}. \end{cases} \tag{3,42}$$

To achieve synchronization, it is assumed that VCVSIs can communicate with each other through the prescribed communication digraph Gr. The auxiliary controls v_{vi} are chosen based on each VCVSI's own information, and the information of its neighbors in the communication digraph as

$$v_{vi} = -c_v\Big(\sum_{j\in N_i} a_{ij}(v_{odi} - v_{odj}) + b_i(v_{odi} - v_{ref}) + \sum_{j\in N_i} a_{ij}(D_{Qi}Q_i - D_{Qj}Q_j)\Big), \qquad (3,43)$$

where $c_v \in R$ is the coupling gain. It is assumed that the pinning gain $b_i \geq 0$ is nonzero for one VCVSI that has the reference voltage v_{ref} information. Theorem 3.1 can be used to show that the auxiliary control in (3,43) synchronizes all VCVSI voltage amplitudes to v_{ref} and shares the output reactive power of VCVSIs based on their reactive power ratings. The reference voltage v_{ref} can be set to the nominal voltage of the microgrid to synchronize the VCVSI voltage magnitudes to the nominal voltage, or can be chosen according to (2,21) to control the voltage magnitude of a critical bus of microgrid.

The block diagram of the proposed voltage control is shown in Figure 4-5. As seen in this figure, the control input E_i^* is written as

$$E_i^* = \int v_{vi}dt. \qquad (3,44)$$

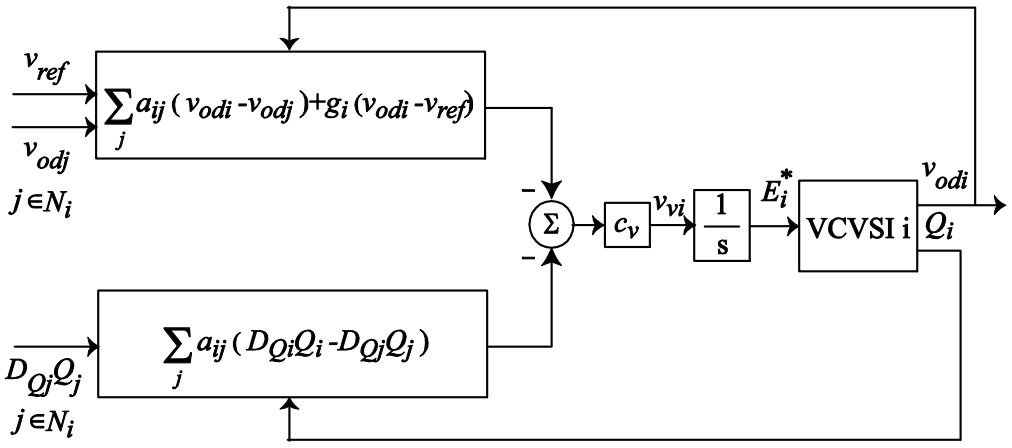

Figure 4-5 The Block Diagram of the Voltage Control in the Control Layer 1

Control Layer 2: Active and Reactive Power Control of CCVSIs

Active Power Control of CCVSIs

Subsequent to the islanding process, the active power of CCVSIs are required to be allocated based on their active power ratings which satisfies (3,27). Since the angle of the i^{th} CCVSI reference frame with respect to the common reference frame α_i is chosen such that the quadrature term of output voltage v_{oqi} becomes zero, the output active power P_i can be tuned by controlling the direct term of output current i_{odi} in Figure 4-2. Since i_{odi} is controlled by i_{drefi}, the output and control input in (3,35) are set to $y_{CCi} = \frac{P_i}{P_{\max i}}$ and $u_{CCi}=i_{drefi}$ for the active power control.

Input-output feedback linearization is used to generate a direct relationship between the output y_{CCi} and input u_{CCi}. According to (3,39), the derivative of P_i can be written as

$$\dot{P}_i = \dot{v}_{odi} i_{odi} + v_{odi} \dot{i}_{odi} . \tag{3,45}$$

Replacing $\dot{i}_{odi}$ by (3,33) and dividing both sides of (3,45) by $P_{\max i}$ yields

$$\dot{y}_{CCi} = \frac{\dot{v}_{odi} i_{odi}}{P_{\max i}} + \frac{v_{odi}}{P_{\max i}} (-\frac{R_{fi}}{L_{fi}} i_{odi} + \omega_{com} i_{oqi} + \frac{1}{L_{fi}} v_{idi} - \frac{1}{L_{fi}} v_{odi}) . \tag{3,46}$$

Replacing v_{idi} by (3,31) yields

$$\dot{y}_{CCi} = M_{Pi}(\mathbf{x}_{CCi}) + N_{Pi}(\mathbf{x}_{CCi}) u_{CCi} , \tag{3,47}$$

where

$$\begin{aligned} M_{Pi}(\mathbf{x}_{CCi}) &= \frac{v_{odi}}{P_{\max i}} (-\frac{R_{fi}}{L_{fi}} i_{odi} + \omega_{com} i_{oqi} - \frac{1}{L_{fi}} v_{odi}) \\ &+ \frac{v_{odi}}{P_{\max i} L_{fi}} (v_{odi} - \omega_b L_{fi} i_{oqi} - K_{PCi} i_{odi} + K_{ICi} \gamma_{di}) + \frac{\dot{v}_{odi} i_{odi}}{P_{\max i}}, \end{aligned} \tag{3,48}$$

and

$$N_{Pi}(\mathbf{x}_{CCi}) = \frac{v_{odi} K_{PCi}}{P_{\max i} L_{fi}} . \tag{3,49}$$

An auxiliary control $v_{Pi}$is defined as

$$v_{Pi} = M_{Pi}(\mathbf{x}_{CCi}) + N_{Pi}(\mathbf{x}_{CCi})u_{CCi}. \quad (3,50)$$

Therefore, (3,47) and (3,50) result in a 1st-order regulator synchronization problem with the following linear system dynamics

$$\dot{y}_{CCi} = v_{Pi}, \forall i. \quad (3,51)$$

By choosing appropriate v_{Pi}, the synchronization for y_{CCi} is provided. The control input u_{CCi} is implemented by v_{Pi} as

$$u_{CCi} = (N_{Pi}(\mathbf{x}_{CCi}))^{-1}(-M_{Pi}(\mathbf{x}_{CCi}) + v_{Pi}). \quad (3,52)$$

The auxiliary controls v_{Pi} are chosen based on each CCVSI's own information, and the information of its neighbors in the communication digraph as

$$v_{Pi} = -c_P(\sum_{j\in N_i} a_{ij}(\frac{P_i}{P_{\max i}} - \frac{P_j}{P_{\max j}}) + b_i(\frac{P_i}{P_{\max i}} - \alpha_P)), \quad (3,53)$$

where $c_P \in R$ is the coupling gain. It is assumed that the pinning gain $b_i \geq 0$ is nonzero for one CCVSI that has the reference active power ratio α_P. The block diagram of the proposed active power control is shown in Figure 4-6. In the following, the Lyapunov technique is used to show the effectiveness of the proposed active power control protocol in (3,53). The global active power neighborhood tracking error is defined as $e_P = \begin{bmatrix} e_{P1} & e_{P2} & \cdots & e_{PN_C} \end{bmatrix}^T = (L+G)(\underline{P} - \underline{\alpha}_P)$, where $\underline{P} = \begin{bmatrix} \frac{P_1}{P_{\max 1}} & \frac{P_2}{P_{\max 2}} & \cdots & \frac{P_{N_C}}{P_{\max N_C}} \end{bmatrix}^T$ and $\underline{\alpha}_P = \mathbf{1}_{N_C} \otimes \alpha_P$. The global active power auxiliary control input $v_P = \begin{bmatrix} v_{P1} & v_{P2} & \cdots & v_{PN_C} \end{bmatrix}^T$ is defined as

$$v_P = \begin{bmatrix} v_{P1} & v_{P2} & \cdots & v_{PN_C} \end{bmatrix}^T = -c_P e_P. \quad (3,54)$$

Consider the Lyapunov function candidate

$$V = \frac{1}{2} e_P^T P e_P, \quad (3,55)$$

where $P = diag\left\{ 1/w_i \right\}$, w_i are the elements of a vector w that satisfies $(L+G)w = \mathbf{1}_N$. Since the digraph $\mathcal{G}$ has a spanning tree and $k_i \neq 0$ for at least one root node, $L+G$ is nonsingular and a unique solution exists for w [82].

Differentiating (3,55) yields

$$\dot{V} = e_P^T P(L+G)v_P. \tag{3,56}$$

Defining $A \equiv L + G$, and placing (3,54) into (3,56) yields

$$\dot{V} = \frac{-c_P}{2} e_P^T (PA + A^T P) e_P. \tag{3,57}$$

From [82], $Q \equiv PA + A^T P$ is positive definite. Therefore, $\frac{c_P}{2} e_P^T Q e_P \geq \frac{c_P}{2} \sigma_{\min}(Q) \left\| e_P \right\|^2$, and hence

$$\frac{-c_P}{2} e_P^T Q e_P \leq \frac{-c_P}{2} \sigma_{\min}(Q) \left\| e_P \right\|^2. \tag{3,58}$$

According to (3,58)

$$\dot{V} \leq \frac{-c_P}{2} \underline{\sigma}(Q) \left\| e_P \right\|^2 \leq 0. \tag{3,59}$$

Equation proves that the global neighborhood tracking error asymptotically goes to zero, and hence, according to Lemma 2.2, the distributed control protocols in (3,53) synchronize all $P_i / P_{\max i}$ to α_P.

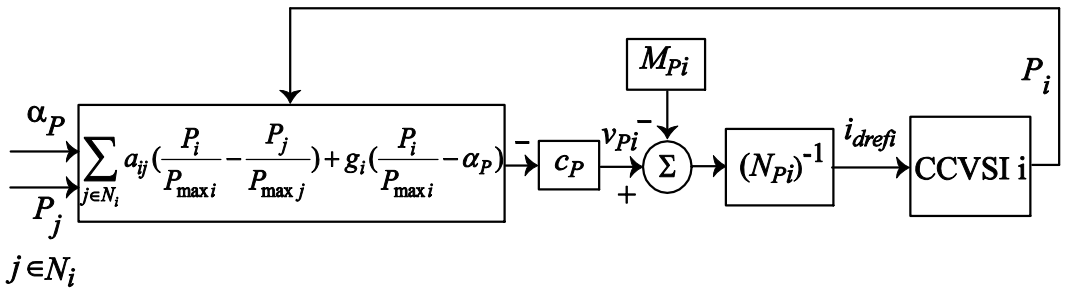

Figure 4-6 The Block Diagram of the Active Power Control in the Control Layer 2

Reactive Power Control of CCVSIs

Subsequent to the islanding process, the reactive power of CCVSIs should be shared based on their reactive power ratings satisfying (3,28). Since the angle of the i^{th} CCVSI reference frame with respect to the common reference frame α_i is chosen such that the quadrature term of output voltage v_{oqi} becomes zero, the output reactive power Q_i can be tuned by controlling the quadrature term of output current i_{oqi} in Figure 4-2. Since i_{oqi} is controlled by i_{qrefi}, the output and control input in (3,35) are set to $y_{CCi} = \frac{Q_i}{Q_{\max i}}$ and $u_{CCi}=i_{qrefi}$ for the reactive power control.

Input-output feedback linearization is used to generate a direct relationship between the output y_{CCi} and input u_{CCi}. According to (3,40), the derivative of Q_i can be written as

$$\dot{Q}_i = -\dot{v}_{odi} i_{oqi} - v_{odi} \dot{i}_{oqi} . \tag{3,60}$$

Replacing $\dot{i}_{oqi}$ by (3,34) and dividing both sides of (3,60) by $Q_{\max i}$ yields

$$\dot{y}_{CCi} = -\frac{\dot{v}_{odi} i_{oqi}}{Q_{\max i}} - \frac{v_{odi}}{Q_{\max i}}\left(-\frac{R_{fi}}{L_{fi}} i_{oqi} - \omega_{com} i_{odi} + \frac{1}{L_{fi}} v_{iqi} - \frac{1}{L_{fi}} v_{oqi}\right) . \tag{3,61}$$

Replacing *times* by (3,32) yields

$$\dot{y}_{CCi} = M_{Qi}(\mathbf{x}_{CCi}) + N_{Qi}(\mathbf{x}_{CCi}) u_{CCi} , \tag{3,62}$$

where

$$\begin{aligned} M_{Qi}(\mathbf{x}_{CCi}) = & -\frac{\dot{v}_{odi} i_{oqi}}{Q_{\max i}} - \frac{v_{odi}}{Q_{\max i}}\left(-\frac{R_{fi}}{L_{fi}} i_{oqi} - \omega_{com} i_{odi} - \frac{1}{L_{fi}} v_{oqi}\right) \\ & -\frac{v_{odi}}{Q_{\max i} L_{fi}}\left(v_{oqi} + \omega_b L_{fi} i_{odi} - K_{PCi} i_{oqi} + K_{ICi} \gamma_{qi}\right), \end{aligned} \tag{3,63}$$

and

$$N_{Qi}(\mathbf{x}_{CCi}) = -\frac{v_{odi} K_{PCi}}{Q_{\max i} L_{fi}} . \tag{3,64}$$

An auxiliary control v_{Qi} is defined as

$$v_{Qi} = M_{Qi}(\mathbf{x}_{CCi}) + N_{Qi}(\mathbf{x}_{CCi})u_{CCi}. \quad (3,65)$$

Therefore, (3,62) and (3,65) result in a 1st-order regulator synchronization problem with the following linear system dynamics

$$\dot{y}_{CCi} = v_{Qi}, \forall i. \quad (3,66)$$

By choosing appropriate v_{Qi}, the synchronization for y_{CCi} is provided. The control input u_{CCi} is implemented by v_{Qi} as

$$u_{CCi} = (N_{Qi}(\mathbf{x}_{CCi}))^{-1}(-M_{Qi}(\mathbf{x}_{CCi}) + v_i). \quad (3,67)$$

The auxiliary controls v_{Qi} are chosen based on each CCVSI's own information, and the information of its neighbors in the communication digraph as

$$v_{Qi} = -c_Q(\sum_{j\in N_i} a_{ij}(\frac{Q_i}{Q_{\max i}} - \frac{Q_j}{Q_{\max j}}) + b_i(\frac{Q_i}{Q_{\max i}} - \alpha_Q)), \quad (3,68)$$

where $c_Q \in R$ is the coupling gain. It is assumed that the pinning gain $b_i \geq 0$ is nonzero for one CCVSI that has the reference reactive power ratio α_Q. The block diagram of the proposed reactive power control is shown in Figure 4-7. The same procedure explained for active power control of CCVSIs can be used to show that all of $\frac{Q_i}{Q_{\max i}}$ synchronize to a α_Q and (3,28) is satisfied.

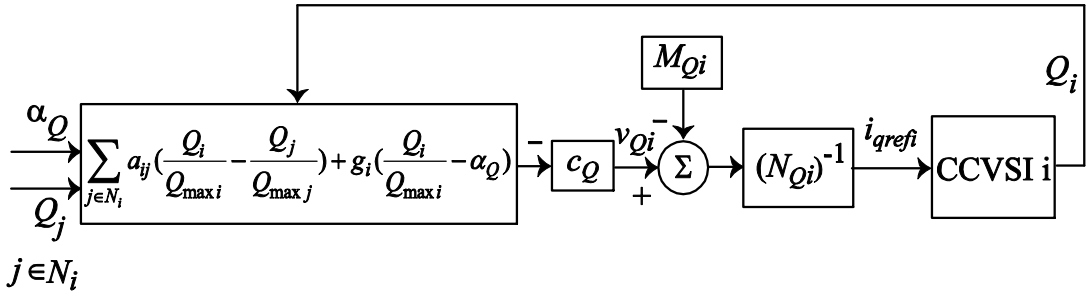

Figure 4-7 The Block Diagram of the Reactive Power Control in the Control Layer 2

Simulation Results for the Two-layer Multi-objective Control Framework

Simulation Results for the Microgrid Test System in Figure 4-8

The effectiveness of the proposed control schemes is verified by simulating an islanded microgrid in Matlab. Figure 4-8 illustrates the single line diagram of the microgrid test system. This microgrid consists of seven DGs including three VCVSIs (DGs 1, 5, 7) and four CCVSIs (DGs 2, 3, 4, 6). The lines between buses are modeled as series RL branches. The specifications of the DGs, lines, and loads are summarized in Appendix D. k_{pi} and k_{ii} in Figure 4-3 are set to 285 and 142500, respectively. The nominal line to line voltage and frequency of the microgrid are 380 V and 50 Hz, respectively. In the following, the simulation results are provided for three different cases, namely *Case 1*, *Case 2*, and *Case 3*. In *Cases 1* and *2*, a fixed communication network is exploited. In *Case 3,* the two-layer control framework is implemented through a time-varying communication network.

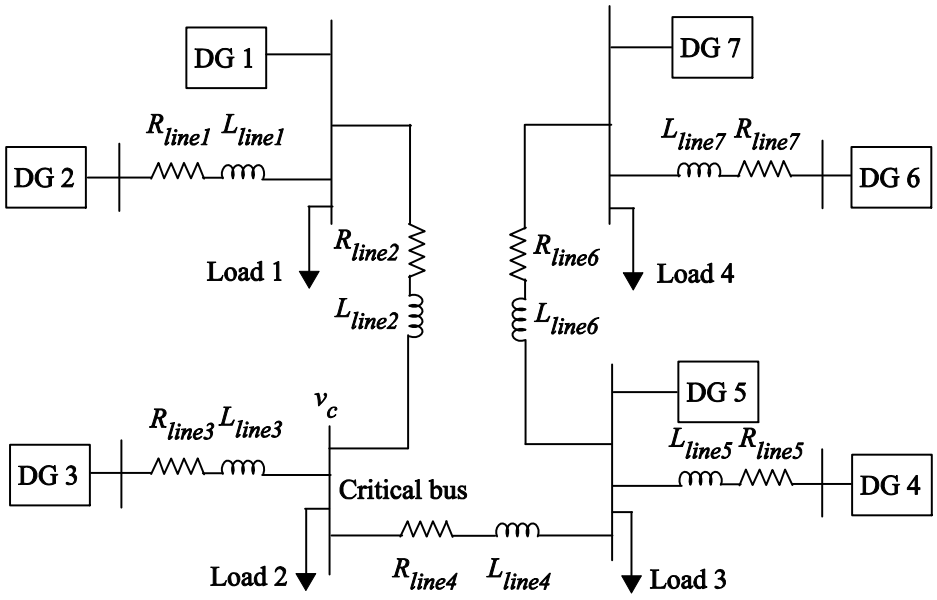

Figure 4-8 Single Line Diagram of the Microgrid Test System

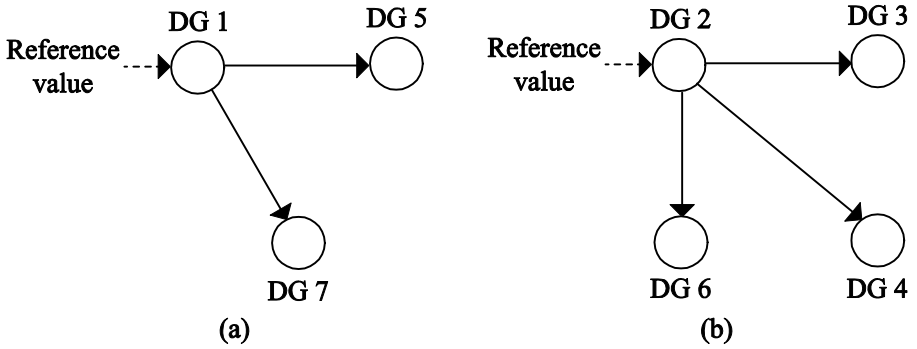

Figure 4-9 Topology of the Communication Digraph for (a) Control Layer 1 and (b) Control Layer 2

It is assumed that VCVSIs and CCVSIs communicate with each other through the communication digraphs depicted in Figures 4-9(a) and 4-9(b), respectively. These communication topologies are chosen based on the geographical location of DGs. The associated adjacency matrix of the digraphs in Figures 4-9(a) and 4-9(b), namely A_{G1} and A_{G2}, are

$$A_{G1} = \begin{bmatrix} 0 & 0 & 0 \\ 1 & 0 & 0 \\ 1 & 0 & 0 \end{bmatrix}, \tag{3,69}$$

and

$$A_{G2} = \begin{bmatrix} 0 & 0 & 0 & 0 \\ 1 & 0 & 0 & 0 \\ 1 & 0 & 0 & 0 \\ 1 & 0 & 0 & 0 \end{bmatrix}, \tag{3,70}$$

respectively. DG 1 is the only VCVSI that knows the voltage and frequency reference values and is connected to the leader node with the pinning gain b_1=1. DG 4 is the only CCVSI that knows the reference value of active and reactive power ratios α_P and α_Q with the pinning gain b_1=1. The coupling gains c_f and c_v in (3,9) and (3,43)are set to 30. The coupling gains c_P and c_Q in (3,53) and (3,68) are set to 30.

In the first case, namely *Case 1*, the reference frequency and voltage $f_{ref} = \omega_{ref} / 2\pi$ and v_{ref} are set to 50 Hz and 1 pu, respectively. The reference active and reactive power ratios are set to $\alpha_P = 0.4$ and $\alpha_Q = 0.3$, respectively. It should be noted that the proposed control framework always exists as a supervisory control level and take actions in the event of disturbances. However, to highlight the effectiveness of the proposed controls, it is assumed that the microgrid is islanded from the main grid at *t*=0, and the secondary control is applied at *t*=0.7 s. Figure 4-10(a) shows the VCVSIs frequencies. As seen in this figure, the frequency control of control layer 1 returns all VCVSIs frequencies to 50 Hz. Figure 4-10(b) shows the ratio of the active powers of VCVSIs with respect to their active power ratings, or equivalently $D_{Pi}P_i$. As seen in this figure, the proposed frequency control satisfies (3,24). Figure 4-11(a) shows the VCVSIs terminal voltage amplitudes. As seen in this figure, the voltage control of control layer 1 returns all VCVSIs terminal voltage amplitudes to a close vicinity of 1 pu. Figure 4-11(b) shows the ratio of the reactive powers of VCVSIs with respect to their reactive power ratings, or equivalently $D_{Qi}Q_i$. Since the microgrid test bed is not fully inductive, small mismatches among the DG reactive power ratios is observable. Figure 4-12(a) shows the ratio of the active powers of CCVSIs with respect to their active power ratings. As seen in this figure, the control layer 2 returns all of the active power ratios to the reference ratio and satisfies (3,27). Figure 4-12(b) shows the ratio of the reactive powers of CCVSIs with respect to their reactive power ratings. As seen in this figure, the control layer 2 returns all of the reactive power ratios to the reference ratio and satisfies (3,28). As seen in Figure 4-12, CCVSIs provide active and reactive power supports for VCVSIs by compensating a portion of the active and reactive power required for voltage and frequency restoration. Therefore, once the secondary control is applied, VCVSIs generate less active and reactive powers, as seen in Figures 4-10(b) and 4-11(b).

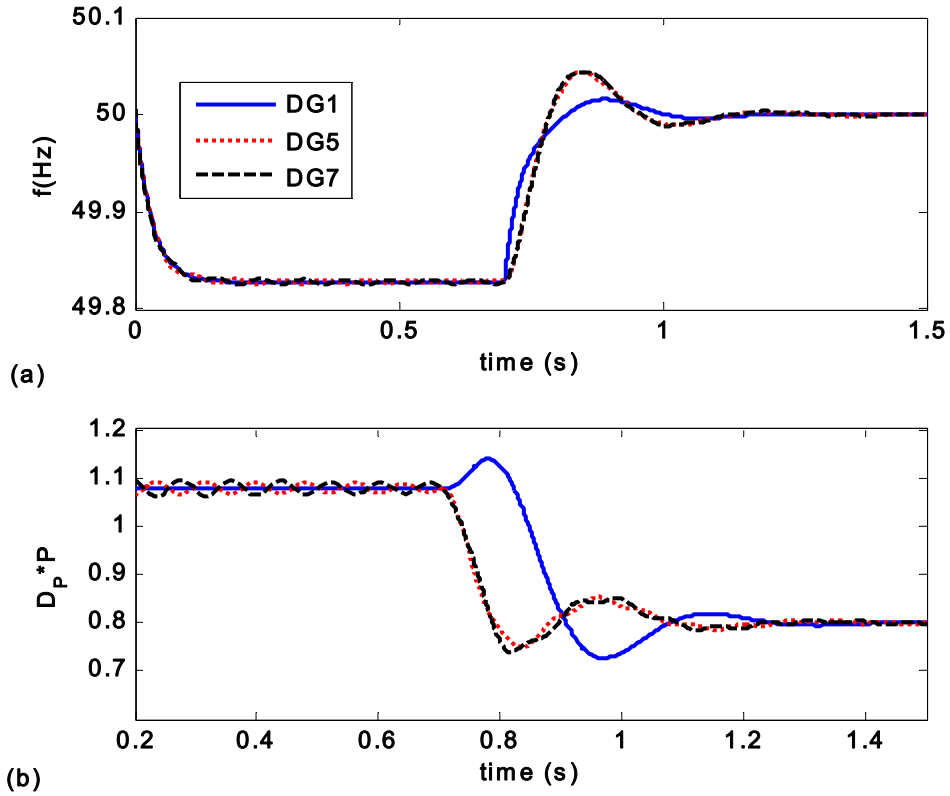

Figure 4-10 Frequency Control of Control Layer 1 in *Case 1*: (a) VCVSI Frequencies and (b) VCVSI Active Power Ratios $D_{Pi}P_i$

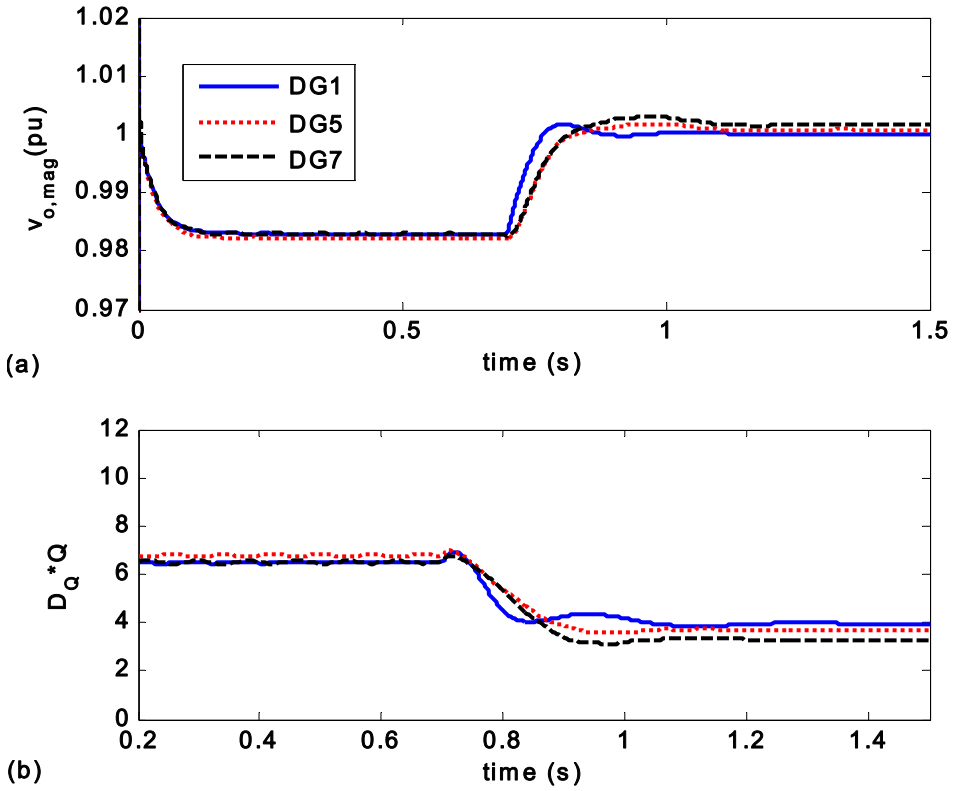

Figure 4-11 Voltage Control of Control Layer 1 in *Case 1*: (a) VCVSI Output Voltage Magnitudes and (b) VCVSI Reactive Power Ratios $D_{Qi}Q_i$

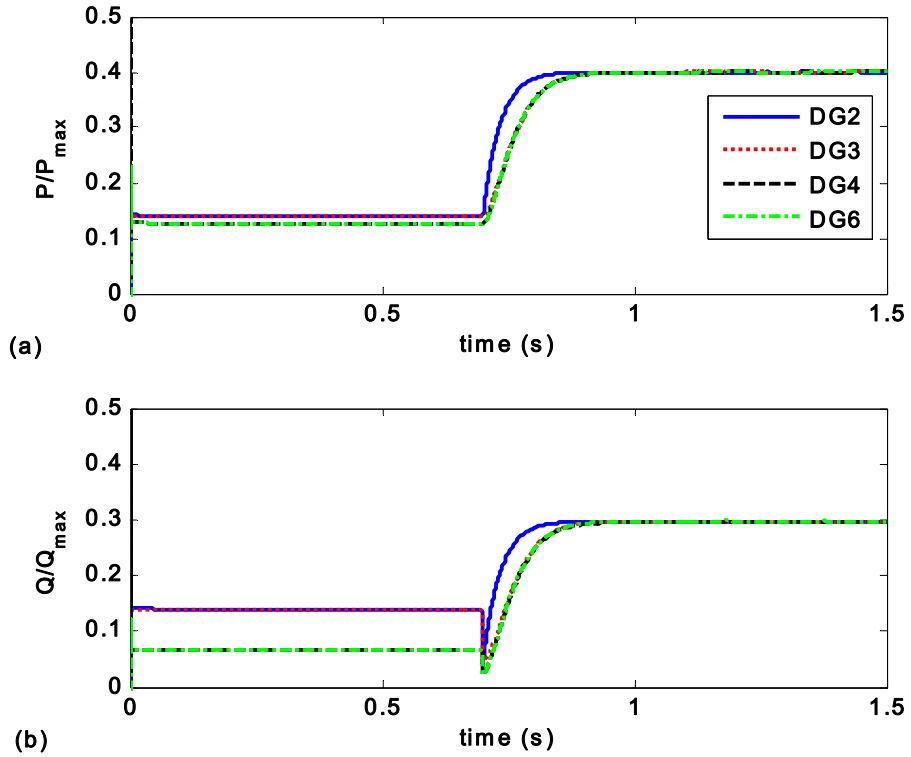

Figure 4-12 Active and Reactive Power Control of Control Layer 2 in *Case 1*: (a) CCVSI Active Power Ratios P_i/P_{maxi} and (b) CCVSI Reactive Power Ratios Q_i/Q_{maxi}

In the second case, namely *Case 2*, it is assumed that the reference frequency f_{ref}=50 Hz and the reference active and reactive power ratios are set to $\alpha_P = 0.6$ and $\alpha_Q = 0.6$, respectively. However, the aim of the voltage control of control layer 1 is to control the voltage of the critical bus, shown in Figure 4-8. Therefore, v_{ref} is implemented by (2,21) with k_{pc}=4, k_{ic}=40, and $v_{nominal}$=1 pu. The microgrid gets islanded from the main grid at *t*=0, and the secondary control is applied at *t*=0.7 s. Figure 4-13(a) shows the VCVSIs frequencies. As seen in this figure, the frequency control of control layer 1 returns all VCVSIs frequencies to 50 Hz. Figure 4-13(b) shows the ratio of the active powers of VCVSIs with respect to their active power ratings. As seen in this figure, the proposed frequency control satisfies (3,3). Figure 4-14(a)

shows the critical bus voltage amplitude. As seen in this figure, the voltage control of control layer 1 returns the critical bus voltage amplitude to 1 pu. Figure 4-14(b) shows the ratio of the reactive powers of VCVSIs with respect to their reactive power ratings. As seen in this figure, the proposed voltage control satisfies (3,25). Figure 4-15(a) shows the ratio of the active powers of CCVSIs with respect to their active power ratings. As seen in this figure, control layer 2 returns all of the active power ratios to the reference ratio and satisfies (3,27). Figure 4-15(b) shows the ratio of the reactive powers of CCVSIs with respect to their reactive power ratings. As seen in this figure, the control layer 2 returns all of the reactive power ratios to the reference ratio and satisfies (3,28). Compared to *Case 1*, greater α_P and α_Q are chosen for control layer 2 and, hence, VCVSIs generate less active and reactive powers, as seen in Figures 4-13(b) and 4-14(b).

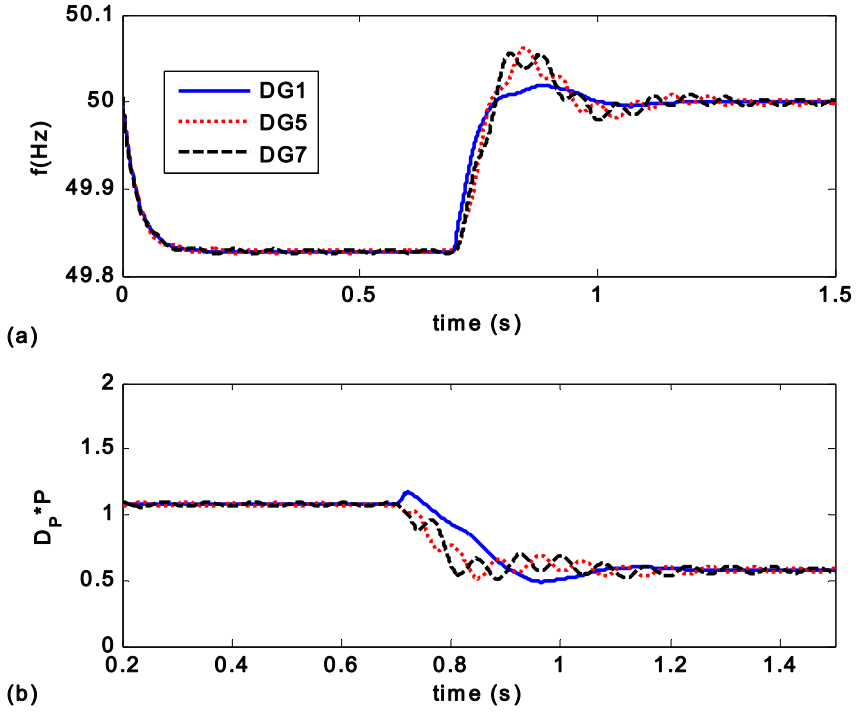

Figure 4-13 Frequency Control of Control Layer 1 in *Case 2*: (a) VCVSI Frequencies and (b) VCVSI Active Power Ratios $D_{Pi}P_i$

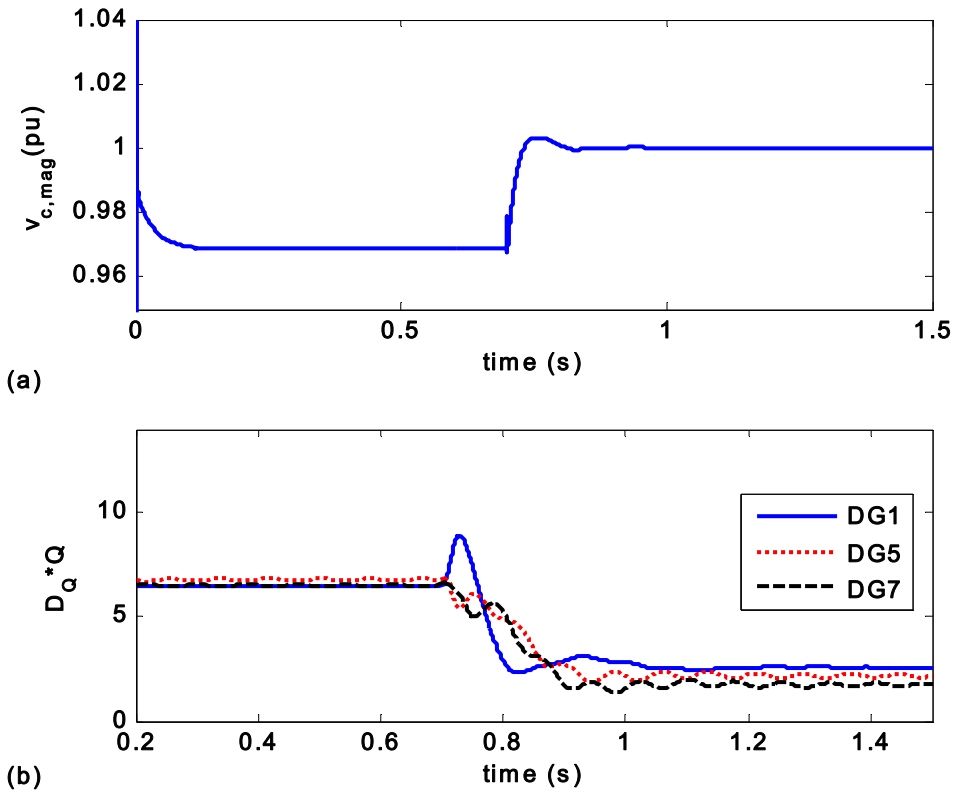

Figure 4-14 Voltage Control of Control Layer 1 in *Case 2*: (a) Critical Bus Voltage Magnitude and (b) VCVSI Reactive Power Ratios $D_{Qi}Q_i$

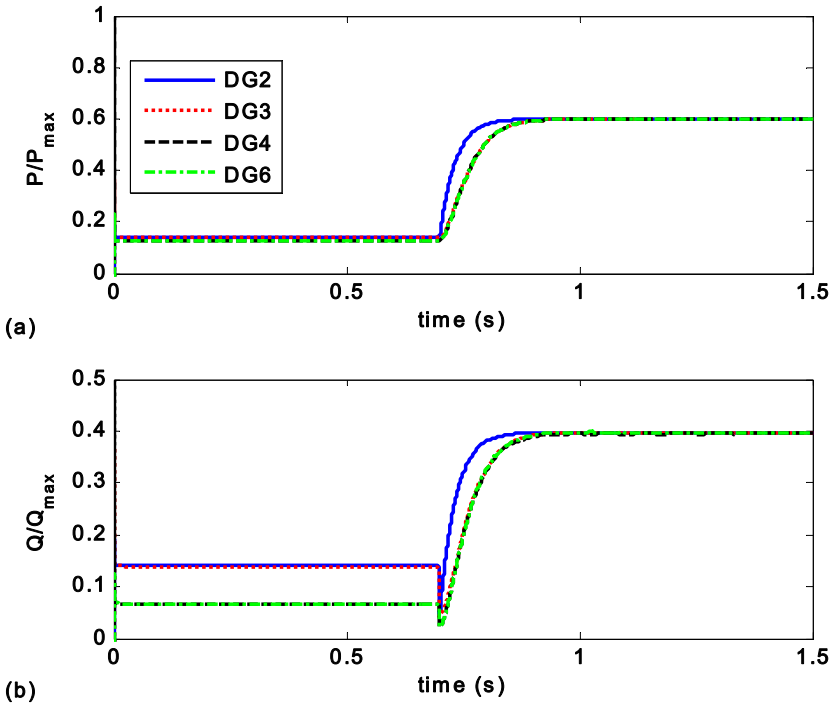

Figure 4-15 Active and Reactive Power Control of Control Layer 2 in *Case 2*: (a) CCVSI Active Power Ratios P_i/P_{maxi} and (b) CCVSI Reactive Power Ratios Q_i/Q_{maxi}

In *Case 3*, it is assumed that the microgrid is islanded from the main grid at *t*=0, and the frequency control is applied at *t*=0.7 s. However, as opposed to *Case 1*, the distributed control framework is associated by time-varying communication networks. Figure 4-16 shows the three communication network structures that are used in simulation. Each structure is adopted at a specific time interval. The communication digraph in Figure 4-16(a) models the communication network at the time interval [(0.7+0.15k) s, (0.7+0.15k)+0.05 s], for *k*=0,1,... The communication digraph in Figure 4-16(b) models the communication network at the time interval [(0.75+0.15k) s, (0.75+0.15k)+0.05 s], for k=0,1,... The communication digraph in Figure 4-16(c) models the communication network at the time interval [(0.8+0.15k) s, (0.8+0.15k)+0.05 s], for k=0,1,... It is seen that over the each 0.15 s period, the sequential completeness condition is satisfied. As seen in Figure 4-17(a), the control layer 1 returns all VCVSI frequencies to 50 Hz. Figure 4-

17(b) shows the active powers multiplied by the active power droop coefficients, i.e., $D_{Pi}P_i$, for VCVSIs. As seen, the frequency control satisfies the equality in (3,25). Figure 4-18(a) shows the terminal voltage amplitude of VCVSIs, where they are all returned to 1 pu. Figure 4-18(b) shows the reactive powers of VCVSIs multiplied by the reactive power droop coefficients, i.e., $D_{Qi}Q_i$. As seen, the voltage control satisfies the equality in (3,27). Figures 4-19(a) and 4-19(b) show the ratio of the active and reactive powers of CCVSIs with respect to their rated active and reactive powers. The control layer 2 returns all active and reactive power ratios to the reference ratios and satisfies (3,27) and (3,28). These simulation results verify the effectiveness of the proposed control framework in the case of time-varying communication networks and communication link failures.

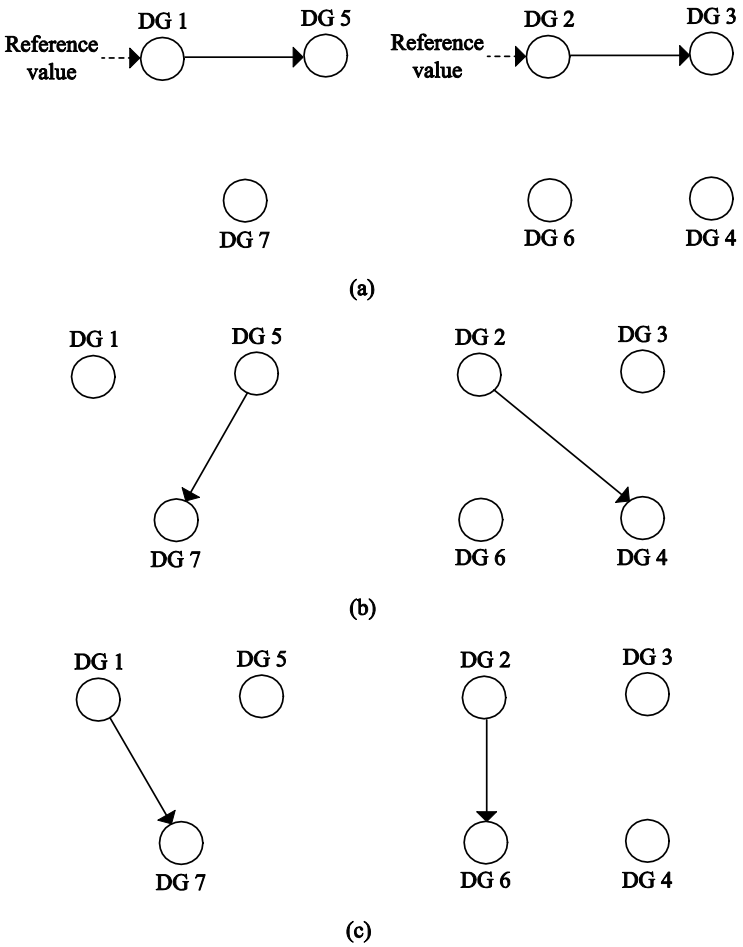

Figure 4-16 Communication Digraphs for the Time-Varying Communication Network in *Case 3*

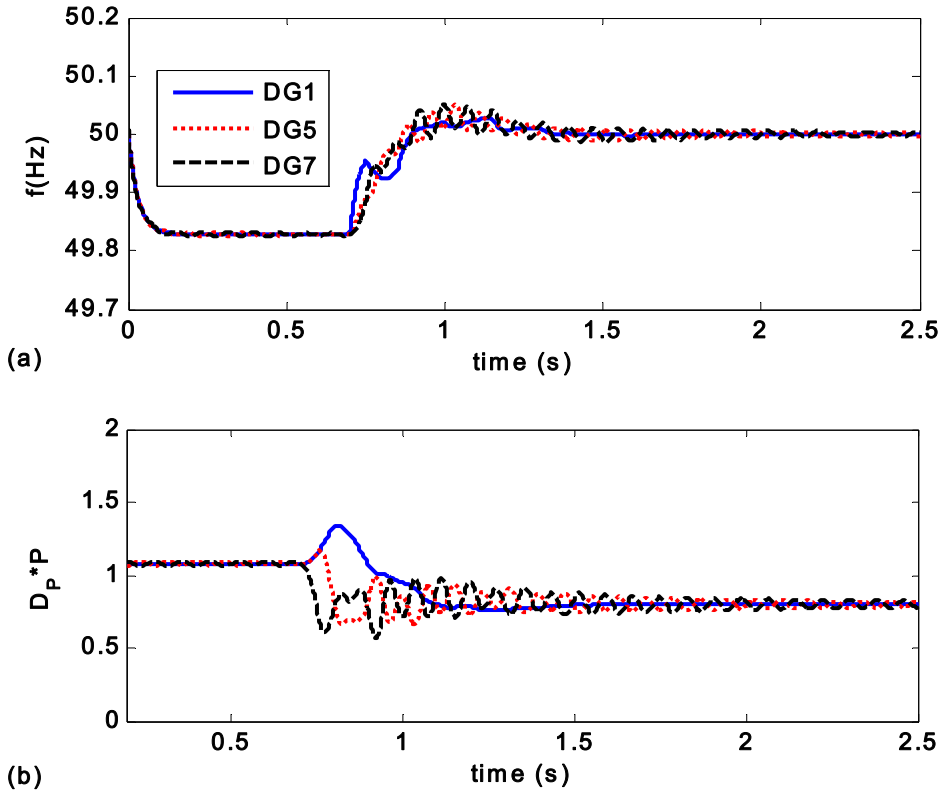

Figure 4-17 Frequency Control Using Control Layer 1 in *Case 3*: (a) VCVSI Frequencies and (b) VCVSI Active Power Ratios $D_{Pi}P_i$

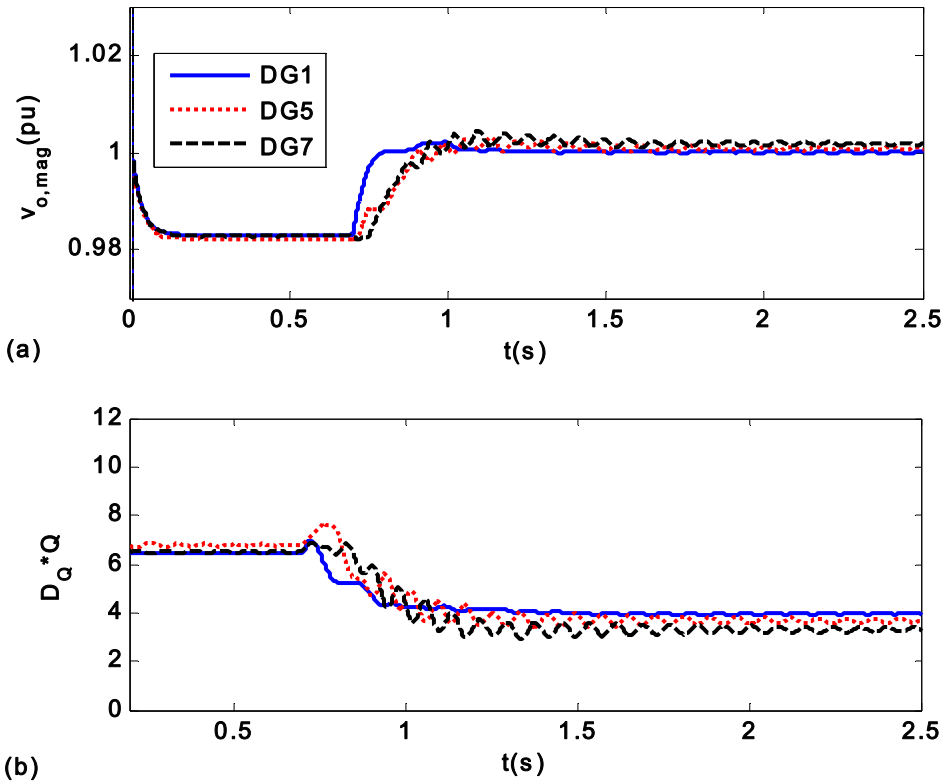

Figure 4-18 Voltage Control Using Control Layer 1 in *Case 3*: (a) Critical Bus Voltage Magnitude and (b) VCVSI Reactive Power Ratios $D_{Qi}Q_i$

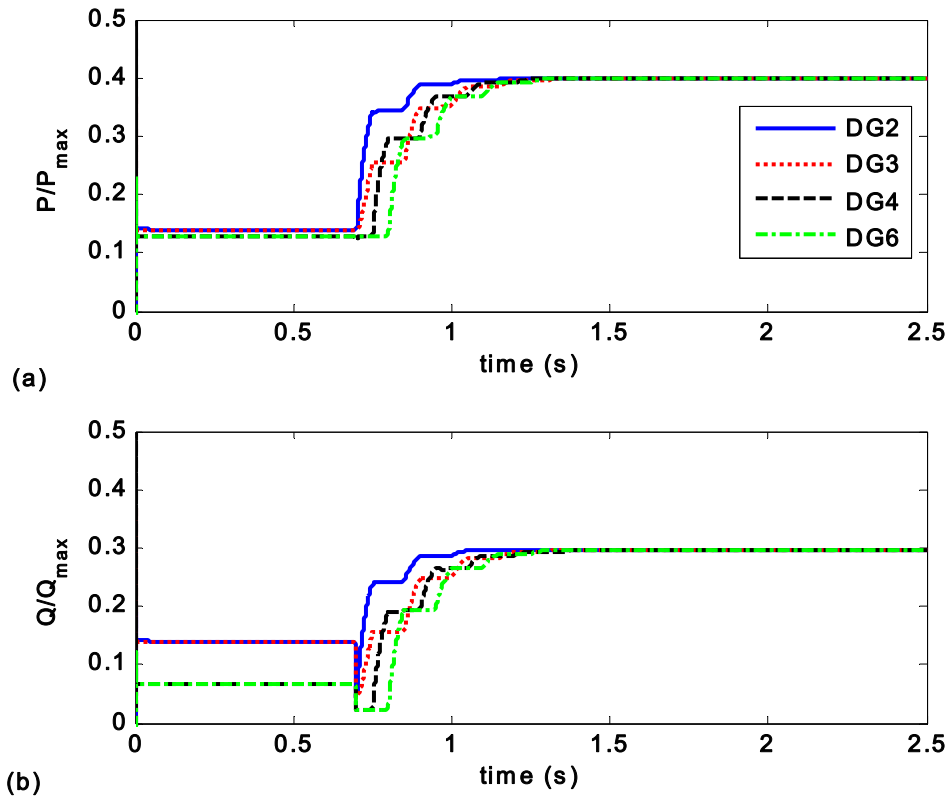

Figure 4-19 Active and Reactive Power Control Using Control Layer 2 in *Case 3*: (a) CCVSI Active Power Ratios P_i/P_{maxi} and (b) and CCVSI Reactive Power Ratios Q_i/Q_{maxi}

Simulation Results for the IEEE 34 Bus Test Feeder

Figure 4-20 illustrates the single-line diagram of the modified IEEE 34 bus test feeder. Six DGs including three VCVSIs (DGs 1, 2, 3) and three CCVSIs (DGs 4, 5, 6) are connected to the test feeder. This feeder is converted to a balanced feeder by averaging the line parameters. The specification of lines is provided in [112]. The specifications of the DGs and loads are summarized in Appendix E. The control coefficients k_{pi} and k_{ii} in Figure 4-3 are set to 285 and 142500, respectively. The nominal frequency and line-to-line voltage are set to 60 Hz and 24.9 kV, respectively. DGs are connected to the feeder through six Y-Y, 480 V/24.9 kV, 400 kVA transformers with the series impedance of 0.03+j0.12 pu. It is assumed that VCVSIs and

CCVSIs communicate through the communication digraphs depicted in Figures 4-21(a) and 4-21(b), respectively. DG 1 is the only VCVSI that knows the voltage and frequency reference values and is connected to the leader node with the pinning gain b_1=1. DG 4 is the only CCVSI that knows the reference value of active and reactive power ratios α_P and α_Q with the pinning gain b_1=1. The control gains c_f, c_v, c_P, and c_Q are all set to 30.

The reference frequency and voltage f_{ref} and v_{ref} are set to 60 Hz and 1 pu, respectively. The reference active and reactive power ratios are set to $\alpha_P = 0.7$ and $\alpha_Q = 0.6$. The test feeder is connected to the main grid at bus 800, shown in Figure 4-20. The test feeder is islanded from the main grid at *t*=0, resembling an islanded microgrid. The secondary control is applied at *t*=0.7 s. As seen in Figure 4-22(a), the control layer 1 returns all VCVSI frequencies to 60 Hz. Figure 4-22(b) shows the active powers multiplied by the active power droop coefficients, i.e., $D_{Pi}P_i$, for VCVSIs. As seen, the frequency control satisfies the equality in (3,25) . Figure 4-23(a) shows the terminal voltage amplitude of VCVSIs, where they are all returned to 1 pu. Figure 4-23(b) shows the reactive powers of VCVSIs multiplied by the reactive power droop coefficients, i.e., $D_{Qi}Q_i$. As seen, the voltage control tries to share the reactive power among VCVSIs based on their reactive power ratings, however, since the transmission lines are not purely inductive, small mismatches among the DG reactive power ratios is observed. Figure 4-24(a) shows the ratio of the active powers of CCVSIs with respect to their rated active powers. The control layer 2 returns all active power ratios to the reference ratio and satisfies (3,27). Figure 4-24(b) shows the ratio of the reactive powers of CCVSIs with respect to their reactive power ratings. As seen, the control layer 2 returns the reactive power ratios to the reference ratio and satisfies (3,28).

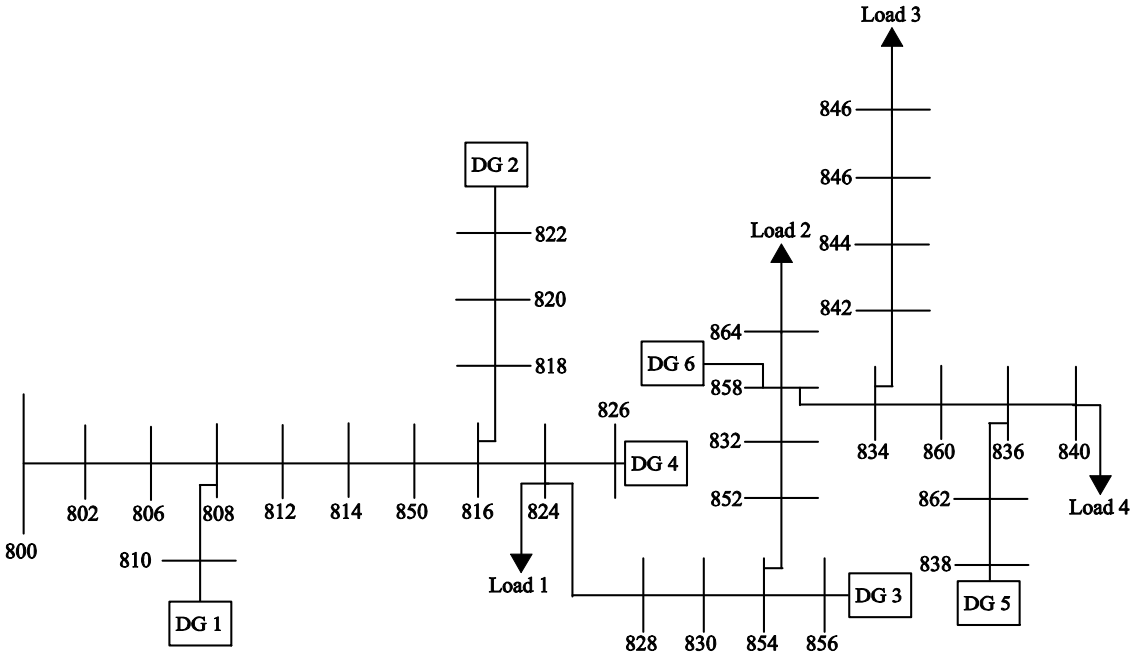

Figure 4-20 Single Line Diagram of Modified IEEE 34 Bus Test Feeder

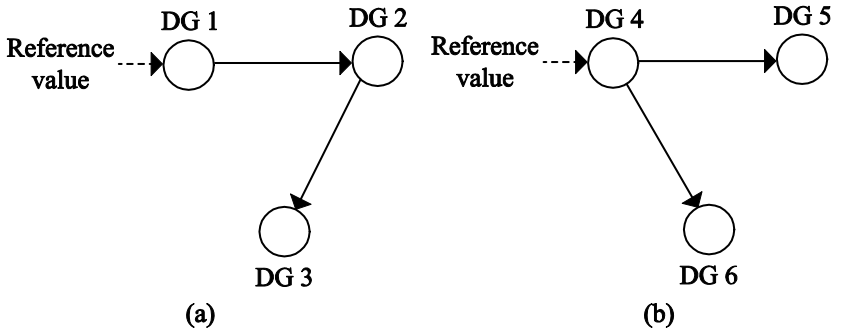

Figure 4-21 Communication Digraphs for IEEE 34 Bus test Feeder: (a) VCVSIs and (b) CCVSIs

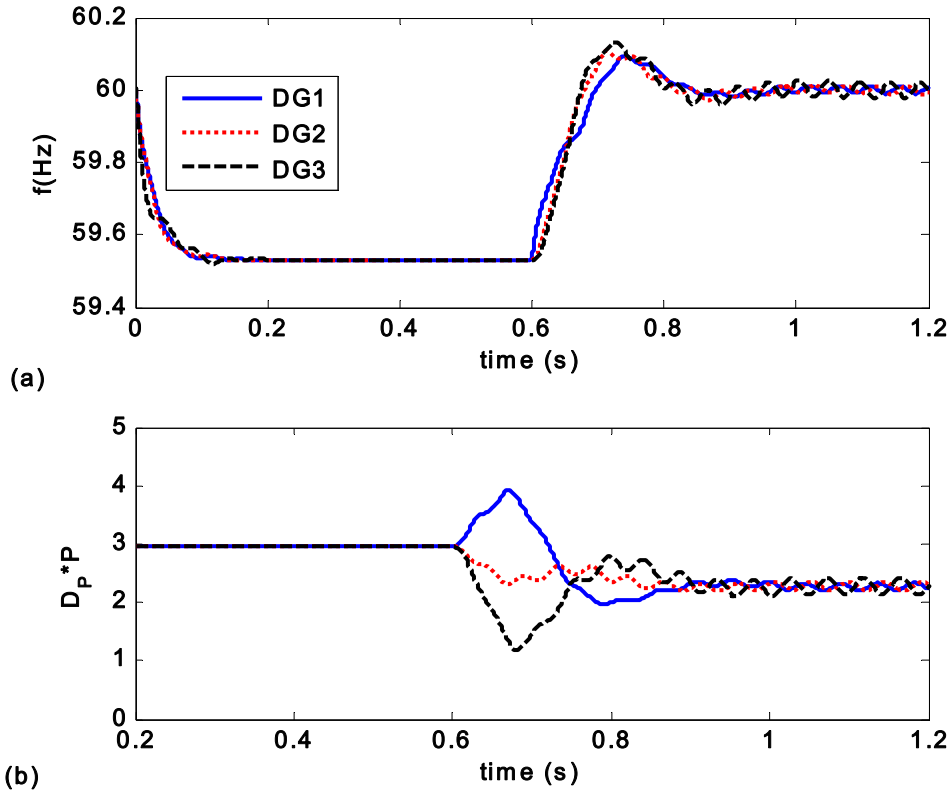

Figure 4-22 Frequency Control for IEEE 34 Bus Test Feeder: (a) VCVSI Frequencies and (b) VCVSI Active Power Ratios $D_{Pi}P_i$

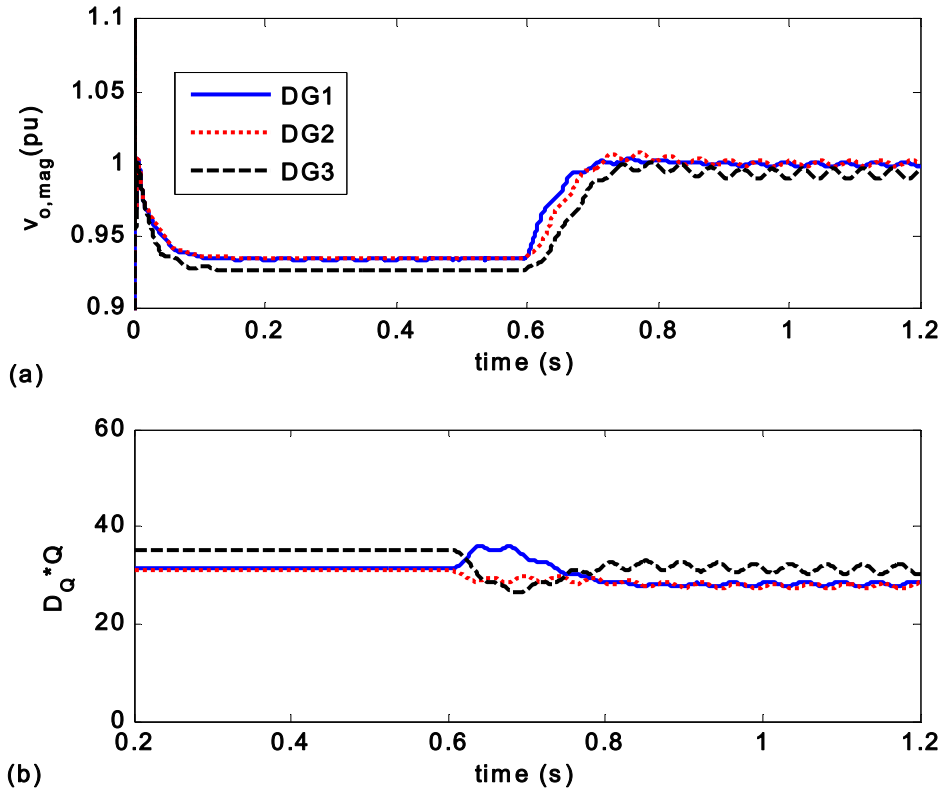

Figure 4-23 Voltage Control for IEEE 34 Bus Test Feeder: (a) VCVSI Output Voltage Magnitudes and (b) VCVSI Reactive Power Ratios $D_{Qi}Q_i$

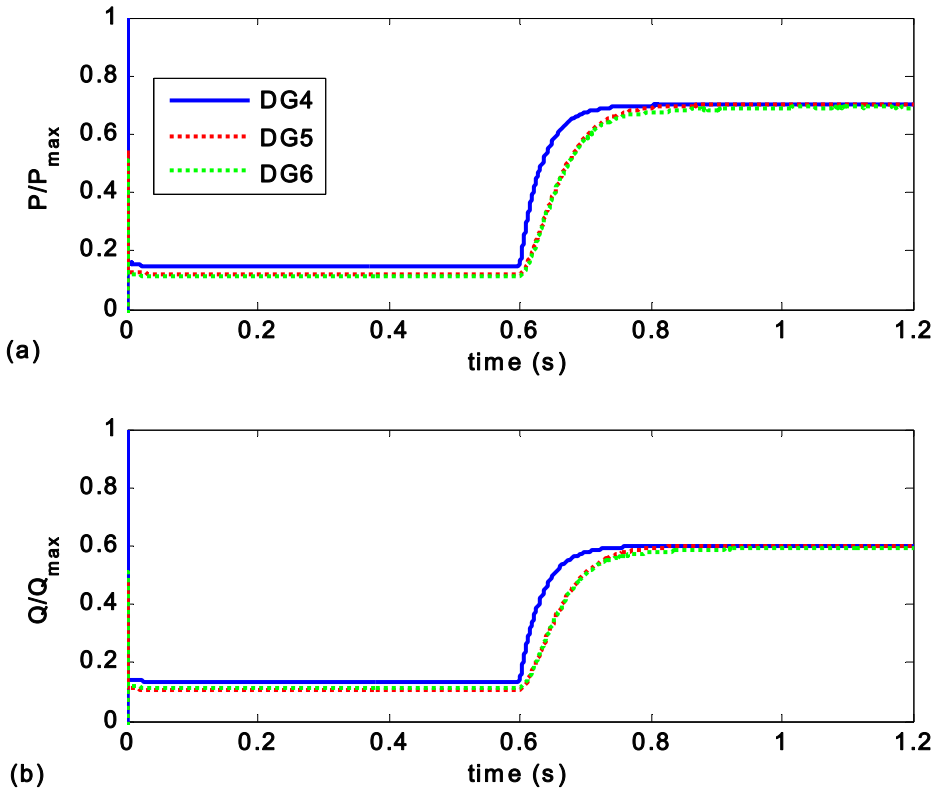

Figure 4-24 Active and Reactive Power Control for IEEE 34 Bus Test Feeder: (a) CCVSI Active Power Ratios P_i/P_{maxi} and (b) CCVSI Reactive Power Ratios Q_i/Q_{maxi}

Conclusion

A two-layer multi-objective control framework for microgrids is introduced. The proposed control framework facilitates the decoupled control of VCVSIs and CCVSIs with two main layers. The first layer deals with the voltage and frequency control of VCVSIs. The second layer is to control the active and reactive power of CCVSIs and provide active and reactive power support for VCVSIs. The proposed controllers are implemented through a communication network with one-way communication links, and are fully distributed such that each DG only requires its own information and the information of its neighbors on the communication network graph.

Chapter 5

Adaptive and Distributed Secondary Voltage Control of Microgrids

Introduction

In Chapter 2, the distributed secondary voltage control of microgrids was proposed. This chapter extends the distributed secondary voltage control proposed in Chapter 2, and proposes an adaptive and distributed secondary voltage control for microgrids with inverter-based DGs. The term adaptive [113]-[116] refers to the following salient features of the proposed controller:

- The proposed controller compensates for the nonlinear and uncertain dynamics of DGs and, hence, obviates the control design challenges caused by the nonlinear dynamics of DGs.
- The controller is fully independent of the DG parameters and the specification of the connector by which each DG is connected to the microgrid. Therefore, the controller can be deployed on any DG regardless of the DG parameters and the connector specifications and its performance does not deteriorate by the change in DG parameters (e.g., due to aging and thermal effects).
- The proposed controller appropriately responds to the changes in the system operating condition, without any manual intervention, and adjusts the control parameters in real time.

Linear-in-parameter neural networks (NN) are used to design an adaptive and distributed secondary voltage control. Neural networks are used to compensate for the uncertainties caused by the unknown dynamics of DGs [117]-[121]. The NN weights are the control parameters and are calculated in realtime. DGs are considered as agents that can communicate with each other through a communication network. This communication network is modeled by a directed graph (digraph). It is assumed that the DG nonlinear dynamical model and parameters are unknown. The Lyapunov technique is adopted to derive fully distributed control protocols for each DG.

The rest of this chapter is organized as follows. First, neural networks are adopted to design an adaptive secondary voltage control based on the distributed cooperative control. Then, the proposed control is verified using a microgrid test system.

Adaptive and Distributed Secondary Voltage Control

As discussed in Chapter 2, a microgrid resembles a nonlinear and heterogeneous multi-agent system, where each DG is an agent. The secondary control is similar to the tracking synchronization problem of multi-agent systems. It is assumed that all DGs can communicate with each other through a nested communication network. The communication network is modeled by the digraph Gr. $A_G=[a_{ij}] \in R^{N\times N}$ denotes the adjacency matrix of digraph Gr. In tracking synchronization problem, all agents synchronize to a leader node that acts as a command generator. The secondary voltage control chooses appropriate control inputs E_i^* in (2,4) to synchronize the voltage magnitudes of DGs $v_{o,magi}$ to the reference voltage v_{ref}. Synchronizing the voltage magnitudes $v_{o,magi}$ is equivalent to synchronizing the direct term of output voltages v_{odi}. Therefore, the secondary voltage control is a tracking synchronization problem in which u_i in (2,19) is chosen such that $y_i \rightarrow y_0, \forall i$, where the reference $y_0=v_{ref}$ is considered as the leader node output.

The dynamics of inverter-based DGs in (2,19) are nonlinear. In this chapter, input-output feedback linearization and neural networks are used to compensate for the nonlinear dynamics of DGs. As discussed in Chapter 2, in input-output feedback linearization, a direct relationship between the dynamics of the output y_i (or equivalently v_{odi}) and the control input u_i (or equivalently E_i^*) is generated by repetitively differentiating y_i with respect to time. For the dynamics of the i^{th} DG in (2,19), the direct relationship between the y_i and u_i is generated after the 2nd derivative of the output y_i. This direct relationship is shown in (2,23). The commensurate reformulated dynamics of each DG in (2,23) can be written as

$$\begin{cases} \dot{y}_{i,1} \equiv y_{i,2}, \\ \dot{y}_{i,2} = f_i(x_i) + g_i(x_i)u_i, \end{cases} \quad \forall i, \tag{4,1}$$

where $y_i \equiv y_{i,1}$, $f_i(x_i) \equiv L_{\mathbf{F}_i}{}^2 h_i$ and $g_i(x_i) \equiv L_{\mathbf{g}_i} L_{\mathbf{F}_i} h_i$.

Remark 5.1. The function $g_i(x_i)$ is equal to $\frac{1}{L_{fi} C_{fi}}$. Therefore, a positive constant g_{0i} exists such that $\left| \frac{d}{dt} \left(1 \big/ g_i(x_i) \right) \right| \leq g_{0i}$.

Using the input-output feedback linearization, each agent dynamics is decomposed into the 2nd-order dynamical system in (4,1) and a set of internal dynamics. It should be noted that since $y_0 = v_{ref}$ is constant, $\dot{y}_0 = 0$. Define $Y_i = \begin{bmatrix} y_{i,1} & y_{i,2} \end{bmatrix}^T$ and $Y_0 = \begin{bmatrix} y_{0,1} & y_{0,2} \end{bmatrix}^T = \begin{bmatrix} v_{ref} & 0 \end{bmatrix}^T$. The secondary voltage control is solved if a distributed u_i in (4,1) is found such that $Y_i \to Y_0, \forall i$. To design a controller independent of DG parameters, it is assumed that the nonlinear dynamics of DGs and, hence, functions $f_i(x_i)$ and $g_i(x_i)$ are unknown. Therefore, NNs should be exploited to design an adaptive control that compensates for the nonlinear and uncertain functions $f_i(x_i)$ and $g_i(x_i)$.

In this section, first, the sliding mode error is introduced. Then, the sliding mode errors are used to design adaptive and distributed secondary controls for each DG using the Lyapunov function technique.

Sliding Mode Error

For each DG, the cooperative team objective is expressed in terms of the local neighborhood tracking error

$$e_{i,m} = \sum_{j \in N_i} a_{ij} (y_{i,m} - y_{j,m}) + b_i (y_{i,m} - y_{0,m}), \tag{4,2}$$

where a_{ij} is the weight of the edge by which the j^{th} DG is connected to the i^{th} DG, and b_i is the pinning gain by which the i^{th} DG is connected to the leader node. For the secondary voltage control, the leader node contains the information of the voltage reference, i.e. $Y_0 = \begin{bmatrix} y_{0,1} & y_{0,2} \end{bmatrix}^T = \begin{bmatrix} v_{ref} & 0 \end{bmatrix}^T$. It should be noted that only a small portion of DGs need to be

pinned to the leader node. Define $e_i = \begin{bmatrix} e_{i,1} & e_{i,2} \end{bmatrix}^T$, $\delta_{i,m} = y_{i,m} - y_{0,m}$, $\delta_i = Y_i - Y_0$ (δ_i is called the local disagreement vector, and Y_0 is considered as the leader node dynamics.), $\mathbf{e} = \begin{bmatrix} e_1 & e_2 & \cdots & e_N \end{bmatrix}^T$, and $\boldsymbol{\delta} = \begin{bmatrix} \delta_1 & \delta_2 & \cdots & \delta_N \end{bmatrix}^T$. The global neighborhood tracking error $\mathbf{e}$ can be written as

$$\mathbf{e} = (L + B)\boldsymbol{\delta}, \tag{4,3}$$

where $B = diag\{b_i\}$.

The sliding mode error r_i for each DG is defined as

$$r_i = \lambda_1 e_{i,1} + \lambda_2 e_{i,2}. \tag{4,4}$$

The parameters λ_i are chosen such that the polynomial $\lambda_1 + \lambda_2 s$ is Hurwitz. Therefore, on the sliding surface $r_i = 0$, e_i exponentially goes to zero. The derivative of the sliding mode error can be written as

$$\dot{r}_i = \lambda_1 e_{i,2} + \sum_{j \in N_i} a_{ij}(f_i + g_i u_i - f_j - g_j u_j) + b_i(f_i + g_i u_i). \tag{4,5}$$

Defining $d_i = \sum_{j \in N_i} a_{ij}$, (4,5) can be reformulated as

$$\dot{r}_i = \lambda_1 e_{i,2} + (d_i + b_i)(f_i + g_i u_i) - \sum_{j \in N_i} a_{ij}(f_j + g_j u_j). \tag{4,6}$$

Define

$$E_{i,1} = \begin{bmatrix} e_{i,1} & e_{i,2} \end{bmatrix} \equiv e_i^T, \tag{4,7}$$

$$\Lambda = \begin{bmatrix} 0 & 1 \\ -\lambda_1 & -\lambda_2 \end{bmatrix}, \tag{4,8}$$

then,

$$\dot{E}_{i,1} = E_{i,1}\Lambda^T + r_i. \tag{4,9}$$

Note that Λ is Hurwitz. Therefore, given any symmetric and positive definite matrix P_i, a positive real number β_i exists such that

$$\Lambda^T P_i + P_i \Lambda = -\beta_i I, \tag{4,10}$$

where I is the identity matrix.

The Adaptive and Distributed Controller Design

The energy function

$$V_{ri} = \frac{1}{2}\frac{r_i^2}{g_i} \tag{4,11}$$

is considered [121]. This function is later used to design the adaptive control input u_i. The energy function V_{ri} will be used to develop a Lyapunov function. The developed Lyapunov function will be exploited to prove that the designed control input synchronizes the output voltage magnitudes of DGs. The adaptive control input u_i should be chosen such that the derivative of the developed Lyapunov function be locally negative definite.

Differentiating V_{ri} and replacing $\dot{r}_i$ from (4,6) yields

$$\begin{aligned} \dot{V}_{ri} &= \frac{1}{2}(-g_{i0} + \frac{-\dot{g}_i}{g_i^2})r_i^2 + r_i g_i^{-1}(-\sum_{j\in N_i} a_{ij}(f_j + g_j u_j)) + \\ & r_i g_i^{-1}(\lambda_1 e_{i,2} + (d_i + b_i)(f_i + g_i u_i) + \frac{g_i g_{i0} r_i}{2}), \end{aligned} \tag{4,12}$$

or equivalently

$$\dot{V}_{ri} = \frac{1}{2}(-g_{i0} + \frac{-\dot{g}_i}{g_i^2})r_i^2 + r_i \bar{f}_i + r_i \bar{g}_i + r_i(d_i + b_i)u_i, \tag{4,13}$$

where

$$\bar{f}_i = \frac{\lambda_1 e_{i,2} + (d_i + b_i) f_i}{g_i} + \frac{g_{i0} r_i}{2} \tag{4,14}$$

is a function of the local information available at the i^{th} DG, and

$$\overline{g}_i = -\frac{\sum_{j\in N_i} a_{ij}(f_j + g_j u_j)}{g_i} \tag{4,15}$$

is a function of the state variables of the i^{th} DG and the state variables of its neighboring DGs on the communication digraph.

To facilitate the adaptive control design, NNs are used to compensate for the nonlinear dynamics of $\overline{f}_i$ and $\overline{g}_i$ in (4,14) and (4,15) instead of the functions f_i and g_i in (4,1). The unknown nonlinear function $\overline{f}_i$ is approximated on a prescribed compact set $\Omega_{\overline{f}}$ by the linear-in-parameter NN [122]

$$\overline{f}_i = W_{\overline{f}_i}^T \phi_{\overline{f}_i}(e_{i,1}, e_{i,2}, x_i) + \varepsilon_{\overline{f}_i}, \tag{4,16}$$

where the NN weight vector is $W_{\overline{f}_i} \in R^{l_{\overline{f}_i}}$, $\varepsilon_{\overline{f}_i}$ is the NN estimation error, and $\phi_{\overline{f}_i} \in R^{l_{\overline{f}_i}}$ consists of a set of $l_{\overline{f}_i}$ basis functions. The NN structure is shown in Figure 5-1(a). As seen in this figure, $e_{i,1}$, $e_{i,2}$, and x_i are the NN inputs and $\hat{W}_{\overline{f}_i}^T \phi_{\overline{f}_i}$ is the NN output. The estimations of weight vectors are denoted as $\hat{W}_{\overline{f}_i}$. The error of the NN weights is defined as $\tilde{W}_{\overline{f}_i}^T = \hat{W}_{\overline{f}_i}^T - W_{\overline{f}_i}^T$. The unknown nonlinear function $\overline{g}_i$ is approximated by linear-in-parameter NNs

$$\overline{g}_i = W_{\overline{g}_i}^T \phi_{\overline{g}_i}(x_i, r_{-i}, x_{-i}, \hat{W}_{\overline{f}_{-i}}, \hat{W}_{\overline{g}_{-i}}) + \varepsilon_{\overline{g}_i}, \tag{4,17}$$

where the NN weight vector is $W_{\overline{g}_i} \in R^{l_{\overline{g}_i}}$, $\varepsilon_{\overline{g}_i}$ is the NN estimation error, and $\phi_{\overline{g}_i} \in R^{l_{\overline{g}_i}}$ consists of a set of $l_{\overline{g}_i}$ basis functions. The NN structure is shown in Figure 5-1(b). As seen in this figure, x_i, r_{-i}, x_{-i}, $\hat{W}_{\overline{f}_{-i}}$, and $\hat{W}_{\overline{g}_{-i}}$ are the NN inputs and $\hat{W}_{\overline{g}_i}^T \phi_{\overline{g}_i}$ is the NN output. The estimations of weight vectors are denoted as $\hat{W}_{\overline{g}_i}$. The terms r_{-i}, x_{-i}, $\hat{W}_{\overline{f}_{-i}}$, and $\hat{W}_{\overline{g}_{-i}}$ are the sliding mode error, states, and the NN estimated weight vectors of the neighbors of i^{th} DG on the communication digraph, respectively. The error of the NN weights is defined as $\tilde{W}_{\overline{g}_i}^T = \hat{W}_{\overline{g}_i}^T - W_{\overline{g}_i}^T$.

Remark 5.2. Considering Stone-Weierstrass approximation theorem [123], positive numbers $W_{\bar{f}_i}^M$, $\varepsilon_{\bar{f}_i}^M$, $W_{\bar{g}_i}^M$, and $\varepsilon_{\bar{g}_i}^M$ exist such that $\left|W_{\bar{f}_i}\right| \le W_{\bar{f}_i}^M$, $\left|\varepsilon_{\bar{f}_i}\right| \le \varepsilon_{\bar{f}_i}^M$, $\left|W_{\bar{g}_i}\right| \le W_{\bar{g}_i}^M$, and $\left|\varepsilon_{\bar{g}_i}\right| \le \varepsilon_{\bar{g}_i}^M$.

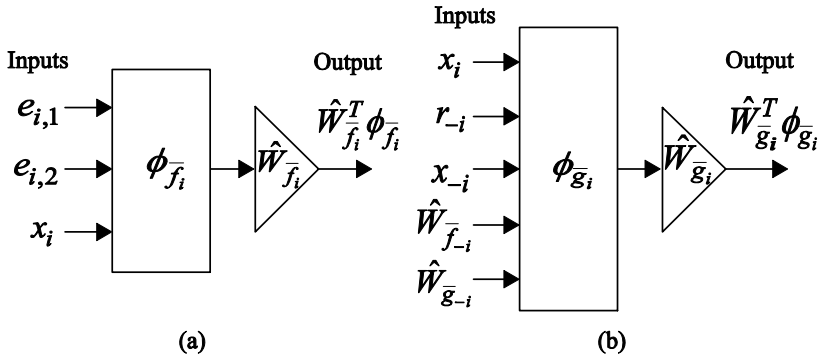

Figure 5-1 NN Structure for Estimating (a) $\bar{f}_i$ and (b) $\bar{g}_i$

Definition 5.1. The Y_i are cooperative uniformly ultimately-bounded (UUB) with respect to Y_0 if there exists a compact set $\Omega \subset R^r$ such that $\forall (Y_i(t_0) - Y_0(t_0)) \in \Omega$ there exists a bound B and a time $t_f(B, (Y_i(t_0) - Y_0(t_0)))$, both independent of t_0, where $\left\| Y_i(t_0) - Y_0(t_0) \right\| \le B, \forall t > t_0 + t_f$ [120].

Theorem 5.1. The commensurate reformulated dynamics of DGs in (4,1) are considered. Let the digraph Gr contain a spanning tree and $b_i \neq 0$ for at least one root node. It is assumed that the internal dynamics are asymptotically stable. Supposed that the control inputs are chosen as

$$u_i = -c_i r_i - \frac{\hat{W}_{\bar{f}_i}^T \phi_{\bar{f}_i}}{d_i + b_i} - \frac{\hat{W}_{\bar{g}_i}^T \phi_{\bar{g}_i}}{d_i + b_i}, \tag{4,18}$$

where c_i is the coupling gain, and the tuning laws are chosen as

$$\dot{\hat{W}}_{\bar{f}_i} = F_{\bar{f}_i} \phi_{\bar{f}_i} r_i - \kappa_{\bar{f}_i} F_{\bar{f}_i} \hat{W}_{\bar{f}_i}, \tag{4,19}$$

$$\dot{\hat{W}}_{\bar{g}_i} = F_{\bar{g}_i} \phi_{\bar{g}_i} r_i - \kappa_{\bar{g}_i} F_{\bar{g}_i} \hat{W}_{\bar{g}_i}, \tag{4,20}$$

where the arbitrary positive definite matrices $F_{\bar{f}_i} \in R^{l_{\bar{f}_i} \times l_{\bar{f}_i}}$ and $F_{\bar{g}_i} \in R^{l_{\bar{g}_i} \times l_{\bar{g}_i}}$ and the coefficients $\kappa_{\bar{f}_i}$ and $\kappa_{\bar{g}_i} > 0$ are design parameters. Then, Y_i is cooperative UUB with respect to Y_0 and,

hence, the direct term of DG output voltages v_{odi} synchronizes to v_{ref}, if c_i is chosen as

$$c_i > \frac{\bar{\sigma}^2(P_i)}{2\beta_i(d_i + b_i)}. \tag{4,21}$$

where $\bar{\sigma}(P_i)$ denotes the maximum singular value of P_i in (4,10), and β_i is calculated from (4,10).

Proof: The Lyapunov function candidate for each agent is considered as

$$V_i = \frac{1}{2}\frac{r_i^2}{g_i} + \frac{1}{2}\tilde{W}_{\bar{f}_i}^T F_{\bar{f}_i}^{-1}\tilde{W}_{\bar{f}_i} + \frac{1}{2}\tilde{W}_{\bar{g}_i}^T F_{\bar{g}_i}^{-1}\tilde{W}_{\bar{g}_i} + \frac{1}{2}E_{i1}P_iE_{i1}^T. \tag{4,22}$$

The derivative of V_i is written as

$$\begin{aligned}\dot{V}_i &= \frac{1}{2}(-g_{i0} + \frac{-\dot{g}_i}{g_i^2})r_i^2 + r_i\bar{f}_i + r_i\bar{g}_i + r_i(d_i + b_i)u_i \\ &+\tilde{W}_{\bar{f}_i}^T F_{\bar{f}_i}^{-1}\dot{\hat{W}}_{\bar{f}_i} + \tilde{W}_{\bar{g}_i}^T F_{\bar{g}_i}^{-1}\dot{\hat{W}}_{\bar{g}_i} + \dot{E}_{i1}P_iE_{i1}^T.\end{aligned} \tag{4,23}$$

Placing (4,18), (4,19), (4,20), and(4,9)into (4,23) yields

$$\begin{aligned}\dot{V}_i &= \frac{1}{2}(-g_{i0} + \frac{-\dot{g}_i}{g_i^2})r_i^2 - c_i(d_i + b_i)r_i^2 - \kappa_{\bar{f}_i}\tilde{W}_{\bar{f}_i}^T W_{\bar{f}_i} - \kappa_{\bar{f}_i}\left|\tilde{W}_{\bar{f}_i}\right|^2 \\ &-\kappa_{\bar{g}_i}\tilde{W}_{\bar{g}_i}^T W_{\bar{g}_i} - \kappa_{\bar{g}_i}\left|\tilde{W}_{\bar{g}_i}\right|^2 + E_{i1}\Lambda^T P_iE_{i1}^{\ T} + r_iP_iE_{i1}^{\ T} + \varepsilon_{\bar{f}_i} + \varepsilon_{\bar{g}_i}.\end{aligned} \tag{4,24}$$

Placing (4,10) into (4,24) yields

$$\begin{aligned}\dot{V}_i &= \frac{1}{2}(-g_{i0} + \frac{-\dot{g}_i}{g_i^2})r_i^2 - c_i(d_i + b_i)r_i^2 - \kappa_{\bar{f}_i}\tilde{W}_{\bar{f}_i}^T W_{\bar{f}_i} - \kappa_{\bar{f}_i}\left|\tilde{W}_{\bar{f}_i}\right|^2 \\ &-\kappa_{\bar{g}_i}\tilde{W}_{\bar{g}_i}^T W_{\bar{g}_i} - \kappa_{\bar{g}_i}\left|\tilde{W}_{\bar{g}_i}\right|^2 - \frac{\beta_i}{2}E_{i1}E_{i1}^{\ T} + r_iP_iE_{i1}^{\ T} + \varepsilon_{\bar{f}_i} + \varepsilon_{\bar{g}_i}.\end{aligned} \tag{4,25}$$

According to the Remarks 5.1 and 5.2

$$\begin{aligned}\dot{V} &\le -c_i(d_i + b_i)r_i^2 + \kappa_{\bar{f}_i}\left|\tilde{W}_{\bar{f}_i}\right|W_{\bar{f}_i}^M - \kappa_{\bar{f}_i}\left|\tilde{W}_{\bar{f}_i}\right|^2 + \kappa_{\bar{g}_i}\left|\tilde{W}_{\bar{g}_i}\right|^2 W_{\bar{g}_i}^M \\ &-\kappa_{\bar{g}_i}\left|\tilde{W}_{\bar{g}_i}\right|^2 - \frac{\beta_i}{2}\left|E_{i1}\right| + \left|r_i\right|\bar{\sigma}(P_i)\left|E_{i1}\right| + \varepsilon_{\bar{f}_i}^M + \varepsilon_{\bar{g}_i}^M.\end{aligned} \tag{4,26}$$

Equation (4,26) can be written as

$$\dot{V} \le -H^T SH + G^T H, \tag{4,27}$$

where

$$H = \begin{bmatrix} |E_{i1}| & \left|\tilde{W}_{\bar{f}_i}\right| & \left|\tilde{W}_{\bar{g}_i}\right| & |r_i| \end{bmatrix}^T, \tag{4,28}$$

$$S = \begin{bmatrix} \frac{\beta_i}{2} & 0 & 0 & \frac{\bar{\sigma}(P_i)}{2} \\ 0 & \kappa_{\bar{f}_i} & 0 & 0 \\ 0 & 0 & \kappa_{\bar{g}_i} & 0 \\ \frac{\bar{\sigma}(P_i)}{2} & 0 & 0 & c_i(d_i + b_i) \end{bmatrix}, \tag{4,29}$$

$$G = \begin{bmatrix} 0 & \kappa_{\bar{f}_i} W_{\bar{f}_i}^M & \kappa_{\bar{g}_i} W_{\bar{g}_i}^M & 0 \end{bmatrix}^T. \tag{4,30}$$

If the following conditions hold,

1) S is positive definite, and

2) $\|H\| > \frac{\|G\|}{\underline{\sigma}(S)}$.

then $\dot{V}_i < 0$.

According to Sylvester's criterion, S is positive-definite if

$$c_i > \frac{\bar{\sigma}^2(P_i)}{2\beta_i(d_i + b_i)}. \tag{4,31}$$

Since $\|G\|_1 \ge \|G\|_2 \ge \cdots \ge \|G\|_\infty$, the second condition holds if

$$\begin{cases} |E_{i1}| > \frac{\|G\|_1}{\underline{\sigma}(S)}, \\ \left|\tilde{W}_{\bar{f}_i}\right| > \frac{\|G\|_1}{\underline{\sigma}(S)}, \\ \left|\tilde{W}_{\bar{g}_i}\right| > \frac{\|G\|_1}{\underline{\sigma}(S)}, \\ |r_i| > \frac{\|G\|_1}{\underline{\sigma}(S)}. \end{cases} \tag{4,32}$$

where $\underline{\sigma}(S)$ is the minimum singular value of S.

Therefore, the sliding-mode error and the NN weights approximation errors are ultimately bounded by $\frac{\|G\|_1}{\underline{\sigma}(S)}$. Since the sliding-mode errors are ultimately bounded, the local neighborhood tracking errors in (4,2) are also bounded [120]. According to Lemma 2.2, δ_i are also ultimately bounded and, hence, all Y_i are cooperative UUB with respect to Y_0, and, hence, the direct term of DG output voltages v_{odi} synchronizes to v_{ref}. This completes the proof.

Remark 5.3. The coupling gain affects the controller speed; the greater value of c_i increases the controller synchronization speed. Additionally, the synchronization speed is affected by λ_1 and λ_2 in (4,4). Greater value of λ_2 with respect to λ_1 forces the local neighborhood tracking error $e_{i,m}$ in (2,31) to converge to zero faster, and, hence, increases the synchronization speed. The neural network weight estimations, $\hat{W}_{\bar{f}_i}$ and $\hat{W}_{\bar{g}_i}$, are the adaptive weights in the control law in (4,18). They are tuned adaptively online in real-time, without manual intervention, using the tuning laws in (4,19) and (4,20). By contrast, $F_{\bar{f}_i} \in R^{l_{\bar{f}_i} \times l_{\bar{f}_i}}$, $F_{\bar{g}_i} \in R^{l_{\bar{g}_i} \times l_{\bar{g}_i}}$, $\kappa_{\bar{f}_i}$, and $\kappa_{\bar{g}_i}$ in the tuning laws in (4,19) and (4,20) are the fixed design constants that are selected by the designer to obtain suitable convergence properties of the adaptive tuning laws. The design constants $F_{\bar{f}_i} \in R^{l_{\bar{f}_i} \times l_{\bar{f}_i}}$, $F_{\bar{g}_i} \in R^{l_{\bar{g}_i} \times l_{\bar{g}_i}}$, $\kappa_{\bar{f}_i}$, and $\kappa_{\bar{g}_i}$ are kept fixed through all the contingencies. By contrast, the adaptive weights, namely the tunable weights $\hat{W}_{\bar{f}_i}$ and $\hat{W}_{\bar{g}_i}$, are automatically adapted online in real time using tuning laws in (4,19) and (4,20), without manual intervention, in response to changes in system operating conditions.

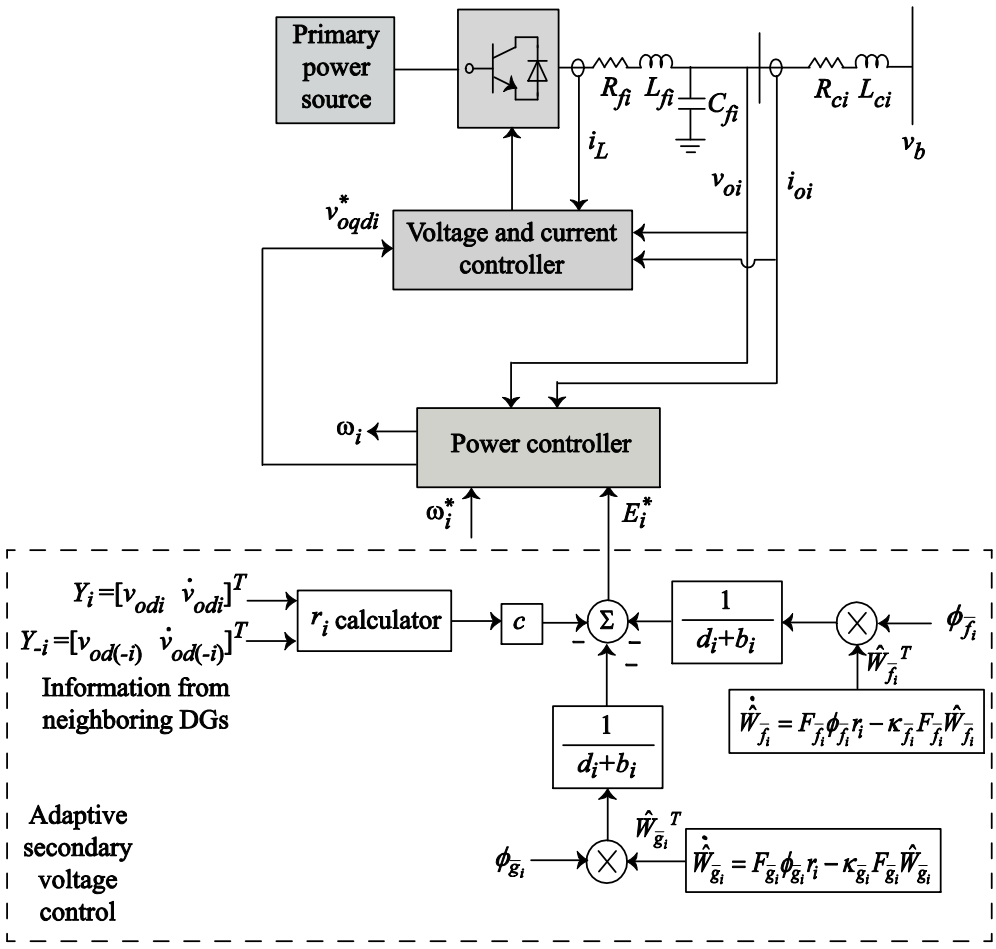

Figure 5-2 The Block Diagram of the Adaptive and Distributed Secondary Control

Remark 5.4. As seen in (4,18), the secondary control of a DG is a function of r_i, $\phi_{\bar{f}_i}$, and $\phi_{\bar{g}_i}$. r_i, the sliding mode error defined in (4,4), is a function of the output voltage magnitude of each DG and the output voltage magnitude of its neighbors on the communication digraph, and their first derivatives. $\phi_{\bar{f}_i}$, the basis functions used to compensate for the nonlinearities in $\bar{f}_i$ in (4,14), are functions of state variables of each DG. $\phi_{\bar{g}_i}$, the basis functions used to compensate

for the nonlinearities in $\bar{g}_i$ in (4,15), are functions of state variables of each DG and its neighbors on the communication digraph.

The block diagram of the adaptive and distributed secondary voltage control is shown in Figure 5-2. In this figure, $\phi_{\bar{f}_i}$ and $\phi_{\bar{g}_i}$ are the NN basis functions introduced in (4,16) and (4,17). The proposed control is fully independent of the DG parameters and the connector specifications. Therefore, the performance of the secondary control does not deteriorate by the change in DG parameters (e.g., due to aging or thermal effects.). Additionally, extensive studies are not required to tune the control parameters.

Simulation Results for the Adaptive and Distributed Secondary Voltage Control

The islanded microgrid shown in Figure 2-6 is used to verify the effectiveness of the proposed voltage control framework. The specifications of DGs, lines, and loads are summarized in Appendix B. Due to the adaptive nature of the proposed methodology, the specifications of DGs are not required for the controller implementation. However, these specifications are required to model DGs in the simulations and are summarized in Appendix B. In this Appendix, K_{PV}, K_{IV}, K_{PC}, and K_{IC} are the voltage and current controller parameters based on the detailed models discussed in Chapter 2. In the following, the simulation results are presented for four different cases. In the first three cases, a fixed communication topology is assumed, while the last case deals with a time-varying communication topology. In the first case, namely *Case 1*, the proposed secondary voltage control restores the DG voltage amplitude to the nominal voltage subsequent to the islanding process. In *Case 2*, the effectiveness of the adaptive voltage control subsequent to the changes in DG parameters is studied. *Case 3* deals with the voltage restoration subsequent to sudden load changes. The last case, namely *Case 4*, studies the proposed controller with a time-varying communication topology. For all cases, the NN tuning parameters are set to $F_{\bar{f}_i} = 10 \times I_{\bar{f}_i}$, $F_{\bar{g}_i} = 10 \times I_{\bar{g}_i}$ (I_N is an $N \times N$ identity matrix.), $\kappa_{\bar{f}_i} = 10$, and $\kappa_{\bar{g}_i} = 10$.

Case 1

In this case, it is assumed that the microgrid is islanded from the main grid at *t*=0, and the secondary control is applied at *t*=0.6 s. In practical applications, the voltage control should be applied immediately after the disturbance occurs. However, in this case, the secondary controller is intentionally delayed by 0.6 s to highlight its effectiveness. It is assumed that the DGs communicate with each other through the communication links depicted in Figure 5-3. DGs 1 and 2 have two communication ports: input and output ports. The associated adjacency matrix of the communication network in Figure 5-3 is

$$A_G = \begin{bmatrix} 0 & 0 & 0 & 0 \\ 1 & 0 & 0 & 0 \\ 0 & 1 & 0 & 0 \\ 1 & 0 & 0 & 0 \end{bmatrix}. \quad (4,33)$$

DG 1 is the only DG that is connected to the leader node with the pinning gain b_1=1. The coupling gain in (4,18) is c_i=4 which satisfies (4,21). λ_1 and λ_2 in (4,4) are chosen as $\lambda_1 = 10$ and $\lambda_2 = 1$.

Figure 5-4 shows the simulation results when the reference voltage value v_{ref} is set to 1 pu. As seen in Figure 5-4, while the primary control keeps the voltage stable, the secondary control returns all terminal voltage amplitudes to the pre-specified reference values in less than 0.6 seconds.

The secondary voltage control can be defined to control the voltage magnitude of the critical bus shown in Figure 2-6. In this case, v_{ref} is chosen according to (2,21), where $v_{c,mag}$ in (2,21) denotes the voltage magnitude of the critical bus. $v_{nominal}$ in (2,21) is set to 1 pu. k_{pc} and k_{ic} in (2,21) are set to 40 and 100, respectively. As seen in Figure 5-5, the secondary control returns the voltage magnitude of critical bus to $v_{nominal}$ in less than 1 second.

According to Remark 5.2, the control parameters c_i, λ_1, and λ_2, have a direct impact on the synchronization speed of the secondary voltage control. Figure 5-6 shows the simulation

results when $c_i = 40$, $\lambda_1 = 100$, and $\lambda_2 = 1$. As seen in this figure, the secondary control is applied at *t*=0.6 s, and returns all terminal voltage amplitudes to $v_{ref} = 1$ pu in less than 0.05 seconds.

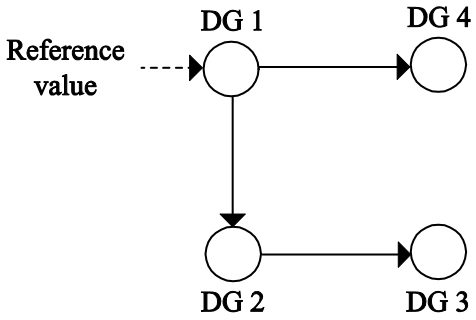

Figure 5-3 The Communication Digraph for *Case 1*, *Case 2, and Case 3*

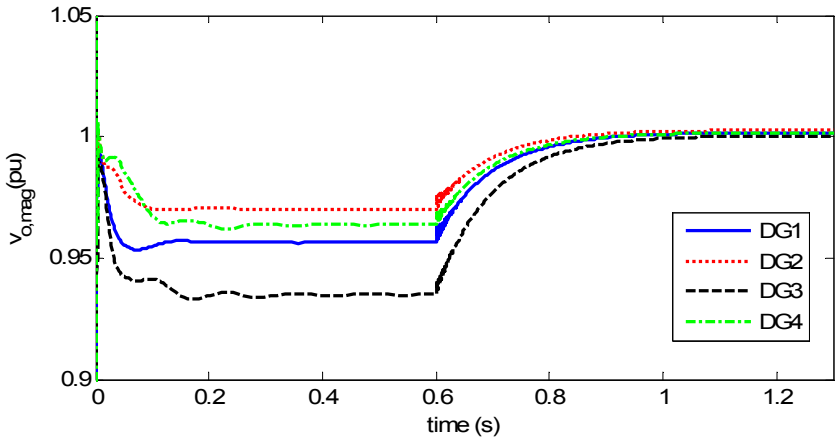

Figure 5-4 DG Output Voltage Magnitudes for *Case 1* when v_{ref}=1 pu

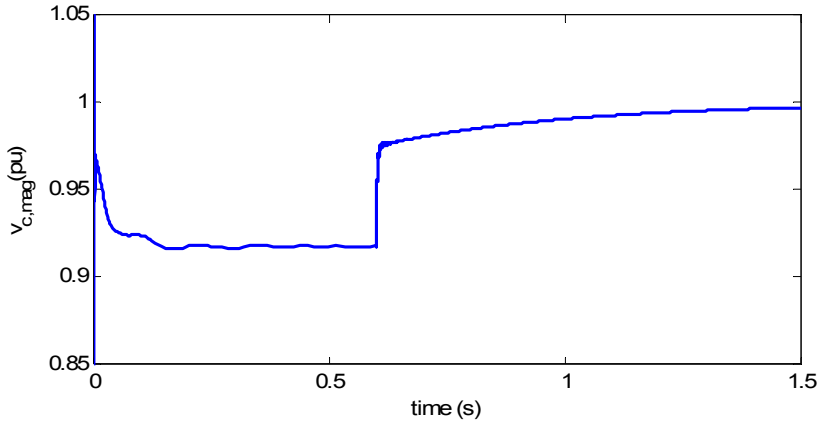

Figure 5-5 The Voltage Magnitude of Critical Bus for *Case 1*

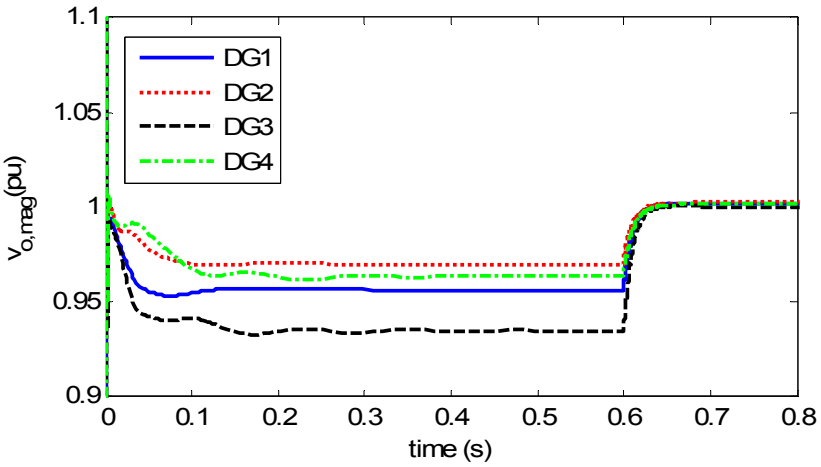

Figure 5-6 DG Output Voltage Magnitudes for *Case 1* when v_{ref}=1 pu, c_i=40, $\lambda_1 = 100$, and $\lambda_2 = 1$

Case 2

In this case, the performance of proposed distributed and adaptive voltage control is verified subsequent to the changes in DG parameters. It is assumed that the secondary voltage control is applied at *t*=0.6 s, and the resistance and inductance of the output connector of each DG, r_c and L_c, change from 0.03 Ω and 0.35 mH to 0.06 Ω and 0.7 mH at *t*=1 s. As seen in Figure 5-7, the performance of the adaptive voltage control does not deteriorate as a result of

the changes in r_c and L_c and the DG voltage magnitudes restoration to the nominal voltage is provided.

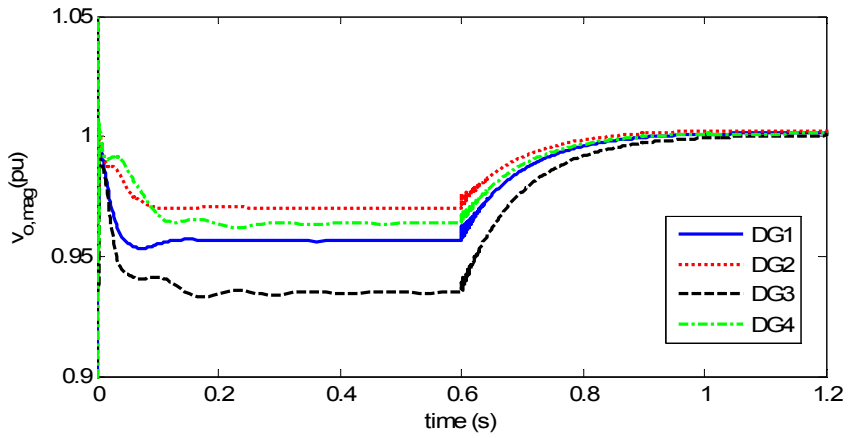

Figure 5-7 DG Output Voltage Magnitudes for *Case 2*

Case 3

Figure 5-8 shows the simulation results considering the load changes in an islanded microgrid. Initially, the secondary voltage control is applied at t=0.6 s. It is assumed that the initial resistance of Load 1 and 2 are 5 Ω, and the initial inductance of Load 1 and 2 are 16 mH. At *t*=1 s, Load 1 resistance and inductance change from 5 Ω and 16 mH to 3 Ω and 6.4 mH, respectively, and Load 2 resistance and inductance change from 5 Ω and 16 mH to 2 Ω and 3.2 mH, respectively. To show the effectiveness of the adaptive voltage control under load changes, it is assumed that the secondary voltage control is halted for 0.2 s. As seen in Figure 5-8, once the voltage control is stopped at *t*=1 s, the voltage magnitudes drop due to the sudden load changes. However, at *t*=1.2 s, the voltage control is applied again and returns the voltage magnitude of DGs to 1 pu, as seen in Figure 5-8. Therefore, the performance of the adaptive voltage control does not deteriorate as a result of the load changes and the adaptive voltage control effectively restores the output voltage magnitude of the DGs to the nominal voltage.

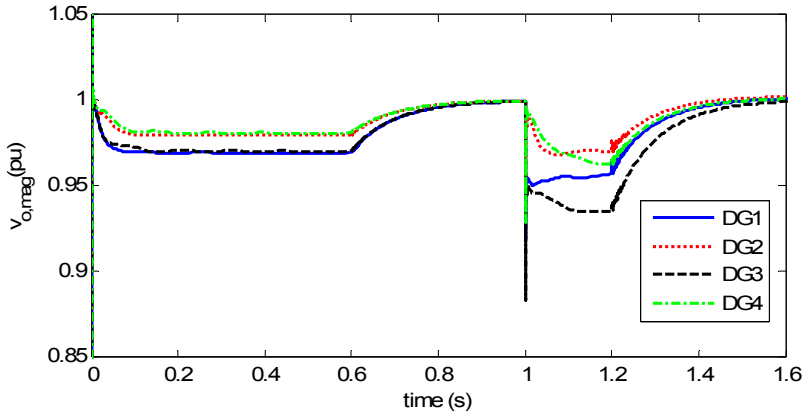

Figure 5-8 DG Output Voltage Magnitudes for *Case 3*

Case 4

In this case, it is assumed that the microgrid is islanded from the main grid at *t*=0, and the secondary control is applied at *t*=0.6 s (Similar to *Case 1*, the voltage control is applied after 0.6 s to highlight the effectiveness of the proposed voltage control.). However, as opposed to *Case 1*, the voltage controller is implemented through a time-varying communication network. Figure 5-9 shows the three communication network structures that are used in simulation. Each structure is adopted at a specific time interval. The communication digraph in Figure 5-9(a) models the communication network over the time interval [(0.6+0.15k) s, (0.6+0.15k)+0.05 s], for k=0,1,… . The communication digraph in Figure 5-9(b) models the communication network over the time interval [(0.65+0.15k) s, (0.65+0.15k)+0.05 s], for k=0,1,… The communication digraph in Figure 5-9(c) models the communication network over the time interval [(0.7+0.15k) s, (0.7+0.15k)+0.05 s], for k=0,1,…

DG 1 is the only DG that is connected to the leader node with the pinning gain b_1=1. The coupling gain in (4,18) is c_i=4 which satisfies (4,21). λ_1 and λ_2 in (4,4) are chosen as $\lambda_1 = 10$ and $\lambda_2 = 1$. Figure 5-10 shows the simulation results when the reference voltage value is set to 1 pu. As seen in Figure 5-10, the secondary control returns all terminal voltage

amplitudes to the pre-specified reference value in less than half a second. Compared with the simulation results of *Case 1*, Figure 5-10 shows that the proposed secondary control appropriately works with time varying communication networks.

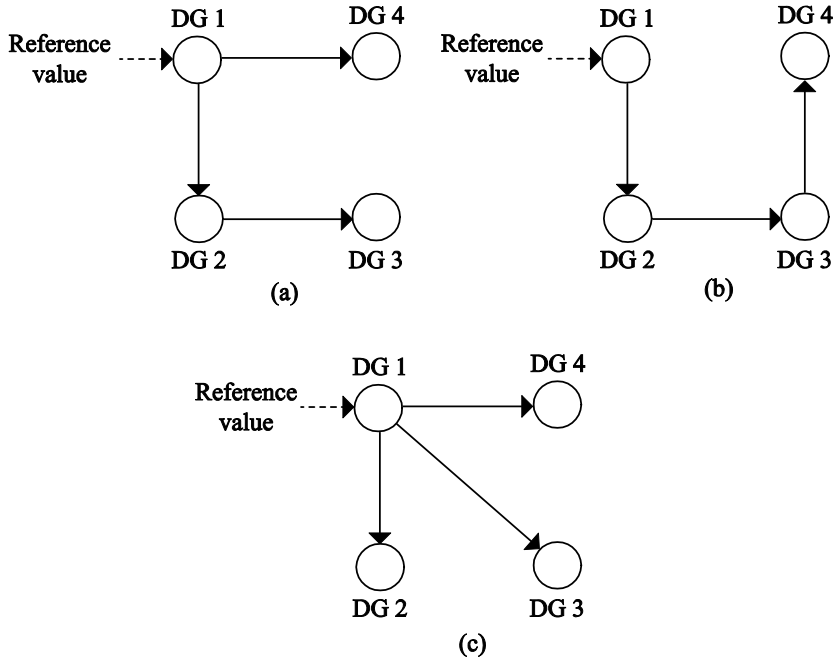

Figure 5-9 The Digraphs for Modeling the Time-Varying Communication Network of *Case 4*

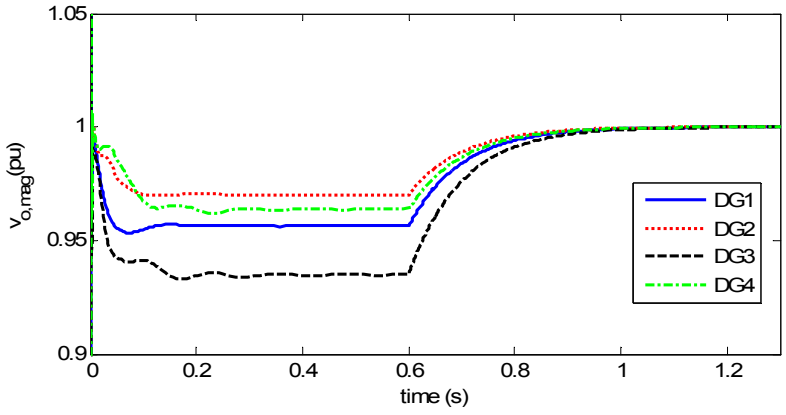

Figure 5-10 DG Output Voltage Magnitudes for *Case 4*

Conclusion

An adaptive and distributed secondary voltage control framework is presented. The proposed controller is independent of the DG parameters. Neural networks compensate for the uncertain/unknown DG dynamics, and facilitate the adaptive feature of this control. The Lyapunov technique is adopted to derive fully distributed control protocols for each DG. The simulation results verified the effectiveness of the proposed controller for several cases, including islanding, sudden load change, and variable communication network.

Chapter 6

Conclusions and Future Works

Contributions and Conclusions

In this dissertation, distributed cooperative control of multi-agent systems is exploited to design a distributed control structure for microgrid control. The main contributions of this dissertation are as follows:

- A straightforward solution is proposed to solve the tracking synchronization problem for nonlinear and heterogeneous multi-agent systems using input-output feedback linearization. Using feedback linearization, the nonlinear and heterogeneous dynamics of agents are transformed to identical linear dynamics and non-identical internal dynamics.
- The proposed solution is used to design a distributed secondary control structure. Input-output feedback linearization is used to transform the nonlinear dynamics of DGs to linear dynamics. Feedback linearization converts the secondary voltage control to a second-order tracker synchronization problem, and the secondary frequency control to a first-order tracking synchronization problem. As opposed to the conventional secondary controls with a centralized control structure, the distributed secondary control obviates the requirement for a central controller and requires only a sparse communication structure with one-way communication links which is cheaper and can be more reliable.
- Based on the distributed control of multi-agent systems, a two-layer and multi-objective control framework is proposed. The proposed control framework has two main layers. The first layer deals with the voltage and frequency control of VCVSIs. The second layer is to control the active and reactive power of CCVSIs.

- Neural networks are exploited to design a distributed and adaptive voltage control for microgrids. The proposed control is adaptive with respect to changes in the DG parameters and microgrid operating conditions.

The main conclusions of this dissertation are as follows:

- All of the proposed control schemes in this dissertation can accept both fixed and time-varying communication topologies. In the case of fixed communication networks, the communication topology must be a graph containing a spanning tree. In the case of time-varying communication networks, the communication topology must satisfy the sequential completeness condition. Optimal communication networks can be designed using operations research or assignment problem solutions. The optimization criteria can include minimal lengths of the communication links, maximal use of existing communication links, minimal number of links, and etc.
- The main drawback of conventional secondary control schemes with centralized structure is the single point of failure. The single point of failure means that the whole secondary control fails by the failure of the central control. The distributed control structure obviates this drawback and improves the reliability of the microgrid secondary control.
- Since the distributed control structure can be associated by time varying communication networks, they are more robust against communication link failures. If a communication link fails, the synchronization for all DGs is still provided if the sequential completeness condition is satisfied. However, in the centralized control structure, the failure of a communication link results in the loss of control system support for one DG.
- Voltage source inverters should be accommodated with a micro-processor to implement internal voltage and current control loops. This micro-processor is an inherent part of the voltage source inverter. The distributed control protocols on each DG do not require any additional micro-processor. They can be simply implemented on the pre-existing

micro-processor of each voltage source inverter. The distributed control protocols embedded on each DG would not require dedicated signal processing units and do not impose heavy processing burden on the existing micro-processor. They can be deployed on the existing processors, with a slight software update to pre-existing codes.

- The proposed control laws in this dissertation are associated with adjustable control parameters that can be used to tune the transient response of the secondary control. In Chapter 2, the ARE parameters in (2,37) can be changed appropriately to tune the transient response of the secondary voltage control. In Chapters 3 and 4, the coupling gains can be used to adjust the convergence speed of the proposed controllers. In Chapter 5, the coupling gain , λ_1 and λ_2 in (4,4), the adaptive weights, $\hat{W}_{\bar{f}_i}$ and $\hat{W}_{\bar{g}_i}$, and the fixed design constants, $F_{\bar{f}_i} \in R^{l_{\bar{f}_i} \times l_{\bar{f}_i}}$, $F_{\bar{g}_i} \in R^{l_{\bar{g}_i} \times l_{\bar{g}_i}}$, $\kappa_{\bar{f}_i}$, and $\kappa_{\bar{g}_i}$ in the tuning laws in (4,19) and (4,20),adjust the transient response of the secondary voltage control.

Future Works

Compared with the conventional control structures of microgrids, a different control structure was proposed in this dissertation. This structure exploits the distributed cooperative control of multi-agent systems. Based on this emerging control structure, future research works can focus on the following research trusts:

- The concept of distributed control can be also exploited in large scale power systems. Traditionally, these control levels are implemented through a centralized control structure. In the centralized control structure, a central controller provides the primary control references, solve optimal power flow, command globally on the gathered system-wide information, and require a complex, wide-bandwidth, and two-way communication network that adversely affect system flexibility, configurability, and reliability. Alternatively, a distributed control structure can be used to implement the

secondary and tertiary control levels. The distributed control structure can be implemented through a sparse communication network and does not require a central controller.

- In addition to voltage and frequency control, other control objectives can be handled through a distributed control structure. Mitigating the voltage unbalance in a microgrid is one of these control objectives. Distributed control structures can be proposed to control the voltage and frequency of microgrids and share the active and reactive power among DGs in the presence of nonlinear loads.
- Due to the presence of sensitive loads and high energy demand loads such as pulse loads, the voltage and frequency control of shipboard power system is of particular importance. Subsequent to the sudden load changes or faults, the voltage and frequency may deviate from their nominal values. The electric ship contains some critical loads that are required to work at the nominal voltage and frequency. Distributed control schemes can be used to control the voltage of critical loads and restore the frequency of the shipboard power system.

Appendix A

The Effects of the Algebraic Riccati Equation Parameters on the Synchronization Speed of the Secondary Voltage Control

The Algebraic Riccati Equation (ARE) parameters have a direct impact on the transient response of the proposed secondary voltage control. The ARE in (2,37) is extracted by minimizing the following performance index for each DG [96]

$$J_i = \frac{1}{2}\int_0^{\infty} (\boldsymbol{\delta}_i^T Q \boldsymbol{\delta}_i + v_i^T R v_i) dt, \tag{A,1}$$

where the local disagreement vector is

$$\boldsymbol{\delta}_i = \mathbf{y}_i - \mathbf{y}_0. \tag{A,2}$$

The performance index J_i can be interpreted as an energy function and the controller is designed to make it as small as possible. The ARE parameters Q and R directly influence the transient response of the controller. Generally speaking, a largermeans that $\boldsymbol{\delta}_i$ is kept smaller by the controller for keeping J_i small. On the other hand, a larger R means that $v_i(t)$ is kept smaller by the controller for keeping J_i small. Therefore, larger Q or smaller R generally result in the poles of the closed-loop system matrix to move left in the s-plane so that the system response speed increases.

Appendix B

The Specifications of the Microgrid Test System in Figure 2-6

The specifications of the DGs, lines, and loads are summarized in Table B-1.

Table B-1 Specifications of the Microgrid Test System in Figure 2-6

DGs	DG 1 & 2 (9 kVA rating)			DG 3 & 4 (7 kVA rating)		
	m_P	9.4×10^{-5}		m_P	12.5×10^{-5}	
	n_Q	1.3×10^{-3}		n_Q	1.5×10^{-3}	
	R_c	0.03 Ω		R_c	0.03 Ω	
	L_c	0.35 mH		L_c	0.35 mH	
	R_f	0.1 Ω		R_f	0.1 Ω	
	L_f	1.35 mH		L_f	1.35 mH	
	C_f	50 μF		C_f	50 μF	
	K_{PV}	0.1		K_{PV}	0.05	
	K_{IV}	420		K_{IV}	390	
	K_{PC}	15		K_{PC}	10.5	
	K_{IC}	20000		K_{IC}	16000	
Lines	Line 1		Line 2		Line 3	
	R_{l1}	0.23 Ω	R_{l2}	0.35 Ω	R_{l3}	0.23 Ω
	L_{l1}	318 μH	L_{l2}	1847 μH	L_{l3}	318 μH
Loads	Load 1			Load 2		
	R (per phase)	3 Ω		R (per phase)	2 Ω	
	X (per phase)	2 Ω		X (per phase)	1 Ω	

Appendix C

The Effect of the Controller Gain on the Convergence Speed in a Tracking Synchronization Problem

Consider N nonlinear and heterogeneous systems or agents that are distributed on a communication graph Gr with the node dynamics

$$\begin{cases} \dot{\mathbf{x}}_i = \mathbf{f}_i(\mathbf{x}_i) + \mathbf{g}_i(\mathbf{x}_i)u_i, \\ y_i = h_i(\mathbf{x}_i) + d_i u_i, \end{cases} \tag{C,1}$$

where $\mathbf{x}_i(t) \in \mathbb{R}^{n_i}$ is the state vector, $u_i(t) \in R$ is the control input, $y_i(t) \in R$ is the output of i^{th} node, and $\mathbf{f}_i$, $\mathbf{g}_i$, and h_i are smooth functions. It is assumed that $\mathbf{f}_i(\bullet) : R^{n_i} \to R^{n_i}$ is locally Lipschitz in R^{n_i} and $\mathbf{f}_i(0) = 0$. d_i is the direct feed term in the output. The agent state dynamics and state dimensions n_i do not need to be the same.

In the tracking synchronization problem, it is desired to design distributed control inputs $u_i(t)$ to synchronize the output of all nodes to the output of a leader node $y_0(t)$. The leader node can be viewed as a command generator that generates the desired trajectory

$$\begin{cases} \dot{\mathbf{x}}_0 = \mathbf{f}_0(\mathbf{x}_0) \\ y_0 = h_0(x_0) \end{cases}. \tag{C,2}$$

The functions $\mathbf{f}_0$ and h_0 are assumed to be of class C^∞. Outputs $y_i(t)$ are performance outputs required to track the leader's output. It is assumed that all of the agent states are measurable. In general, observers can be added if output measurements are available.

As seen in (C,1), the output $y_i(t)$ is related to the input $u_i(t)$ by the nonlinear function $h_i(x_i)$ and d_i. The difficulties associated with the nonlinear nature of the dynamics can be overcome by using the following procedure.

Differentiate the output of each agent in (C,1) to obtain

$$\dot{y}_i = L_{\mathbf{f}_i} h_i + L_{\mathbf{g}_i} h_i u_i + d_i \dot{u}_i, \tag{C,3}$$

where $L_{\mathbf{f}} h = \dfrac{\partial h}{\partial \mathbf{x}} \mathbf{f}(\mathbf{x})$ denotes Lie derivative. Define the auxiliary control v_i as

$$v_i = L_{\mathbf{f}_i} h_i + L_{\mathbf{g}_i} h_i u_i + d_i \dot{u}_i. \tag{C,4}$$

Then, the control input u_i satisfies the nonlinear state variable equation

$$d_i \dot{u}_i = -L_{\mathbf{g}_i} h_i u_i - L_{\mathbf{f}_i} h_i + v_i \,. \qquad \text{(C,5)}$$

Equation (C,5) allows direct computation of the control input u_i in terms of v_i. The auxiliary control v_i is specified in Theorem C.1. It is noted that the state-space equation (C,5) guarantees that the control input u_i is differentiable.

Equation (C,4) defines the input-output feedback linearization that results in the first-order linear systems

$$\dot{y}_i = v_i, \forall i \,. \qquad \text{(C,6)}$$

Using this input-output feedback linearization, the dynamics of each agent are decomposed into the first order dynamical system in (C,6) and a set of internal dynamics

$$\dot{\mu}_i = W_i(y_i, \mu_i), \forall i \,, \qquad \text{(C,7)}$$

where $\mu_i \in R^{n_i}$ represents the internal dynamics.

To solve the synchronization problem for the systems in (C,6), cooperative team objectives can be expressed in terms of the *local neighborhood tracking error*

$$e_i = \sum_{j \in N_i} a_{ij}(y_i - y_j) + b_i(y_i - y_0) \,. \qquad \text{(C,8)}$$

The pinning gain $b_i \geq 0$ is nonzero only for the nodes that are directly connected to the leader node. It is assumed that b_i is nonzero for at least one node. The nodes for which $b_i \neq 0$ are referred to as the pinned or controlled nodes.

From (C,8), the global neighborhood error vector for the graph Gr is written as

$$e = (L + B)\left(y - \underline{y}_0\right) \equiv (L + B)\delta, \qquad \text{(C,9)}$$

where the global variables are defined as

$y = \begin{bmatrix} y_1 & y_2 & \cdots & y_N \end{bmatrix}^T \in R^N$, $e = \begin{bmatrix} e_1 & e_2 & \cdots & e_N \end{bmatrix}^T \in R^N$, and $\underline{y}_0 = \mathbf{1}_N \otimes y_0 \in R^N$, with $\mathbf{1}_N$ the vector of ones with the length of N. $B \in R^{N \times N}$ is a diagonal matrix with diagonal entries equal to the pinning gains b_i. The *global disagreement vector* is δ.

Assumption C.1. The vector $\dot{\underline{y}}_0 = \mathbf{1}_N \otimes \dot{y}_0$ is bounded so that $\left\| \dot{\underline{y}}_0 \right\| \le Y_M$, for some finite bound Y_M that is generally unknown.

Theorem C.1. Let the digraph Gr have a spanning tree and $b_i \neq 0$ for at least one root node. Assume that the zero dynamics of each node $\dot{\mu}_i = W_i(0, \mu_i), \forall i$ are asymptotically stable. Let the auxiliary control v_i in (C,5) be chosen as

$$v_i = -ce_i, \tag{C,10}$$

where the scalar $c > 0$ and e_i is in (C,8). Then, the global neighborhood error e in (C,9) is UUB with the practical bound in (C,17). Moreover, the agent outputs $y_i(t)$ are cooperative UUB with respect to the leader node output $y_0(t)$ in (C,2) and all nodes synchronize to $y_0(t)$.

Proof: From (C,10), the global input vector v is

$$v = \begin{bmatrix} v_1 & v_2 & \cdots & v_N \end{bmatrix}^T = -ce. \tag{C,11}$$

Consider the Lyapunov function candidate

$$V = \frac{1}{2} e^T P e, \text{ where } P = diag\left\{ 1 \middle/ w_i \right\}, \tag{C,12}$$

where w_i are the elements of a vector w that satisfies $(L+B)w = \mathbf{1}_N$. Since the digraph Gr has a spanning tree and $k_i \neq 0$ for at least one root node, $L+B$ is nonsingular and a unique solution exists for w [82].

Differentiating (C,12) and using (C,9) yield

$$\dot{V} = e^T P(L+B)(\dot{y} - \dot{\underline{y}}_0) = e^T P(L+B)(v - \dot{\underline{y}}_0). \tag{C,13}$$

Defining $A \equiv L + B$, and placing (C,11) into (C,13) yields

$$\dot{V} = \frac{-c}{2} e^T (PA + A^T P) e - e^T PA \dot{y}_0. \tag{C,14}$$

From [82] $Q \equiv PA + A^T P$ is positive definite. Therefore, $\frac{c}{2} e^T Q e \geq \frac{c}{2} \underline{\sigma}(Q) \|e\|^2$, and hence

$$\frac{-c}{2} e^T Q e \leq \frac{-c}{2} \underline{\sigma}(Q) \|e\|^2, \tag{C,15}$$

where $\underline{\sigma}(\cdot)$ is the minimum singular value of a matrix. According to (C,15) and Assumption C.1

$$\dot{V} \leq \frac{-c}{2} \underline{\sigma}(Q) \|e\|^2 + \|e\| \overline{\sigma}(P) \overline{\sigma}(A) Y_M, \tag{C,16}$$

where $\overline{\sigma}(\cdot)$ is the maximum singular value of a matrix. $\dot{V} \leq 0$ if

$$\|e\| \geq \frac{\overline{\sigma}(P) \overline{\sigma}(A) Y_M}{\frac{c}{2} \underline{\sigma}(Q)}. \tag{C,17}$$

Equation (C,17) shows that the derivative of Lyapunov function in (C,16) is negative outside a compact set around origin with the radius of $\overline{\sigma}(P) \overline{\sigma}(A) Y_M \Big/ \frac{c}{2} \underline{\sigma}(Q)$. This demonstrates that any trajectory of $e(t)$ beginning in this compact set evolves completely within this compact set. Therefore, according to the standard Lyapunov theorem extension, $e(t)$ is UUB. According to (C,9), if the graph has a spanning tree then $L+B$ is nonsingular and $\|\delta\| \leq \|e\| / \underline{\sigma}(L + B)$. Therefore the global disagreement vector δ is UUB and, hence, $y_i(t)$ are cooperative UUB with respect to $y_0(t)$. If the zero dynamics $\dot{\mu}_i = W_i(0, \mu_i), \forall i$ are asymptotically stable, then (C,6) and (C,10) are asymptotically stable. This completes the proof. □

Remark C.1. Supposed that $Y_M = 0$, equation (C,16) yields

$$\dot{V} \leq \frac{-c}{2} \underline{\sigma}(Q) \|e\|^2 \leq \frac{-c}{2} \frac{\underline{\sigma}(Q)}{\overline{\sigma}(P)} V \equiv -2\alpha V, \tag{C,18}$$

From (C,18), one can write

$$V(t) \leq e^{-2\alpha t} V(t_0). \tag{C,19}$$

From (C,12) and (C,19)

$$\frac{1}{2}\underline{\sigma}(P)\left\|e(t)\right\|^2 \le \frac{1}{2}\bar{\sigma}(P)e^{-2\alpha t}\left\|e(t_0)\right\|^2, \qquad \text{(C,20)}$$

or equivalently

$$\left\|e(t)\right\| \le \sqrt{\frac{\bar{\sigma}(P)}{\underline{\sigma}(P)}}e^{-\alpha t}\left\|e(t_0)\right\|. \qquad \text{(C,21)}$$

Equation (C,21) shows that the global neighborhood error $e(t)$ goes to zero with the time constant $1/\alpha$. Since $\alpha = \frac{-c}{2}\frac{\underline{\sigma}(Q)}{\bar{\sigma}(P)}$, the synchronization speed of the system can be adjusted by c.

Appendix D

The Specifications of the Microgrid Test System in Figure 4-8

The specifications of the DGs, lines, and loads are summarized in Tables D-1, D-2, and D-3.

Table D-1 Specifications of DGs for Microgrid Test System in Figure 4-8

	DG 1 & 3		DG 2	
VCVSIs	m_P	18.8×10^{-5}	m_P	25×10^{-5}
	n_Q	2.6×10^{-3}	n_Q	3×10^{-3}
	R_c	0.03 Ω	R_c	0.03 Ω
	L_c	0.35 mH	L_c	0.35 mH
	R_f	0.1 Ω	R_f	0.1 Ω
	L_f	1.35 mH	L_f	1.35 mH
	C_f	50 μF	C_f	50 μF
	K_{PV}	0.1	K_{PV}	0.05
	K_{IV}	420	K_{IV}	390
	K_{PC}	15	K_{PC}	10.5
	K_{IC}	20000	K_{IC}	16000
CCVSIs	DG 4 & 5		DG 6 & 7	
	R_f	0.23 Ω	R_f	0.35 Ω
	L_f	318 μH	L_f	1847 μH
	K_{PC}	10.5	K_{PC}	10.5
	K_{IC}	16000	K_{IC}	16000
	P_{max}	1500 W	P_{max}	2000 W
	Q_{max}	1000 W	Q_{max}	1200 W

Table D-2 Specifications of Lines for Microgrid Test System in Figure 4-8

Line 1, 3, 5, 7		Line 2, 4, 6	
R_{line}	0.23 Ω	R_{line}	0.35 Ω
L_{line}	318 μH	L_{line}	1847 μH

Table D-3 Specifications of Loads for Microgrid Test System in Figure 4-8

	Load 1	Load 2	Load 3	Load 4
R (per phase)	30 Ω	20 Ω	25 Ω	25 Ω
X (per phase)	15 Ω	10 Ω	10 Ω	15 Ω

Appendix E

The Specifications of the IEEE 34 Bus Test Feeder

The specifications of the DGs and loads are summarized in Tables E-1 and E-2.

Table E-1 Specifications of DGs for IEEE 34 Bus Test Feeder

	DG 1 & 2		DG 3	
VCVSIs	m_P	5.64×10^{-5}	m_P	7.5×10^{-5}
	n_Q	5.2×10^{-4}	n_Q	6×10^{-4}
	R_c	0.03 Ω	R_c	0.03 Ω
	L_c	0.35 mH	L_c	0.35 mH
	R_f	0.1 Ω	R_f	0.1 Ω
	L_f	1.35 mH	L_f	1.35 mH
	C_f	50 µF	C_f	50 µF
	K_{PV}	0.1	K_{PV}	0.05
	K_{IV}	420	K_{IV}	390
	K_{PC}	15	K_{PC}	10.5
	K_{IC}	20000	K_{IC}	16000
CCVSIs	DG 4 & 5		DG 6	
	R_f	0.2 Ω	R_f	0.35 Ω
	L_f	340 µH	L_f	1900 µH
	K_{PC}	11	K_{PC}	11
	K_{IC}	16000	K_{IC}	16000
	P_{max}	35 kW	P_{max}	30 kW
	Q_{max}	32 kVAr	Q_{max}	30 kVAr

Table E-2 Specifications of Loads for IEEE 34 Bus Test Feeder

	Load 1	Load 2	Load 3	Load 4
R (per phase)	30 Ω	20 Ω	25 Ω	25 Ω
X (per phase)	15 Ω	10 Ω	10 Ω	15 Ω

References

[1] G. A. Pagani and M. Aiello, “Towards decentralization: A topological investigation of the medium and low voltage grids,” *IEEE Trans. Smart Grid*, vol. 2, pp. 538-547, Sept. 2011.

[2] T. L. Vandoorn, B. Renders, L. Degroote, B. Meersman, and L. Vandevelde, “Active load control in islanded microgrids based on the grid voltage,” *IEEE Trans. Smart Grid,* vol. 2, pp. 139-151, Mar. 2011.

[3] Q. Yang, J. A. Barria, and T. C. Green, “Advanced power electronic conversion and control system for universal and flexible power management,”*IEEE Trans. Smart Grid,* vol. 2, pp. 231-243, June 2011.

[4] B. Fahimi, A. Kwasinski, A. Davoudi, R. S. Balog, and M. Kiani, “Charge it,” *IEEE Power & Energy Magazine,* vol. 9, pp. 54-64, July/Aug. 2011.

[5] M. E. Elkhatib, R. El-Shatshat, and M. M. A. Salama, “Novel coordinated voltage control for smart distributed networks with DG,”*IEEE Trans. Smart Grid,* vol. 2, pp. 598-605, Dec. 2011.

[6] “The smart grid: An introduction,” United States Department of Energy, Office of Electricity Delivery and Energy Reliability. Washington, DC, 2008. [Online]. Available: http://www.oe.energy.gov/1165.htm.

[7] R. H. Lasseter, “Microgrid,” in *Proc*. *IEEE Power Eng. Soc. Winter Meeting*, vol. 1, New York, 2002, pp. 305-308.

[8] F. Katiraei, R. Iravani, N. Hatziargyriou, and A. Dimeas, “Microgrids management,” *IEEE Power & Energy Magazine,* vol. 6, pp. 54-65, May/June 2008.

[9] N. Hatziargyriou, H. Asano, R. Iravani, and C. Marnay, “Microgrids,” *IEEE Power & Energy Magazine,* vol. 5, pp. 78-94, July/Aug. 2007.

[10] P. Piagi and R. H. Lasseter, “Industrial applications of microgrids,” Power System Engineering Research Center, Univ. Wisconsin, Madison, WI, 2001.

[11] J. Driesen and F. Katiraei, “Design for distributed energy resources,” *IEEE Power & Energy Magazine,* vol. 6, pp. 30-40, May/June 2008.

[12] J. M. Guerrero, J. C. Vásquez, J. Matas, M. Castilla, L. G. d. Vicuña, and M. Castilla, “Hierarchical control of droop-controlled AC and DC microgrids-A general approach toward standardization,” *IEEE Trans. Ind. Electron.,* vol. 58, pp. 158-172, Jan. 2011.

[13] A. Mehrizi-Sani and R. Iravani, “Potential-function based control of a microgrid in islanded and grid-connected models,” *IEEE Trans. Power Syst.,* vol. 25, pp. 1883-1891, Nov. 2010.

[14] C. Yuen, A. Oudalov, and A. Timbus, “The provision of frequency control reserves from multiple microgrids,” *IEEE Trans. Ind. Electron.,* vol. 58, pp. 173-183, Jan. 2011.

[15] K. D. Brabandere, K. Vanthournout, J. Driesen, G. Deconinck, and R. Belmans, “Control of microgrids,” in *Proc.IEEE Power & Energy Society General Meeting*, 2007, pp. 1-7.

[16] Y. A. R. I. Mohamed and A. A. Radwan, “Hierarchical control system for robust microgrid operation and seamless mode transfer in active distribution systems,” *IEEE Trans. Smart Grid,* vol. 2, pp. 352-362, June 2011.

[17] J. A. P. Lopes, C. L. Moreira, and A. G. Madureira, “Defining control strategies for microgrids islanded operation,” *IEEE Trans. Power Syst.,* vol. 21, pp. 916-924, May 2006.

[18] P. Piagi and R. H. Lasseter, “Autonomous control of microgrids,” in *Proc*. *IEEE Power Eng. Soc. General Meeting*, 2006.

[19] F. Katiraei, M. R. Iravani, and P. W. Lehn, “Microgrid autonomous operation during and subsequent to islanding process,” *IEEE Trans. Power Del.,* vol. 20, pp. 248-257, Jan. 2005.

[20] Y. Li, D. M. Vilathgamuwa, and P. C. Loh, “Design, analysis, and real-time testing of a controller for multibus microgrid system,” *IEEE Trans. Power Electron.,* vol. 19, pp. 1195-1204, Sept. 2004.

[21] H. Nikkhajoei and R. H. Lasseter, “Distributed generation interface to the CERTS microgrid,” *IEEE Trans. Power Del.,* vol. 24, pp. 1598-1608, July 2009.

[22] M. C. Chandorkar, D. M. Divan, and R. Adapa, “Control of parallel connected inverters in standalone AC supply systems,” *IEEE Trans. Ind. Appl.,* vol. 29, pp. 136-143, Jan/Feb 1993.

[23] H. Karimi, H. Nikkhajoei, and M. R. Iravani, “Control of an electronically-coupled distributed resource unitsubsequent to an islanding event,” *IEEE Trans. Power Del.,* vol. 23, pp. 493-501, Jan. 2008.

[24] M. D. Ilic and S. X. Liu, *Hierarchical power systems control: Its value in a changing industry*. London, U.K.: Springer, 1996.

[25] M. J. Ryan, W. E. Brumsickle, and R. D. Lorenz, “Control topology options for single-phase UPS inverters,” *IEEE Trans. Ind. Appl.,* vol. 33, pp. 493-501, Mar./Apr. 1997.

[26] G. Escobar, P. Mattavelli, A. M. Stankovic, A. A. Valdez, and J. L. Ramos, “An adaptive control for UPS to compensate unbalance and harmonic distortion using a combined capacitor/load current sensing,” *IEEE Trans. Ind. Appl.,* vol. 54, pp. 839-847, Apr. 2007.

[27] A. Hasanzadeh, O. C. Onar, H. Mokhtari, and A. Khaligh, “A proportional-resonant controller-based wireless control strategy with a reduced number of sensors for parallel-operated UPSs,” *IEEE Trans. Power Del.,* vol. 25, pp. 468-478, Jan. 2010.

[28] M. Prodanović and T. C. Green, “High-quality power generation through distributed control of a power park microgrid,” *IEEE Trans. Ind. Electron.,* vol. 53, pp. 1471-1482, October 2006.

[29] Y. W. Li, D. M. Vilathgamuwa, and P. C. Loh, “Robust control method for a microgrid with PFC capacitor connected,” *IEEE Trans. Ind. Appl.,* vol. 43, pp. 1172-1182, Sept./Oct. 2007.

[30] Y. W. Li, D. M. Vilathgamuwa, and P. C. Loh, “A grid-interfacing power quality compensator for three-phase three-wire microgrid applications,” *IEEE Trans. Power Electron.,* vol. 21, pp. 1021-1031, July 2006.

[31] J. M. Guerrero, L. Hang, and J. Uceda, “Control of distributed uninterruptible power supply systems,” *IEEE Trans. Ind. Electron.,* vol. 55, pp. 2845-2859, Aug. 2008.

[32] T. Iwade, S. Komiyama, and Y. Tanimura, “A novel small-scale UPS using a parallel redundant operation system,” in *Proc*. *International Telecommunications Energy Conf.*, 2003, pp. 480-483.

[33] Y. J. Cheng and E. K. K. Sng, “A novel communication strategy for decentralized control of paralleled multi-inverter systems,” *IEEE Trans. Power Electron.,* vol. 21, pp. 148-156, Jan. 2006.

[34] X. Sun, Y. S. Lee, and D. Xu, “Modeling, analysis, and implementation of parallel multi-converter system with instantaneous average-current-sharing method,” *IEEE Trans. Power Electron.,* vol. 18, pp. 844-856, May 2003.

[35] S. Sun, L. K. Wong, Y. S. Lee, and D. Xu, “Design and analysis of an optimal controller for parallel multi-inverter systems,” *IEEE Trans. Circuit and Syst. II,* vol. 52, pp. 56-61, Jan. 2006.

[36] T. F. Wu, U. K. Chen, and Y. H. Huang, “3C strategy for inverters in parallel operation achieving an equal current distribution,” *IEEE Trans. Ind. Electron.,* vol. 47, pp. 273-281, Apr. 2000.

[37] C. Mark and L. Bolster, “Bus-tie synchronization and load share technique in a ring bus system with multiple power inverters,” in *Proc*. *IEEE Applied Power Electron. Conf.,* APEC*,* 2005, pp. 871-874.

[38] J. M. Guerrero, J. C. Vásquez, J. Matas, M. Castilla, and L. G. D. Vicuña, “Control strategy for flexible microgrid based on parallel line-interactive UPS systems,” *IEEE Trans. Ind. Electron.,* vol. 56, pp. 726-736, Mar. 2009.

[39] J. M. Guerrero, J. Matas, L. G. d. Vicuna, M. Castilla, and J. Miret, “Wireless-control strategy for parallel operation of distributed generation inverters,” *IEEE Trans. Ind. Electron.,* vol. 53, pp. 1461-1470, Oct. 2006.

[40] J. M. Guerrero, J. Matas, L. G. D. Vicuna, M. Castilla, and J. Miret, “Decentralized control for parallel operation of distributed generation inverters using resistive output impedance,” *IEEE Trans. Ind. Electron.,* vol. 54, pp. 994-1004, Apr. 2007.

[41] J. M. Guerrero, L. G. D.Vicuna, J. Matas, M. Castilla, and J. Miret, “Output impedance design of parallel-connected UPS inverters with wireless load-sharing control,” *IEEE Trans. Ind. Electron.,* vol. 52, pp. 1126-1135, Aug. 2005.

[42] J. M. Guerrero, L. G. d. Vicuna, J. Miret, J. Matas, and J. Cruz, “Output impedance performance for parallel operation of UPS inverters using wireless and average current-sharing controllers,” in *Proc*. *Power Electron. Specialist Conf.*, 2004, pp. 2482-2488.

[43] F. Katiraei and M. R. Iravani, “Power management strategies for a microgrid with multiple distributed generation units,” *IEEE Trans. Power Syst.,* vol. 21, pp.1821-1831, Jan. 2005.

[44] I. Y. Chung, W. Liu, D. A. Cartes, and K. Schoder, “Control parameter optimization for a microgrid system using particle swarm optimization,” in *Proc*. *IEEE International Conf. on Sustainable Energy Technologies*, 2008, pp. 837 - 842.

[45] E. Rokrok and M. E. H. Golshan, “Adaptive voltage droop method for voltage source inverters in an islanded multibus microgrid,” *IET Gen., Trans., and Dist.,* vol. 4, no. 5, pp. 562-578, 2010.

[46] G. Diaz, C. Gonzalez-Moran, J. Gomez-Aleixandre, and A. Diez, “Scheduling of droop coefficients for frequency and voltage regulation in isolated microgrids,” *IEEE Trans. Power Syst.,* vol. 25, pp. 489-496, Feb. 2010.

[47] C. K. Sao and W. Lehn, “Autonomous load sharing of voltage source inverters,” *IEEE Trans. Power Del.,* vol. 20, pp. 1009-1016, Apr. 2005.

[48] C. K. Sao and W. Lehn, “Control and power management of converter fed microgrids,” *IEEE Trans. Power Syst.,* vol. 23, pp. 1088-1098, Aug. 2008.

[49] M. N. Marwali, J. W. Jung, and A. Keyhani, “Control of distributed generation systems-part II: Load sharing control,” *IEEE Trans. Power. Electron.,* vol. 19, pp. 1551-1561, Nov. 2004.

[50] U. Borup, F. Blaabjerg, and P. N. Enjeti, “Sharing of nonlinear load in parallel-connected three-phase converters,” *IEEE Trans. Ind. Appl.,* vol. 37, pp. 1817-1823, Nov./Dec. 2001.

[51] T. L. Lee and P. T. Cheng, “Design of a new cooperative harmonic filtering strategy for distributed generation interface converters in an islanding network,” *IEEE Trans. Power. Electron.,* vol. 22, pp. 1919-1927, Sept. 2007.

[52] Q. C. Zhong, “Harmonic droop controller to reduce the voltage harmonics of inverters,” *IEEE Trans. Ind. Electron.,* vol. 60, pp. 936-945, March 2013.

[53] J. C. Vasquez, J. M. Guerrero, A. Luna, P. Rodriguez, and R. Teodorescu, “Adaptive droop control applied to voltage-source inverters operating in grid-connected and islanded modes,” *IEEE Trans. Ind. Electron.,* vol. 56, pp. 4088-4096, Oct. 2009.

[54] K. D. Brabandere, B**.** Bolsens , J. V. D. Keybus, A. Woyte, J. Driesen, and R. Belmans, “A voltage and frequency droop control method for parallel inverters,” *IEEE Trans. Power Electron.,* vol. 22, pp. 1107-1115, July 2007.

[55] Z. Jiang and X. Yu, “Active power-voltage control method for islanding operation of inverter-interfaced microgrids,” in*Proc.IEEE Power & Energy Society General Meeting*, 2009, pp. 1 - 7.

[56] Y. Li and Y. W. Li, “Decoupled power control for an inverter based low voltage microgrid in autonomous operation,” in *Proc*. *IEEE 6th International Power Electron. and Motion Control Conf.*, 2009, pp. 2490 - 2496.

[57] Y. Li and Y. W. Li, “Virtual frequency-voltage frame control of inverter based low voltage microgrid,” in *Proc*. *IEEE Electrical Power & Energy Conf.*, 2009, pp. 1 - 6.

[58] Y. Li and Y. W. Li, “Power management of inverter interfaced autonomous microgrid based on virtual frequency-voltage frame,” *IEEE Trans. Smart Grid,* vol. 2, pp. 30-40, Mar. 2011.

[59] W. Yao, M. Chen, J. Matas, J. M. Guerrero, and Z. Qian, “Design and analysis of the droop control method for parallel inverters considering the impact of the complex impedance on the power sharing,” *IEEE Trans. Ind. Electron.,* vol. 58, pp. 576-588, Feb. 2011.

[60] M. Savaghebi, A. Jalilian, J. Vasquez, and J. Guerrero, “Autonomous voltage unbalance compensation in an islanded droop-controlled microgrid,” *IEEE Trans. Ind. Electron.,* vol. 60, pp. 1390-1402, April 2013.

[61] A. Tuladhar, H. Jin, T. Unger, and K. Mauch, “Control of parallel inverters in distributed AC power systems with consideration of line impedance effect,” *IEEE Trans. Ind. Appl.,* vol. 36, pp. 131-138, Jan./Feb. 2000.

[62] A. Tuladhar, H. Jin, T. Unger, and K. Mauch, “Parallel operation of single phase inverter modules with no control interconnections,” in *Proc. Applied Power Electron. Conf. and Exposition*, APEC, 1997, pp. 94-100.

[63] B. Marinescu and H. Bourles, “Robust predictive control for the flexible coordinated secondary voltage control of large scale power system,” *IEEE Trans. Power Syst.,* vol. 14, pp. 1262-1268, Nov. 1999.

[64] D. Yazdani, A. Bakhshai, G. Joos, and M. Mojiri, “A nonlinear adaptive synchronization technique for grid-connected distributed energy sources,” *IEEE Trans. Power Electron.,* vol. 23, pp. 2181-2186, July 2008.

[65] B. P. McGrath, D. G. Holmes, and J. J. H. Galloway, “Power converter line synchronization using a discrete fourier transform (DFT) based ona variable sample rate,” *IEEE Trans. Power Electron,* vol. 20, pp. 877-884, July 2005.

[66] S. J. Lee, H. Kim, S. K. Sul, and F. Blaabjerg, “A novel control algorithm for static series compensators by use of PQR instantaneous power theory,” *IEEE Trans. Power Electron,* vol. 19, pp. 814-827, May 2004.

[67] D. Jovcic, “Phase-locked loop system for FACTS,” *IEEE Trans. Power Syst.,* vol. 18, pp. 1116-1124, Aug. 2003.

[68] A. Yazdani and R. Iravani, “A unified dynamic model and control for the voltage source inverter under unbalanced grid conditions,” *IEEE Trans. Power Del.,* vol. 21, pp. 1620-1629, July 2006.

[69] M. Savaghebi, A. Jalilian, J. Vasquez, and J. Guerrero, “Secondary control scheme for voltage unbalance compensation in an islanded droop- controlled microgrid,” *IEEE Trans. Smart Grid,* vol. 3, pp. 797-807, June 2012.

[70] K. Vanthournout, K. D. Brabandere, E. Haesen, J. Driesen, G. Deconinck, and R. Belmans, “Agora: Distributed tertiary cotrol of distributed resources,” in *Proc. 15th Power Systems Computation Conf.*, 2005, pp. 1-7.

[71] A. Pantoja and N. Quijano, “A population dynamics approach for the dispatch of distributed generators,” *IEEE Trans. Ind. Electron.,* vol. 58, pp. 4559-4567, Oct. 2011.

[72] T.Tanabe, *et al.*, “Optimized operation and stabilization of microgrids with multiple energy resources,” in *Proc. 7th Int. Conf. on Power Electron.*, 2007, pp. 74 - 78.

[73] E. Barklund, N. Pogaku, M. Prodanovic´, C. Hernandez-Aramburo, and T. C. Green, “Energy management in autonomous microgrid using stability-constrained droop control of inverters,” *IEEE Trans. Power Electron.,* vol. 23, pp. 2346-2352, September 2008.

[74] C. A. Hernandez-Aramburo, T. C. Green, and N. Mugniot, “Fuel consumption minimization of a microgrid,” *IEEE Trans. Ind. Appl.,* vol. 41, pp. 673-681, May/June 2005.

[75] K. Vanthournout, “A semantic overlay network based robust data-infrastructure, applied to the electric power grid,” PhD Dissertation, Facultiet Ingenieurswetenschappen, Lueven, 2006.

[76] A. Bidram and A. Davoudi, “Hierarchical structure of microgrids control system,” *IEEE Trans. Smart Grid,* vol. 3, pp. 1963-1976, Dec. 2012.

[77] H. Xin, Z. Qu, J. Seuss, and A. Maknouninejad, “A self-organizing strategy for power flow control of photovoltaic generators in a distribution network,” *IEEE Trans. Power Syst.*, vol. 26, pp. 1462-1473, Aug. 2011.

[78] S. D. J. McArthur, E. M. Davidson, V. M. Catterson, A. L. Dimeas, N. D. Hatziargyriou, F. Ponci, and T. Funabashi, “Multi-agent systems for power engineering applications-part I: Concepts, approaches, and technical challenges,” *IEEE Trans. Power Syst.,* vol. 22, pp. 1743-1752, Nov. 2007.

[79] Q. Hui and W. Haddad, “Distributed nonlinear control algorithms for network consensus,” *Automatica*, vol. 42, pp. 2375–2381, 2008.

[80] J. Fax and R. Murray, “Information flow and cooperative control of vehicle formations,” *IEEE Trans. Automatic Control*, vol. 49, pp. 1465–1476, Sept. 2004.

[81] W. Ren and R. W. Beard, *Distributed consensus in multi-vehicle cooperative control*. Berlin: Springer, 2008.

[82] Z. Qu, *Cooperative control of dynamical systems: Applications to autonomous vehicles*. New York: Springer-Verlag, 2009.

[83] A. Jadbabaie, J. Lin, and A. S. Morse, “Coordination of groups of mobile autonomous agents using nearest neighbor rules,” *IEEE Trans. Automatic Control*, vol. 48, pp. 988–1001, June 2003.

[84] X. Li, X. Wang, and G. Chen, “Pinning a complex dynamical network to its equilibrium,” *IEEE Trans. Circuits and Systems I: Regular Papers,* vol. 51, 2074–2087, Oct. 2004.

[85] Q. Yang, J. A. Barria, and T. C. Green, “Communication infrastructures for distributed control of power distribution networks,” *IEEE Trans. Industrial Informatics*, vol. 7, pp. 316-327, May. 2011.

[86] A. Bidram, A. Davoudi, F. L. Lewis, and J. M. Guerrero, “Distributed cooperative secondary control of microgrids using feedback linearization,” *IEEE Trans. Power Syst.,* vol. 28, pp. 3462-3470, Aug. 2013.

[87] Q. Zhang, L. Lapierre, and X. Xiang, “Distributed control of coordinated path tracking for networked nonholonomic mobile vehicles,” *IEEE Trans. Industrial Informatics*, vol. 9, pp. 472-484, Feb. 2013.

[88] Z. Li, Z. Duan, G. Chen, and L. Huang, “Consensus of multi-agent systems and synchronization of complex networks: a unified view point,” *IEEE Trans. Circuits and Systems I,* vol. 57, pp. 213–224, Jan. 2010.

[89] A. Das and F. L. Lewis, “Distributed adaptive control for synchronization of unknown nonlinear networked systems,” *Automatica*, vol. 46, pp. 2014-2021, 2010.

[90] A. Bidram, F. Lewis, A. Davoudi, and J. Guerrero, “Distributed cooperative control of nonlinear and non-identical multi-agent systems,” in *Proc.*21st Mediterranean Conf. Control and Automation, 2013, pp. 770-775.

[91] N. Pogaku, M. Prodanovic, and T. C. Green, “Modeling, analysis and testing of autonomous operation of an inverter-based microgrid,” *IEEE Trans. Power Electron.*, vol. 22, pp. 613–625, March 2007.

[92] M. N. Marwali and A. Keyhani, “Control of distributed generation systems part I: Voltage and currents control,” *IEEE Trans. Power Electron.*, vol. 19, pp. 1541–1550, Nov. 2004.

[93] A. Keyhani, M. N. Marwali, and M. Dai, *Integration of green and renewable energy in electric power systems*. New Jersey: Wiley, 2010.

[94] J. J. E. Slotine and W. Li, *Applied nonlinear control*. New Jersey: Prentice-Hall, 2009.

[95] J. W. Brewer, “Kronecker products and matrix calculus in system theory,” *IEEE Trans. Circuits and Systems*, vol. 25*,* pp. 772-781, Sept. 1978.

[96] F. L. Lewis and V. L. Syrmos, *Optimal control*. New York: Wiley, 1995.

[97] H. Zhang, F. L. Lewis, and A. Das, “Optimal design for synchronization of cooperative systems: State feedback, observer, and output feedback,” *IEEE Trans. Automatic Control*, vol. 56, pp. 1948–1952, Aug. 2011.

[98] E. Bassi, F. Benzi, L. Lusetti, and G. S. Buja, “Communication protocols for electrical drives,” in *Proc. 21st Int. Conf. Industrial Electronics (IECON)*, 1995, pp. 706–711.

[99] R. K. Ahuja, T. L. Magnanti, andJ. B. Orlin, *Network flows: theory, algorithms, and applications*. Englewood Cliffs: Prentice Hall: 1993.

[100] R. Burkard, M. Dell’Amico, and S. Martello, *Assignment Problems*. Philadelphia: SIAM: 2009.

[101] A. Bidram, A. Davoudi, F. L. Lewis, and Z. Qu, “Secondary control of microgrids based on distributed cooperative control of multi-agent systems,” *IET Generation, Transmission and Distribution*, vol. 7, pp. 822-831, Aug. 2013.

[102] I. Serban and C. Marinescu, “Frequency control issues in microgrids with renewable energy resources,” *Proc. 7th Int. Symposium on Advanced Topics in Electrical Eng.*, 2011, pp. 1–6.

[103] M. B. Delghavi and A. Yazdani, “A unified control strategy for electronically interfaced distributed energy resources,” *IEEE Trans. Power Delivery,* vol. 27, pp. 803-812, Apr. 2012.

[104] H. Zhang and F. L. Lewis, “Adaptive cooperative tracking control of higher-order nonlinear systems with unknown dynamics,” *Automatica*, vol. 48, pp. 1432–1439, 2012.

[105] E. Serban and H. Serban, “A control strategy for a distributed power generation microgrid application with voltage- and current-controlled source converter,” *IEEE Trans. Power Electron.*, vol. 15, pp. 2981–2992, Dec. 2010.

[106] S. Teleke, M. E. Baran, S. Bhattacharya, and A. Q. Huang, “Rule-based control of battery energy storage for dispatching intermittent renewable sources,” *IEEE Trans. Sustainable Energy*, vol. 1, pp. 117–124, Oct. 2010.

[107] A. Bidram, M. E. H Golshan, and A. Davoudi, “Capacitor design considering first swing stability of distributed generations,” *IEEE Trans. Power Syst.,* vol. 27, pp. 1941-1948, Nov. 2012.

[108] A. Bidram, M. E. H. Golshan, and A. Davoudi, “Loading constraints for first swing stability margin enhancement of distribution generation,” *IET Generation, Transmission, and Distribution*, vol. 6, pp. 1292-1300,Dec. 2012.

[109] A. Bidram, A. Davoudi, and F. Lewis, “Two-layer distributed cooperative control of multi-inverter microgrids,” *Digest accepted in IEEE Applied Power Electronics Conf. and Exposition*, Sept 2013, (Paper ID: 1493).

[110] A. Maknouninejad, Z. Qu, J. Enslin, and N. Kutkut, “Clustering and cooperative control of distributed generators for maintaining microgrid unified voltage profile and complex power control,” in *Proc*. *IEEE PES Transmission and Distribution Conference and Exposition* , Orlando, FL, 2012, pp. 1-8.

[111] S. K. Chung, “A phase tracking system for three phase utility interface inverters,” *IEEE Trans. Power Electron.*, vol. 15, pp. 431–438, May 2000.

[112] N. Mwakabuta and A. Sekar, “Comparative study of the IEEE 34 node test feeder under practical simplications," in *Proc. 39th North American Power Symposium*, Sep. 2007.

[113] R. M. Milasi, A. F. Lynch, and Y. W. Li, “Adaptive control of a voltage source converter for power factor correction,” *IEEE Trans. Power Electron.*, vol. 28, pp. 4767–4779, Oct. 2013.

[114] H. Li, F. Li, Y. Xu, D. Tom Rizy, and S. Adhikari, “Autonomous and adaptive voltage control using multiple distributed energy resources,” *IEEE Trans. Power Syst.,* vol. 28, pp. 718–730, Spet. 2012.

[115] H. Li, F. Li, Y. Xu, D. Tom Rizy, and J. D. Kueck, “Adaptive voltage control with distributed energy resources: algorithm, theoretical analysis, simulation, and field test verification,” *IEEE Trans. Power Syst.,* vol. 25, pp. 1638-1647, Aug. 2010.

[116] H. Li, F. Li, Y. Xu, D. T. Rizy, and S. Adhikari, “Autonomous and adaptive voltage control using multiple distributed energy resources,” *IEEE Trans. Power Syst.*, vol. 28, pp. 718–730, May 2013.

[117] A. Das and F. L. Lewis, “Distributed adaptive control for synchronization of unknown nonlinear networked systems,” *Automatica*, vol. 46, pp. 2014-2021, 2010.

[118] Z. Hou, L. Cheng, and M. Tan, “Decentralized robust adaptive control for the multiagent system consensus problem using neural networks,” *IEEE Trans. Systems Man and Cybernetics, Part B-Cybernetics*, vol. 39, pp. 636–647, June 2009.

[119] H. B. Ma, “Decentralized adaptive synchronization of a stochastic discrete-time multiagent dynamic model,” *SIAM J. Control Optim.*, vol. 48, no. 2, pp. 859-880, 2009.

[120] H. Zhang and F. L. Lewis, “Adaptive cooperative tracking control of higher-order nonlinear systems with unknown dynamics,” *Automatica*, vol. 48, pp. 1432-1439, July 2012.

[121] R. Cui, B. Ren, S. S. Ge, “Synchronised tracking control of multi-agent system with high-order dynamics,” *IET Control Theory Appl.*, vol. 6, pp. 603-614, March 2012.

[122] F. L. Lewis, S. Jagannathan, and A. Yesildirek, *Neural network control of robot manipulators and nonlinear systems*. London: Taylor and Francis, 1999.

[123] M. H. Stone, “The generalized Weierstrass approximation theorem,” *Mathematics Magazine*, vol. 21, no. 4/5, pp. 167-184/237-254, 1948.

Biographical Information

Ali Bidram received the B.Sc. and M.Sc. degrees in electrical engineering from Department of Electrical and Computer Engineering, Isfahan University of Technology, Isfahan, Iran, in 2008 and 2010, respectively, and Ph.D. degree in electrical engineering from the Department of Electrical Engineering, the University of Texas at Arlington, Arlington, TX. He received N. M. Stelmakh outstanding student research award in 2014. His research interests include power system dynamics, distributed control systems, micro-grid, and renewable energy resources.